ROBUST APPROACHES TO NON-LINEAR DIFFUSION BASED COMPRESSED SENSING IN PARALLEL MRI

A THESIS SUBMITTED BY

AJIN JOY

In partial fulfilment of the requirements

for the award of the degree of

DOCTOR OF PHILOSOPHY

INDIAN INSTITUTE OF INFORMATION TECHNOLOGY AND MANAGEMENT-KERALA
Trivandrum – 695 581

FACULTY OF TECHNOLOGY
COCHIN UNIVERSITY OF SCIENCE AND TECHNOLOGY
Cochin – 682 022

September 2019

Certificate

This is to certify that the thesis entitled "**Robust Approaches to Non-Linear Diffusion Based Compressed Sensing in Parallel MRI**" submitted by Mr. Ajin Joy to the Cochin University of Science and Technology, Kochi for the award of the degree of Doctor of Philosophy is a bonafide record of research work carried out by him under my supervision and guidance at the Medical Image Computing and Signal Processing Laboratory, Indian Institute of Information Technology and Management-Kerala. The contents of this thesis, in full or in parts, have not been submitted to any other University or Institute for the award of any degree or diploma.

I further certify that the corrections and modifications suggested by the audience during the pre-synopsis seminar and recommended by the Doctoral Committee of Mr. Ajin Joy are incorporated in the thesis.

Prof. (Dr.) Joseph Suresh Paul,

Research Supervisor,

Indian Institute of Information Technology and Management-Kerala,

Trivandrum, 695581.

Place : Trivandrum

Date : 19/09/2019

DECLARATION

I hereby declare that the work presented in the thesis titled "**Robust Approaches to Non-Linear Diffusion Based Compressed Sensing in Parallel MRI**" is based on the original research work carried out by me under the supervision and guidance of Dr. Joseph Suresh Paul, Professor, Indian Institute of Information Technology and Management-Kerala, for the award of the degree of Doctor of Philosophy with Cochin University of Science and Technology. I further declare that the contents of this thesis in full or in parts have not been submitted for the award of any degree, diploma, associateship, or any other title or recognition from any other University/Institution.

Place : Trivandrum Ajin Joy

Date : 19/09/2019

Abstract

Magnetic resonance imaging (MRI) is one of the most popular non-invasive imaging techniques used to look inside the human body and visually represent the physiology of various organs and tissues. One of its particularly notable features is the lack of ionizing radiations involved. However, a relatively high scanning time puts it at a disadvantage. Therefore, a major component of the research in this field over the last four decades has been focused on improving the imaging speed while also trying to achieve better image quality. The demand for accelerated imaging is often met by restricting the amount of data collected from the scanner. Missing data would then be estimated offline to reconstruct an artifact-free image. In this thesis, a new approach to MRI reconstruction using robust non-linear (NL) diffusion based compressed sensing (CS) is introduced and investigated in detail.

The signal processing technique of CS is widely popular due to its ability to facilitate efficient acquisition and reconstruction of a sparse or compressible signal like that of MRI, from relatively few measurements. Among the numerous sparse approximation techniques available in CS, minimization of total variation (TV) has been the key approach to sharply preserve the edges during the reconstruction process.

In the primary phase of this work, a Perona-Malik (PM) diffusion based sparse approximation algorithm is developed as an alternative to TV to address its high

sensitivity to regularization parameter. In the succeeding part, a mixed-order diffusion algorithm is developed that can prevent the formation of both staircase and speckle effects during reconstruction.

It is further observed that the direction of image gradient computation has significant influence on the diffusion of both edges and artifacts. In the final part of the work, this critical aspect is addressed by developing a directionality guided diffusion reconstruction algorithm. This enables a better preservation of the complex structural details in the image by adapting the direction of diffusion to local variations in the directionality of edges and employing a precise diffusion in the local regions of the image on a sub-pixel level.

Acknowledgments

It gives me utmost pleasure to express my heartfelt gratitude and appreciation to the helping hands of all the kind people and almighty that made this thesis possible.

Firstly, I would like to express my sincere gratitude to my advisor Prof. Joseph Suresh Paul for his patience, persistent inspiration and enduring support throughout the course of this work. The sharing of his vast knowledge and experience truly made this journey intellectual and joyful. I'm thankful for his guidance and the freedom he has given me to pursue my research directions. His advices and encouragements at key moments has been invaluable. I thank him with love, respect and admiration.

Besides my advisor, I would like to thank the rest of my doctoral committee members: Dr. S. Savitri at NIIST, Prof. Saji Gopinath, director of IIITM-K, and Prof. Rajasree M.S., former director of IIITM-K, for their constructive feedbacks and encouragement at each stage of the dissertation process.

My gratitude also extends to Prof. Mathews Jacob at UIowa, Prof. Albert Thomas at UCLA and Dr. Ramesh Venkatesan at GE for their insightful comments, Dr. Binu Joy and Dr. Ajith Toms at Rajagiri hospital for their feedbacks from a clinical perspective, and the library department at IIITMK for all the support.

I would like to thank the support and kindness of all the professors, non-teaching staffs and my colleagues at IIITM-K. Thanks to all my fellow labmates for making

this journey memorable, especially Sreekanth and Raji, who has been there with me from day one. I also express my best wishes to the new entrant Vazim.

I'm grateful to all the teachers I ever had for nourishing my science curiosities, especially Profs. V.S. Jayanthi and D. Baskar during my post-graduation days for their encouragements to take up serious research.

I also thankfully acknowledge the Kerala State Council for Science, Technology and Environment and the Council of Scientific and Industrial Research, Govt. of India, for providing the financial support at various stages of this research.

None of this would have been possible without the love and support I got from my mother Shaly T.I. who is also my first teacher, my father Joy Markose who is my pillar of strength, my loving brother Isac Joy, my grandmothers Sosamma and Annamma, my grandaunt Aleyamma, and all my extended family members. I cannot thank them enough.

I would also like to thank my beloved wife Anju Ann Paul, for the happiness she shares and her support and care during this journey. My heartfelt gratitude extends to all my in-laws for their overwhelming love and support.

This journey would not have been the same without my spare time spent with two of my best friends, Amal and Gregary, and many timely advices from my uncle, Dr. T.P. Varghese. I'm very thankful for that.

Memories of my grandfathers, Ackamparambil Markose and Thalamattathil Issac is something which I cherish all the time. I dedicate this thesis to the two of them.

Ajin Joy

Contents

List of Tables

List of Figures

List of Publications

Peer Reviewed Journal Articles:

1. Ajin Joy, Mathews Jacob and Joseph Suresh Paul. “Directionality Guided Non-Linear Diffusion Compressed Sensing MR Image Reconstruction” *Magnetic Resonance in Medicine,* vol. 82, No. 6, pp 2326-2342, 2019.
2. Ajin Joy and Joseph Suresh Paul. “A Mixed-order Non-Linear Diffusion Compressed Sensing MR Image Reconstruction.” *Magnetic Resonance in Medicine,* vol. 80, No. 5, pp 2215-2222, 2018.
3. Ajin Joy and Joseph Suresh Paul. “Multichannel compressed sensing MR image reconstruction using statistically optimized nonlinear diffusion.” *Magnetic Resonance in Medicine,* vol. 78, No. 2, pp 754-762, 2017.
4. Akshara P. Krishnan, Ajin Joy, Joseph Suresh Paul, “Improved image reconstruction of low-resolution multichannel phase contrast angiography,” *Journal of Medical Imaging*, vol. 3, No. 1, pp 014001, 2016.

Conference Proceedings:

1. Ajin Joy and Joseph Suresh Paul. “A Rapid Non-Linear Diffusion Compressed Sensing parallel MR Image Reconstruction.” *In Proceedings of the 11th Indian Conference on Computer Vision, Graphics and Image Processing (ICVGIP)*, December, 2018.

2. Ajin Joy and Joseph Suresh Paul. “Improving Image Quality and Convergence Rate of Perona-Malik Diffusion based Compressed Sensing MR Image Reconstruction by Gradient Correction.” *In Proceedings of the 3rd International Conference on Computer Vision & Image Processing (CVIP)*, September, 2018.
3. Andres Saucedo, Ajin Joy, Eric S. Daar, Mario Guerrero, Joseph Suresh Paul, Manoj K. Sarma and M. Albert Thomas. “Comparison of Compressed Sensing Reconstruction for 3D Echo Planar Spectroscopic Imaging data using Total Variation and Statistically Optimized Perona-Malik Non-linear Diffusion,” *In Proceedings of the 26th Annual Meeting of International Society for Magnetic Resonance in Medicine (ISMRM)*, June, 2018.

Chapter 1

Introduction to Compressed Sensing MRI and Thesis Outline

1.1 Introduction

Compressed Sensing (CS) is a signal processing technique that has recently received a lot of attention in the areas of signal detection, estimation and classification due to its ability to facilitate efficient acquisition and reconstruction of a sparse/compressible signal from relatively few measurements. The term sparsity indicates the scarcity of non-zero elements in a signal. A sparser signal will have a greater number of its elements as zeros as compared to a less sparse one. The theory of CS is built on an idea that the perfect reconstruction of a signal need not require a sampling rate proportional to its maximum frequency as necessitated by the famous Nyquist sampling rate, but proportional to its actual information content, since the complete information in a sparse signal can be captured by collecting only a few of its samples (1-3). This is particularly useful in different areas of imaging sciences like radar imaging, seismic imaging and various bio-medical applications like Magnetic

Resonance Imaging (MRI) (4-6), where the signal of interest has an associated sparse representation.

In the case of MRI for example, which is the broad theme of this thesis, the images are generally compressible in different representations like wavelet and finite differences (6, 7). MRI is one of the established and most popular non-invasive imaging techniques used to look inside the human body and visually represent the physiology of various organs and tissues. It carries clinically valuable information regarding various anatomical and functional details of the internal organs in a human body. One of its particularly notable features is the lack of ionizing radiations involved in the imaging process as compared to other imaging modalities like computed tomography (CT).

Even though the diagnostic information generated by MRI aids in early detection and staging of various diseases and monitoring the body's response to various treatments, the relatively high scanning time involved puts it at a disadvantage. For example, the factors like patient discomfort (MRI scanners generate noise due to gradient fields) and motion related artifacts in the image (because patient might find it difficult to stay still for a longer duration) become important when the scanning time is high. Furthermore, one would ideally prefer the magnetic resonance (MR) images to have both high resolution and large spatial field-of-view (FOV) at the same time. While a high resolution gives more information about the fine details in the image, a large spatial FOV covers more area in the scan. However, to achieve this simultaneously, dense sampling (small sampling interval) and larger FOV of k-space

are required. That is, a greater number of samples need to be collected, increasing the scan time.

Therefore, the research in this field over the last four decades has been mainly focused on improving the imaging speed while also trying to achieve better image quality. In MRI, the data is collected in 'k-space', which is a collection of the spatial frequencies of the image, related to the actual image through Fourier transform. That is, the entries of k-space are Fourier coefficients of the image. As the sampling speed is fundamentally limited by various physical and physiological constraints, a straightforward approach to address the aforementioned factors is to accelerate the imaging process (data acquisition) by limiting the number of samples collected to what is essential. The skipped samples are then estimated from the collected samples using the computing power of modern-day computers. This is the well-defined and widely researched reconstruction problem in MRI where the MR signal collected in k-space is undersampled and an artifact-free image is reconstructed from it.

The fact that CS can correctly reconstruct a sparse signal from randomly measured Fourier coefficients with high probability (as proved by Emmanuel Candès, David Donoho, Justin Romberg and Terence Tao in 2004) made it a natural candidate for solving the rapid MR imaging problem (1). Due to the highly compressible nature of MR images, application of CS theory becomes feasible and facilitates an accelerated data acquisition without compromising the image quality. This forms the specific theme of this thesis, with the major contributions being the CS based novel approaches to MR image reconstruction.

In the following, a background of the MR image formation and the associated reconstruction problem using CS is briefly described along with the details of the original contribution in this thesis.

1.2 Basics of MR Image Formation

1.2.1 Nuclear magnetization and MR signal generation

In principle, an MR image is a visual interpretation of the response of different tissues inside the human body to a magnetic field applied around it. More specifically, it is the response of hydrogen nuclei (a single proton) inside different tissues that is generally measured. Since proton possesses an electric charge and is spinning on its axis, its behavior can be compared to that of a tiny bar magnet. Spinning charge constitutes a current loop and therefore has a magnetic moment associated with it. The overall spin of an atomic nucleus is by virtue of the spin of nucleons (protons or neutrons) within it. Each nucleon possesses a spin of ±1/2. Pairing of nucleons can cancel the spin due to their anti-parallel alignment. Therefore, not all nuclei exhibit magnetism. It is the unpaired nucleons that generate a non-zero spin. The nucleus of Hydrogen, for example, constituting only a single proton, gives rise to an overall spin of 1/2 for the atom. Therefore, it is a suitable candidate for nuclear magnetization and is generally used in MRI. It has a high biological abundance to further justify its candidacy. The signal generation involves three main stages.

1. Alignment: Spins are forced to align with an applied magnetic field B_0 to generate a net macroscopic magnetization, M.

Under normal circumstances, the spin of these tiny magnets in the body are randomly aligned. Therefore, it does not exhibit magnetization in macroscopic scale. However, in the presence of a strong magnetic field, such as the one applied by an MRI scanner, these spins are forced to line up with the direction of the applied magnetic field (B_0). This creates a magnetic vector oriented along the axis (Z-axis) of the applied field and the spin vector of protons aligns itself in either parallel or anti-parallel direction compared to that of the applied filed. It corresponds to two distinct energy levels/states. For spin-1/2 nuclei, the energy levels are separated by $\Delta E = \gamma \hbar B_0$ where γ is the gyromagnetic ratio of the nuclei and $\hbar$ is the Planck constant. For protons, $\gamma = 2\pi \times 42.57$ MHz/T.

Compared to the thermal energy at room temperature, the difference in energy between two distinct energy states is relatively small. This can cause the protons to acquire enough energy from the thermal noise to induce a transition between two states. However, it is observed that at thermal equilibrium, the parallel state of the spin which is at lower potential energy is slightly more populous than the antiparallel state. This difference in population generates a net macroscopic magnetization (M) in the direction of the B_0 field.

2. Excitation: M is tilted away from B_0 by applying an RF pulse.

The net magnetization M is a vector that can be resolved into longitudinal (M_Z) and transverse (M_X and M_Y) components with respect to the main magnetic field B_0. When the object is first placed in the B_0 field, the net magnetization builds exponentially as a function of time and reaches a maximum value M_0 at equilibrium. The resulting magnetic vector has no component of magnetization (M_X or M_Y) along

transverse plane (XY-plane orthogonal to Z-axis) and the component along Z-axis, M_Z is equal to M_o.

In this situation, if the difference in energy between the two states is supplied in the form of a radiofrequency (RF) pulse orthogonal to the Z-axis, it can excite the protons from lower energy state to higher energy state. For an individual spin to change its energy state, the excitation has to be at its resonance frequency ω_0, expressed as $\omega_0 = \gamma B_0$. Consequently, it alters the population balance between the energy states and the orientation of net magnetic vector moves away from the Z-axis. As it moves towards the XY-plane, M_X and M_Y components of magnetization are generated. This RF pulse is also called a 90^0 pulse since it flips the net magnetic vector from Z-direction to the orthogonal XY-plane.

The RF pulse is applied in the form of a rotating magnetic field (B_1 field) along XY-plane. Therefore, the effective magnetic field consists of a stationary field along Z-axis and a rotating field along XY-plane. This forces the net magnetization vector to precess about the Z-axis. The frequency at which bulk magnetization precesses is called Larmor frequency, which is identical to the resonance frequency ω_0.

3. Relaxation: M returns to the resting state, aligning with the B_0 field and generating the MR signal.

If the RF pulse is now turned off, the magnetic vector will slowly return to its resting state (aligned to the main magnetic field B_0). Consequently, the strength of longitudinal component M_Z increases and the transverse components M_X and M_Y decrease (at a different rate for different type of tissues). The resulting signal is known

as the free induction decay (FID). This is the MR signal generated from the object being scanned. If a set of receiver coils are placed nearby the object, the rotating magnetic field will induce an alternating current in them. This way, the MR signal is captured. The frequency of precession will be different for different atomic nuclei depending on its gyromagnetic ratio. Therefore, the nuclei other than that of Hydrogen will produce an MR signal only if the energy delivered by the excitation RF pulse is at its respective Larmor frequency.

1.2.2 Spatial encoding, k-space and image formation

The MR signal generated through the stages of alignment, excitation and relaxation represents the entire volume of the object. In order to localize the signal from just the region-of-interest (ROI), say a small area in one slice of the object, the spatial information is encoded. This involves three stages.

1. Slice selection: By applying a magnetic field gradient (G_Z) in the Z-direction on top of the B_0 field, the effective field becomes $B(r) = B_0 + G_Z r$, where r is the spatial location. This causes a linear variation of precession frequency in space. Therefore, when an RF excitation pulse is applied, the Larmor frequency will be matched for only a sub-volume (slice) of the object. This way, the slice of interest is selected using an appropriate RF pulse frequency.
2. Phase encoding (PE): With a slice selected, the entire plane of the slice is resonating at the Larmor frequency. Each slice can be further divided into rows and columns. In order to localize the signal from different rows, another magnetic field gradient (G_Y) is applied along Y-axis for a certain time interval

τ. This varies the frequency in this direction and the signals at different positions accumulate different phase. The extent of phase shift is proportional to the amplitude and time duration of G_Y. When the gradient is switched off after the interval, the precessing frequency of the selected slice will return to the same resonating frequency but not its phase. Therefore, the signal from each row can be distinguished by its phase shift.

3. Frequency encoding (FE): In order for the signal to be fully spatially localized, different locations in a row should be distinguishable as well. This is realized by applying another magnetic field gradient (G_X) along X-direction. G_X is turned on at the same time when a readout (signal detection by receiver coil) is performed. Consequently, the signal recorded at successive time points (different locations in a row) will be at different frequencies. In order to collect the signal from a different row, another phase shift is introduced by G_Y and readout is again performed with G_X turned on.

In summary, the MRI signal is localised in the three-dimensional (3D) space by manipulating the magnetic properties of the nuclei in a predictable way. Signal detected by a receiver coil is the integration of all spins over the entire volume. The variation in precession frequency due to G_x and G_y gradients causes a location dependent phase dispersion to develop in the selected XY-plane (slice). Since readout is performed at the same time when G_X is applied, the contribution of G_X in phase dispersion varies according to time t while the contribution of G_Y remains constant for the entire duration of a single readout. Let u and v be the respective spatial frequencies along the directions X and Y at time t.

$$u = \frac{\gamma G_x t}{2\pi}, \quad [1.1]$$

$$v = \frac{\gamma G_y \tau}{2\pi}. \quad [1.2]$$

Then the detected MRI signal is given by

$$s(t) = \iint \rho(x,y) e^{-i2\pi(ux+vy)} dxdy \quad [1.3]$$

where ρ denotes the spin density at location (x, y) and the integral of $2\pi(ux + vy)$ is the phase accumulated due to G_X and G_Y from the time when RF excitation pulse is switched off till t. This signal equation represents the Fourier transform of the selected slice image. The discrete time samples of this signal are then stored in the k-space, which is a rectangular array. Therefore, the spin density in image space can be reconstructed by an inverse Fast Fourier Transform (FFT) of the k-space. This way, the MR signal from a 3D volume is collected in the form of multiple slices. Instead of a two-dimensional (2D) slice, localized signal from 3D volume can be acquired as well using another PE gradient along the Z-direction.

One of the challenges while collecting FID is that the spins contributing to transverse magnetization start to go out of phase post the application of 90^0 RF pulse. That is, some of the spins precess faster than others causing a phase difference. This weakens the total signal over time leaving only a short duration to measure the useful signal. Therefore, the signal is generally forced to rephrase by different techniques like spin echo and gradient echo (8-10), so that it can be measured when the spins are back in phase again. For example, the technique of spin echo applies an additional RF pulse called 180^0 pulse, after the initial 90^0 pulse. This flips the entire spins in XY-plane by

an angle of 180^0, causing the faster precessing spins to appear lagging behind the slower ones. However, since these spins continue to precess faster, it catches up with the slower spins causing the signal to rephase. The measured signal is called an echo. It is sampled using an analog to digital converter and stored in k-space. A typical spin echo pulse sequence in shown in Fig. 1.1. In order to collect another echo, the process is repeated after the repetition time (TR). Usually, the sequence of RF pulses is designed such that the echo occurs in the middle of the data collection period. By varying the sequence of pulses applied and collected, different types of images are created. The user can choose different parameters of the sequence to find the best compromise between tissue contrast, spatial resolution and speed of acquisition.

1.3 MR Image Reconstruction

1.3.1 Undersampling of k-space

Different trajectories to traverse the k-space can be achieved by changing the encoding gradients in an appropriate way. A Cartesian trajectory where the samples are collected on a rectangular grid is the most frequently used sampling pattern. This is mainly because it enables the reconstruction by a simple inverse FFT which is easy to implement. However, there are non-Cartesian sampling patterns in use as well, like sampling along radial and spiral trajectories where the data points generated do not fall into a rectangular matrix. Examples of some of the popular undersampling patterns are shown in Fig. 1.2. White and black pixels represent sampled and skipped locations of k-space respectively. The energy distribution in k-space is mostly concentrated in the

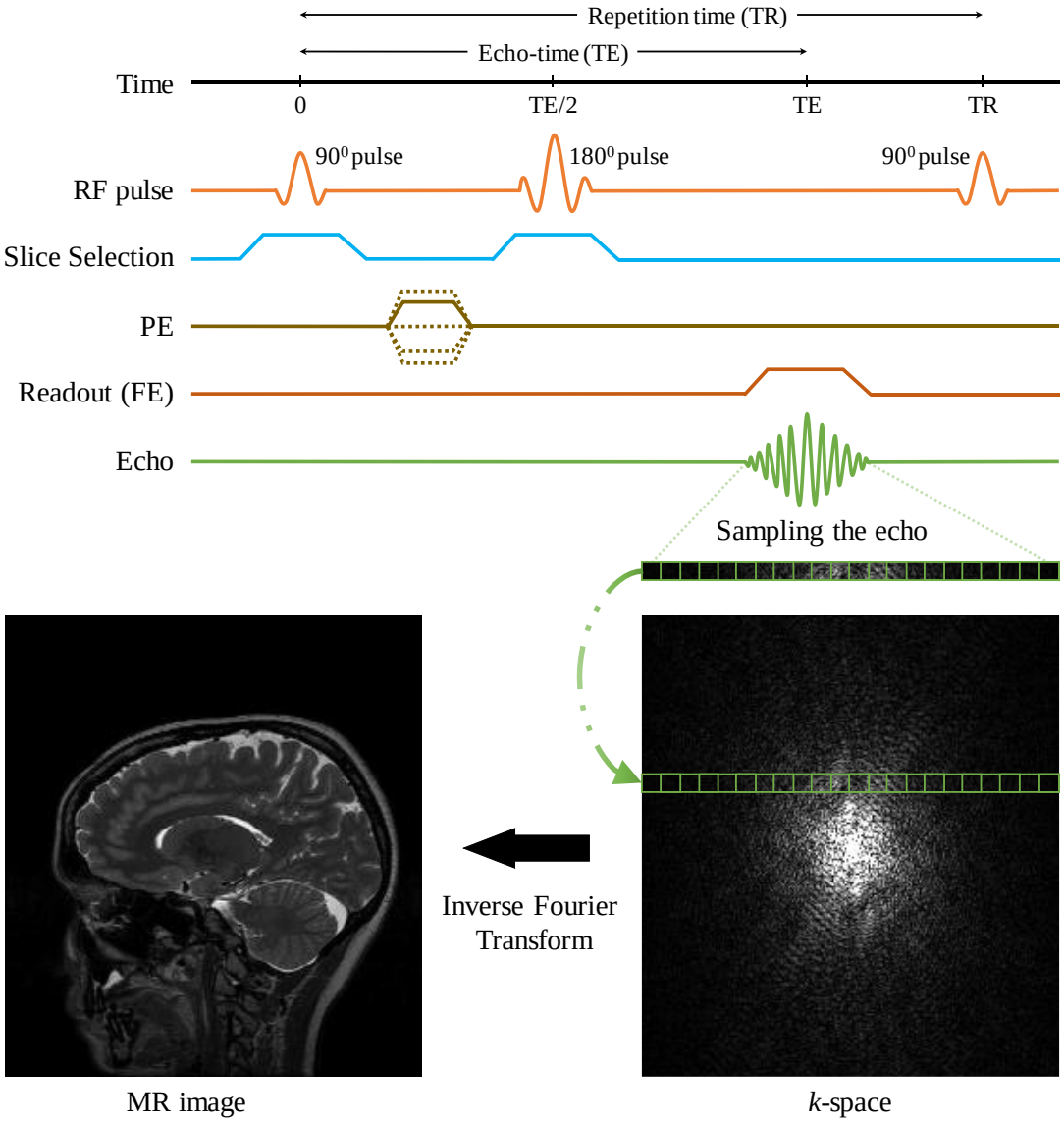

Figure 1.1. An example of spin echo pulse sequence diagram and MR image formation. The echo is sampled using analog-to-digital converter and forms a line in the k-space. Time to collect an echo is marked as echo-time (TE). In order to fill another line, the RF pulses and gradient fileds are applied again after the repetition time, TR. Dotted lines in PE represent different PE gradient strengths and polarities used to collect additional lines in k-space. After filling all lines in k-space, it is inverse Fourier transformed to generate the MR image.

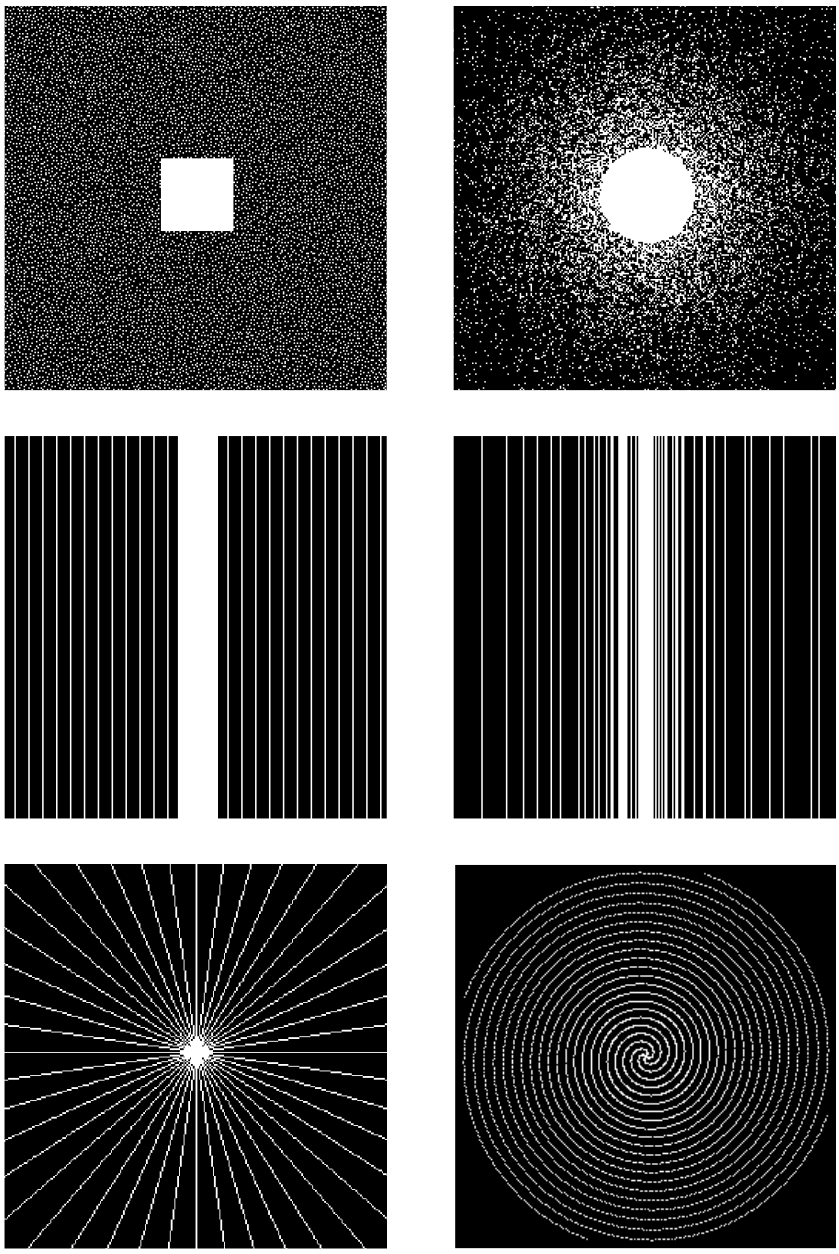

Figure 1.2. Different sampling trajectories. Panels from left to right in the top row shows Poisson-disc and Gaussian density sampling, middle row shows uniform PE and random PE lines sampling and bottom row shows radial and spiral sampling.

low frequency region, which is close to its center. Therefore, undersampling is generally limited to the peripheral region.

Missing samples in the k-space introduces artifacts in the image. The way these artifacts manifest depends on the type of sampling pattern used. For example, uniform undersampling of k-space, such as skipping every other line of k-space, results in artifacts that are very similar to the actual structural details of the image. On the other hand, random undersampling causes the artifacts to appear more like noise. This is shown in Fig. 1.3 which illustrates the result of inverse Fourier transform of k-space with the values at unacquired locations set to zero (zero-filled reconstruction).

1.3.2 CS approach to sampling and reconstruction

For storage and computational purposes, the natural signals which are continuous in nature are often converted to discrete domain. This process samples the signal, generally based on Shannon-Nyquist sampling theorem which ensures perfect reconstruction of the signal if sampled at twice its maximum frequency. However, in many applications, the signal of interest is found to have a sparse representation. That is, the actual information content of the signal can be approximated using a few coefficients when represented in certain basis, referred to as sparsity basis. For example, MR images are known to be sparse in different basis like wavelets and ridgelets. Fig. 1.4 shows the sparsity of an MR image in wavelet and finite difference representations. Digital images are often compressed with hardly any perceivable loss in visual quality by storing only a few significant wavelet coefficients. The number of samples thus required to capture the complete information is far less compared to what

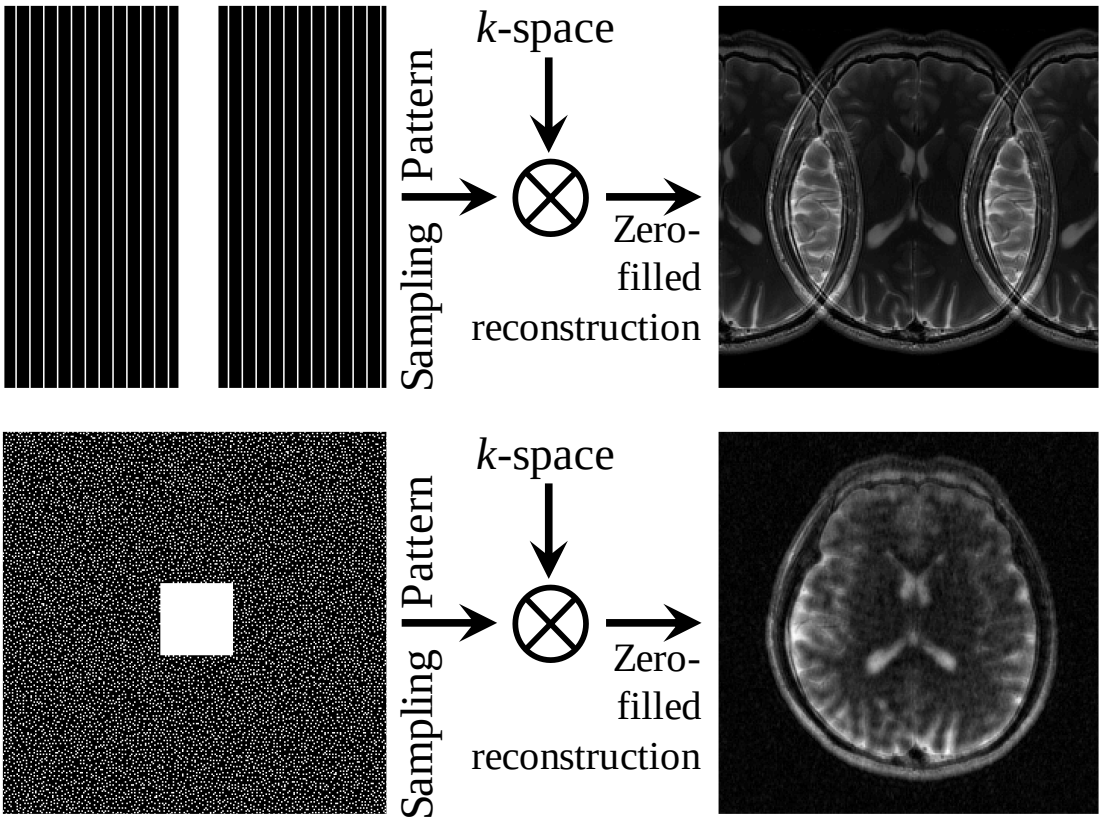

Figure 1.3. Zero-filled reconstruction. Panels in the top row shows the zero-filled reconstruction of k-space undersampled by uniformly skipping PE lines. Panels in the bottom row shows the result when k-space is randomly undersampled.

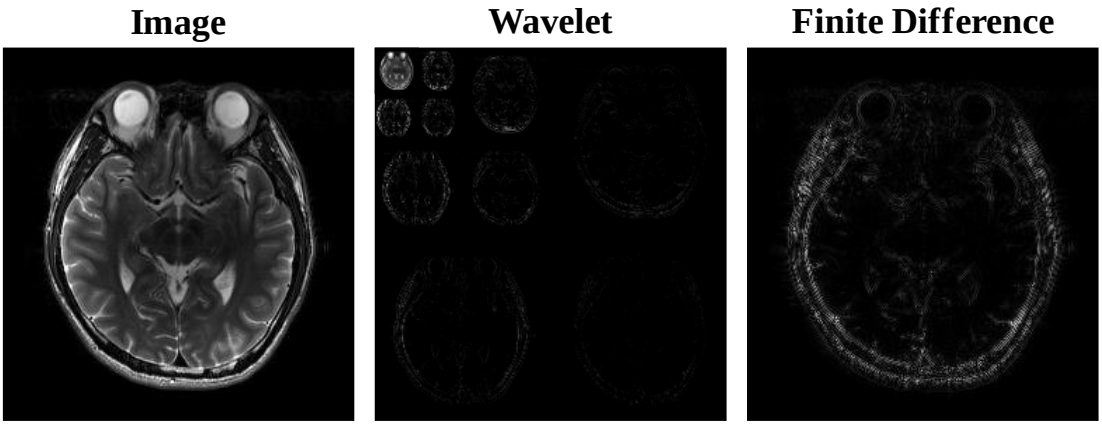

Figure 1.4. Transform domain sparsity of MR image. Panels from left to right shows image domain, wavelet domain and finite difference representation of an MR image.

is required if the image is sampled at Nyquist rate. The technique of CS is rooted on this fact and describes how to faithfully reconstruct a signal from samples collected at sub-Nyquist rate, if one has the knowledge about that signal's sparsity.

For example, consider the sampling of a discrete complex signal $\mathbb{x}$ of length $\mathcal{N}$. Images can be considered in this form by concatenating its columns to form one vector. Let $\mathbb{y}$ be the measurement vector of length $\mathcal{M}$ such that

$$\mathbb{y} = A\mathbb{x} \qquad [1.4]$$

where A is the measurement matrix of size $\mathcal{M} \times \mathcal{N}$. Since a typical acquisition based on CS would sample the signal at a rate much lower than the Nyquist limit, $\mathcal{M} \ll \mathcal{N}$. This makes the system under-determined and we cannot retrieve $\mathbb{x}$ uniquely from $\mathbb{y}$. In order to uniquely solve this system of linear equations, we need $\mathcal{M} \geq \mathcal{N}$.

Now, consider the case where $\mathbb{x}$ is $\mathcal{S}$-sparse. That is, $\mathbb{x}$ has only $\mathcal{S}$ non-zero values and the remaining entries are zeros, $\mathcal{S} \ll \mathcal{N}$. Suppose we also know the locations of $\mathcal{S}$ non-zero entries in $\mathbb{x}$. Then, we have

$$\mathbb{y} = A_{\mathcal{S}}\mathbb{x}_{\mathcal{S}} \qquad [1.5]$$

where $A_{\mathcal{S}}$ is formed by keeping only $\mathcal{S}$ columns of A corresponding to the non-zero locations in $\mathbb{x}$ and $\mathbb{x}_{\mathcal{S}}$ is formed by keeping the $\mathcal{S}$ non-zero entries of $\mathbb{x}$. Now, if $\mathcal{M} > \mathcal{S}$, the problem is over-determined and a unique solution can be found. If $A^H A = I$, least squares method can be used to obtain a signal estimate as

$$\hat{\mathbb{x}}_{\mathcal{S}} = (A_{\mathcal{S}}^H A_{\mathcal{S}})^{-1} A_{\mathcal{S}}^H \mathbb{y} \qquad [1.6]$$

In practical scenarios, the locations of non-zero values are unknown and hence the solution can't be found this way. However, CS shows that the sparsest solution will be unique (11, 12). That is, as long as it is known that the solution will be sparse, CS shows that $\mathbb{x}_{\mathcal{S}}$ can be recovered from the $\mathcal{M}$ linear measurements, with $\mathcal{S} < \mathcal{M} < \mathcal{N}$, by finding the sparsest solution to (Eq. [1.5]), provided the sampling matrix follows a certain property known as Restricted Isometry Property (RIP) (13-15). Therefore, in practical scenarios, we need not search for $\mathcal{S}$-sparse solution, but instead only find the sparsest solution.

The RIP condition defines a quality measure for A, called restricted isometry constant $\delta_{\mathcal{S}}$, to ensure that the signal energy is not lost while sampling. For good CS measurement matrices, $\delta_{\mathcal{S}}$ which will be small (close to 0). For all $\mathcal{S}$-sparse signals $\mathbb{x}_{\mathcal{S}}$, $\delta_{\mathcal{S}}$ is defined as the smallest quantity that satisfies

$$(1 - \delta_{\mathcal{S}})\|\mathbb{x}_{\mathcal{S}}\|_2^2 \leq \|A\mathbb{x}_{\mathcal{S}}\|_2^2 \leq (1 + \delta_{\mathcal{S}})\|\mathbb{x}_{\mathcal{S}}\|_2^2. \qquad [1.7]$$

Even though the value of $\delta_{\mathcal{S}}$ is very hard to evaluate, it is found that a matrix randomly drawn from the family of random matrices satisfies RIP with very high probability (14). For example, random measurement matrices like Gaussian random matrix is known to have small restricted isometry constants. For signals which are not sparse by themselves but are sparse when represented using a sparsity basis Ψ, the matrix A that maps the sparse coefficients to the measurements is defined as $A = \Phi\Psi^H$, where Φ is the $\mathcal{M} \times \mathcal{N}$ measurement matrix (which is Fourier in the case of MRI) and Ψ is an $\mathcal{N} \times \mathcal{N}$ sparsifying transform matrix.

Yet another important criterion for applying compressed sensing is the requirement of incoherent sampling. This notion of incoherence may be estimated using transform point spread function (TPSF) when orthogonal sparsifying transform is used (6). It measures the influence of one pixel on another in the sparse domain due to undersampling. That is, say the sparse domain has a value of 1 for the pixel at the i^{th} location and 0 for all other pixels. It can be transformed into the Fourier domain using an operator $\mathcal{F}\Psi^H$, where $\mathcal{F}$ is the Fourier transform operator. After undersampling the Fourier coefficients, say it is transformed back to the sparse domain. Then, TSPF(i,j) measures the result at j^{th} location in the sparse domain. For effective application of CS theory, the TPSF should be as small as possible and have noise-like statistics (6). Random undersampling in general leads to better TPSF values compared to uniform undersampling.

In an MR image reconstruction perspective, the random sampling is generally achieved by randomly skipping the PE steps during acquisition. Since the FE step is very quick on its own, undersampling along its direction doesn't help the cause of accelerated acquisition by much. A typical example of the sampling pattern with randomly skipped PE lines for a 2D acquisition is shown in Fig. 1.2. In the case of a 3D acquisition, randomization along two directions like the Poisson-disc random sampling is possible since it has two PE dimensions.

1.3.3 Sparse optimization formulation

An MR image is considered to have the sparsest representation when the k-space is fully sampled. Undersampling of k-space introduces aliasing artifacts in the image,

which reduces the sparsity. When the sampling pattern is random, application of CS theory becomes feasible and the image can be reconstructed by finding its sparsest representation in a domain where it is known to be sparse. That is, out of all the possible ways which one can fill the missing samples of k-space, the best solution would be that set of k-space values which can maximize the sparsity of the image in its sparse domain.

Expressing mathematically, a signal $\mathbb{x}$'s sparsity is measured as its l_0-norm (defined as $\|\mathbb{x}\|_0 = \lim_{p\to 0} \sum_i |\mathbb{x}_i|^p$), which counts the number of non-zero coefficients in $\mathbb{x}$. For signals which are sparse when represented using a sparsity basis Ψ, $\mathbb{x}$ can be recovered by finding its sparse representation $\mathbb{z}$, $\mathbb{z} = \Psi\mathbb{x}$, especially when Ψ is orthonormal. With the prior knowledge that $\mathbb{x}$ is sparse in Ψ, a typical CS reconstruction method would reconstruct it from $\mathbb{y}$ by solving the following constraint l_0 minimization problem.

$$\min_{\mathbb{z}} \|\mathbb{z}\|_0 \; subject\ to \; \|\mathbb{y} - A\mathbb{z}\|_2^2 < \epsilon \qquad [1.8]$$

where the quadratic constraint is a fidelity term that restricts the deviation of solution from $\mathbb{y}$ and ϵ is related to the noise level in the signal.

This type of formulation in which one seeks for the sparse coefficients of $\mathbb{x}$ is called synthesis model (16, 17). The signal of interest, $\mathbb{x}$ is then recovered from $\mathbb{z}$ by the transformation, $\mathbb{x} = \Psi^{\mathrm{T}}\mathbb{z}$. However, this is not possible with the choices of sparse transform domains where Ψ is not orthogonal. For example, in the finite differencing domain where a signal is represented by its gradient, we have $\mathbb{z} = \Psi\mathbb{x}$, but $\mathbb{x} \neq \Psi^{\mathrm{T}}\mathbb{z}$. Since the gradients computed by a finite difference operation can be sparse, it is

commonly considered as a sparse transform domain. This is particularly important in the case of MRI since piecewise smooth signals like MR images have very sparse gradients. To facilitate reconstruction in such cases, an alternative formulation called analysis model (16, 17) is used where the emphasis is on finding the signal $\mathbb{x}$ whose transformed coefficients are sparse, as follows.

$$\min_{\mathbb{x}} \|\Psi\mathbb{x}\|_0 \ \ subject\ to\ \|\mathbb{y} - \Phi\mathbb{x}\|_2^2 < \epsilon \qquad [1.9]$$

Be it synthesis or analysis model, the formulations typically involve two parts, (i) sparse approximation of $\mathbb{x}$ and (ii) data consistency with $\mathbb{y}$.

(i) sparse approximation of $\mathbb{x}$ **:** Minimizing l_0-norm of the signal in sparse domain is what is required to find the sparsest solution as shown in Eqs. [1.8 - 1.9]. Even though finding an exact solution this way is proven to be an non-deterministic polynomial (NP) hard problem (18), results in (3, 11, 12, 19) shows that the sparse solution can be approximated by replacing l_0-norm with l_1-norm which is its tightest convex surrogate. This has since been the most popular alternative to l_0-norm for sparse approximations, though other non-convex l_p-norms ($0 < p < 1$) have been successfully explored (20, 21) as well. An l_p-norm of a vector $\mathbb{x}$ is expressed as $\|\mathbb{x}\|_p = (\sum_i |\mathbb{x}_i|^p)^{1/p}$. The l_1-norm, therefore, provides absolute sum of the elements in the vector and modifies Eq. [1.9] as

$$\min_{\mathbb{x}} \|\Psi\mathbb{x}\|_1 \ \ subject\ to\ \|\mathbb{y} - \Phi\mathbb{x}\|_2^2 < \epsilon \qquad [1.10]$$

The associated unconstrained Lagrangian form is

$$\operatorname*{argmin}_{\mathbb{x}} \|\mathbb{y} - \Phi\mathbb{x}\|_2^2 + \lambda\|\Psi\mathbb{x}\|_1 \qquad [1.11]$$

where λ is a regularization parameter that controls the trade-off between sparsity and data fidelity.

The unconstrained l_1-minimization problem in Eq. [1.11] has been solved using different methods like nonlinear conjugate gradients (6), projection onto convex sets (22), iterated shrinkage (23-29) and iteratively reweighted least squares (21). Attempts to directly solve the problem of l_0-norm minimization mainly involves a group of greedy algorithms (30-33), mostly without any guarantees for an optimum solution. These algorithms in general try to iteratively detect the support set (columns of A corresponding to non-zero elements in the sparse vector $\mathbb{z}$) so that the signal can be reconstructed from its measurements by a least squares fit.

The sparse approximation using l_1-norm minimization is often also referred to as Basis Pursuit De-Noising (BPDN) (34) or Least Absolute Shrinkage and Selection Operator (LASSO) (35). A closely related formulation with an equality constraint $\mathbb{y} = \Phi\mathbb{x}$, known as Basis Pursuit (36), addresses the sparse approximation problem when the measured signal $\mathbb{y}$ is noiseless.

(ii) data consistency with $\mathbb{y}$: The second part of the reconstruction formulation is to ensure data fidelity. Unlike the different realizations to sparse approximation, l_2-norm is often always the ideal choice to ensure data consistency. This is due to the quadratic nature of l_2-norm, which penalizes large errors significantly more as compared to the smaller ones.

1.4 Motivation and Problem Statement

The realization of CS in MRI has triggered a thorough research over the last decade contributing to its much-needed acceleration in data acquisition process. During this period, a cohort of reconstruction algorithms were developed that differ in their approaches to sparse representation of the image while having a common aim of estimating the missing random samples in k-space. A particularly notable approach that constitutes the specific theme of this thesis is that of the edge preserving reconstruction which considers the image to be sparsely represented by spatial finite differences. Its importance is mainly due to the fact that the edges are one of the key features in an MR image that helps to distinguish different anatomical regions and thus must be preserved sharp and undistorted while removing the artifacts due to undersampling.

Among the different edge preserving compressed sensing MRI (CS-MRI) reconstruction techniques that were developed in this period, the Total Variation (TV) based approaches stands out as the most popular. A TV regularizer minimizes the l_1-norm of image gradients. Ever since it was pioneered by Rudin et al. (37) in 1992 (known as ROF model), TV based approaches have played a major role in the field of image denoising/smoothing (noise removal) due to the inherent edge preserving properties of the TV regularization. Since the random sampling of k-space in CS-MRI helps to make the artifacts appear noise-like (6), a denoising criterion like TV minimization constraint becomes a good choice for sparse reconstruction, especially when edge preservation properties are desired. Also, in applications like dynamic heart imaging, where the temporal variations (change in intensity of a pixel that happen over

scans at different timepoints) are highly sparse in the finite differences transform, this becomes a suitable reconstruction approach.

Despite contributing to an important role in CS-MRI, edge preserving approaches, especially that of TV, have some inherent shortcomings as well. For example, a very common drawback is the staircasing artifact (blocky effect) in the reconstructed image. Though it can be addressed by different methods like using second order finite differences in the reconstruction model (38-40), the sensitivity of reconstruction to the free parameters still pose as an important problem. Furthermore, the application of TV based functionals to some of the recently introduced data-driven learning based reconstruction models as an auxiliary constraint tend to become less efficient since its stand-alone reconstruction performance is inferior to that of these learning based approaches.

In a related work, Li (41) showed that the use of Perona-Malik (PM) diffusion in CS model has the potential to reconstruct a Shepp-Logan phantom from very limited set of samples in the Fourier domain. Theoretically, both TV and PM diffusion belong to the same broad area of non-linear (NL) diffusion models that exhibit inherent edge-preservation properties. Therefore, the appropriateness of using PM diffusion in CS-MRI applications is instantly noticeable. Though it shares similarities with TV, unique properties like enabling the user to set a threshold between edges and noise in the finite differences representation opens up promising possibilities in CS-MRI. This thesis is mainly inspired by these facts and investigates the application of NL diffusion, PM diffusion in particular, to CS-MRI reconstruction with a focus to address the

shortcomings that limit the efficiency of TV based edge preserving reconstruction techniques.

1.5 Original Contributions

The contribution in this thesis can be broadly viewed as the design and application of novel NL diffusion based CS-MRI reconstruction techniques with the goal of improved sensitivity to regularization parameters and improved diffusion updates that can generate high quality MR images. These are published as three papers in the journal Magnetic Resonance in Medicine and described in detail in chapters 3,4 and 5. A few specific points are listed below to give a short overview.

- **Reduced sensitivity to regularization parameter**

  The choice of regularization parameter (step-size) in TV based CS-MRI reconstruction requires prior tuning and if not properly tuned, it can lead to residual noise or increased blur in the reconstructed image. In an attempt to minimize this dependency of reconstruction to sensitive tuning of step-size, an alternative edge-preserving CS-MRI reconstruction model using biased PM diffusion is developed and discussed in detail in this thesis. The improved sensitivity is facilitated by the fact that the PM style of diffusion involves a contrast parameter that separates the gradient magnitudes attributed to noise and true edges in an image. Updating this parameter based on the changes in gradient magnitudes helps it to adapt to the reduction in artifacts that happen over iterations. This significantly reduces the sensitivity to regularization parameter, thereby removing the need for its search optimization.

- **Mitigation of second and fourth order diffusion artifacts**

  Staircasing artifact is a common outcome of denoising smooth regions of an image using second order partial differential equation (PDE) based techniques like the ROF model of TV (42). In the case of CS-MRI reconstruction using TV, however, countermeasures for staircase effect are already in place. Therefore, when an alternative edge-preserving reconstruction approach is introduced, it is important to also address the associated staircase artifacts. One generally considered notion to solve this problem is the use of second and fourth order PDEs in a combined fashion, for example, a weighted combination of individual solutions (43). However, like the second order diffusion, fourth order diffusion also introduces an artifact of its own that appears like speckles in the solution. This means that any attempt to remove the staircase/speckle after it has formed in the solution will be limited by the accuracy in estimation of both staircase and speckle effects in the image. Therefore, a new mixed-order PM diffusion based CS-MRI reconstruction model is developed that aims at preventing the formation of staircasing and speckle effects, rather than removing it after the artifacts are formed in the reconstructed image and is discussed in detail in this thesis. An illustration of staircase and speckle effects are shown in Fig. 1.5.

- **Subpixel diffusion correction and directionality guided diffusion model**

  Because of the complexity of structural details present in an MR image, the directional orientation of different edges can be spread across all possible angular directions. This is observed to have a significant influence on the local variations in the rate of diffusion. The conventional approaches do not tune the

reconstruction for these local variations and are therefore prone to miss important structural details in the image. Therefore, a new reconstruction model is developed that computes the gradients in all possible angular directions and use a spatial-frequency based deviation measure to choose the most reliable edges from the set of images diffused along different directions. For each individual edge, only the diffusion along its corresponding optimal direction is considered. This helps to adapt the direction of diffusion to local variations in the directionality of edges and employs a precise diffusion in the local regions of the image on a sub-pixel level, leading to the preservation of the complex nature of edges and therefore, much improved stand-alone finite difference sparsity based reconstruction performance.

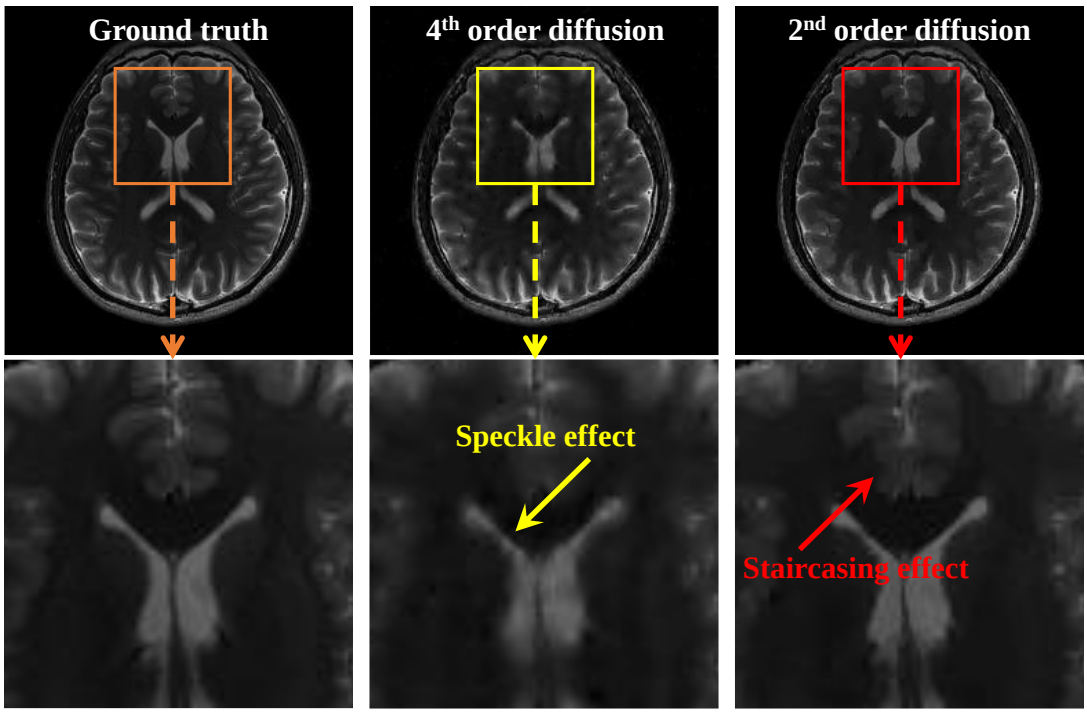

Figure 1.5. Illustration of staircase and speckle artifacts.

1.6 Thesis Organization

The remaining part of this thesis is organized as follows:

Chapter 2 presents the review of the literature related to MR image reconstruction leading to CS based techniques for sparse reconstruction.

Chapter 3 describes the theory and advantages of a newly developed PM diffusion reconstruction model for CS-MRI. Role of the associated diffusivity function, choice of parameters, biasing strategy and the significance of contrast parameter are discussed in detail. This is followed by the description of various numerical experiments that analyze the sensitivity to parameter tuning and reconstruction performance. Also, the reconstruction of in-vivo data using PM diffusion and TV at different acceleration actors are presented for comparative evaluation.

Chapter 4 describes the cause and remedial measures of the blocky effect (staircase) observed in the solution of second-order diffusion at high acceleration factors. This includes a summary of the advantages and challenges of regularizing the second-order PM diffusion reconstruction model using fourth-order terms, followed by a description of the biased mixed-order reconstruction model developed to address the blocky effect. The proposed reconstruction is shown to be stable for an experimentally determined range of the regularization parameter so that the advantages of second-order reconstruction model in terms of reduced sensitivity to the regularization parameters is retained.

Chapter 5 starts with a discussion of the factors limiting the performance of a typical NL diffusion reconstruction model and shows that the rate of diffusion for edges varies

in accordance with the direction of gradient computation. Since the directionality of edges varies at different regions of the image, an improved reconstruction technique is described that computes the gradients along all possible angular directions, and use a spatial-frequency based deviation measure to choose the most reliable edges from the set of images obtained by diffusion along these directions. The results are compared with different state-of-the-art data-driven learning based techniques to demonstrate the superior performance of the proposed reconstruction technique.

Chapter 6 summarizes the contributions of the work and discuss the limitations and the directions for potential future research to conclude this thesis.

Chapter 2

Literature Review

2.1 Early Days of MRI Reconstruction

The phenomenon of nuclear magnetic resonance (NMR) used in MRI was discovered by Rabi in 1938 (44). However, the possibility of multi-dimensional imaging by NMR physics came into the limelight later in 1973 when Lauterbur introduced gradient magnetic field to spatially encode the NMR signal generated from the nuclei of an object (45). It also forms the basis of signal localization in multidimensional Fourier imaging in MRI where the encoded signals represent the Fourier transform of the image of interest. On the downside, the gradient encoding technique restricts the number of positions of k-space that can be sampled at a time to one. This resulted in a relatively slow imaging speed which adversely affected the prospect of useful applications. Therefore, from late 1970s onwards, a cohort of attempts were made to accelerate the MRI (46). Due to the physical and physiological constraints that limits the speed at which k-space can be traversed, the approaches were soon streamlined to the idea of reducing the number of samples collected in k-space and estimating the skipped samples later.

2.1.1 Partial Fourier approach

Though the sampling theorem suggests that the signal needs to be sampled at least at Nyquist rate to generate an artifact-free image, the possibility of reducing the number of samples was motivated by the fact that some of the information in k-space is redundant. For example, if the MR image is a real-valued function, then its Fourier transform would exhibit a peculiar mirrored property known as Hermitian symmetry. It implies that only half of the k-space (partial Fourier) would then need to be filled because the other half would simply be its complex conjugate. This led to some of the initial partial Fourier methods like the works of Margosian et al. (47) and Cuppen et al. (48) where one collects slightly more than the half of k-space and estimate the remaining data to reconstruct the entire image. Scan time is saved by reducing the number of PE steps. Though not popular, partial data can also be collected in the FE direction by reducing the echo-time. In some of the later works, partial Fourier methods were extended to k-space truncated in both PE and FE directions as well (49-51).

In practice, the MR images are complex and the conjugate symmetry property is not perfect due to phase errors that arise due to different factors like susceptibility variations in tissues (52, 53) and unwanted variations in magnetic field (54-56). Therefore, the conjugate symmetry property was not sufficient for good reconstruction. Filling the locations of unacquired samples with zeros is the most basic approach to reconstruction. Usually referred to as the zero-filled reconstruction, this results in a trivial blurry image. A non-trivial solution was initially obtained by phase correction and conjugate synthesis method as shown in Fig. 2.1 where an estimate of

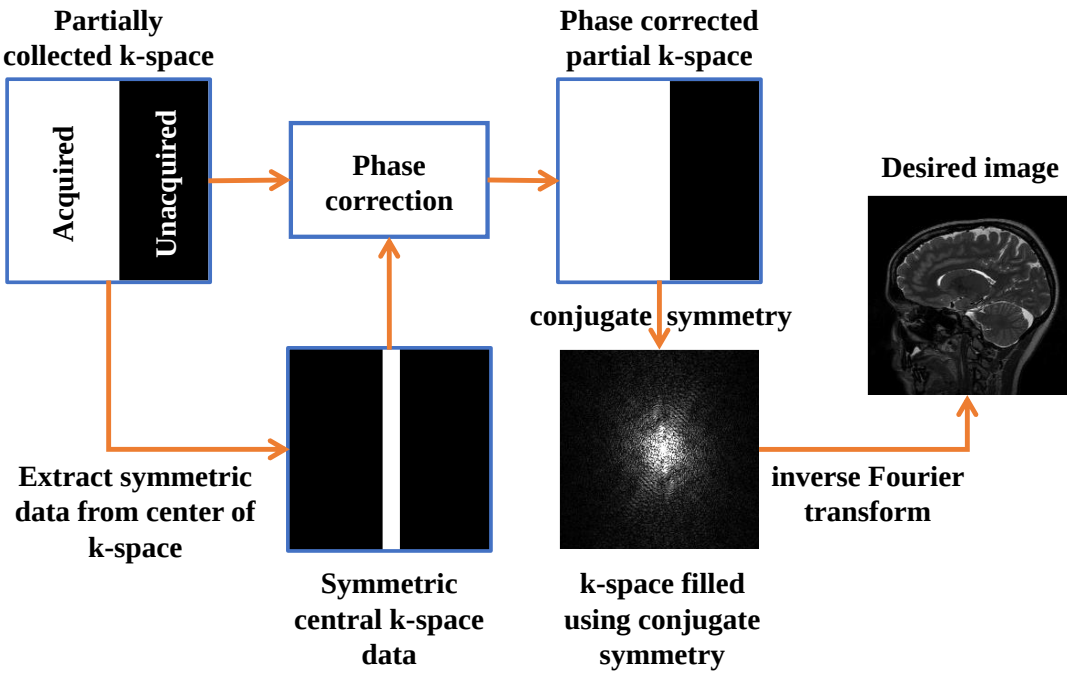

Figure 2.1. Phase correction and conjugate synthesis based partial Fourier MRI reconstruction workflow.

phase from the set of low spatial frequencies is used to correct the phase error, followed by k-space filling based on conjugate symmetry property. Since the low frequency information is required for phase correction, slightly more than half the k-space need to be collected in practice.

Noll et al. in (57) used a Homodyne algorithm for partial Fourier reconstruction, where the partial k-space is weighted before applying inverse Fourier transform to generate the image. After phase correction, the final image is obtained by keeping only the real part of the result. Pre-weighting of k-space here ensures that the real part of the result corresponds to a uniformly weighted k-space. This also eliminated the need for additional Fourier transforms in the phase correction and conjugate synthesis method for filling the k-space post phase correction. Cuppen et al and Haacke et al in

(48, 58) took another approach to reconstruction using iterative algorithms called projection onto convex sets (POCS) where the phase correction and conjugate synthesis are applied iteratively (59). Pauly in (60) reported that the homodyne approach introduces ghosting effect if the variations in phase of the image are not smooth and the POCS approach tend to generate better results than homodyne at higher undersampling rates.

2.1.2 Multiple coils for faster scanning

Among other approaches for reduced sampling that followed, the use of multiple receiver coils to collect fewer PE lines simultaneously in each coil stands out as the most significant (61-69). Though it accelerates the acquisition, it also introduces aliasing artifacts in the image. To address this issue, different parallel MRI (pMRI) reconstruction techniques were developed. An example of pMRI reconstruction workflow is shown in Fig. 2.2.

In 1997, Sodickson et al. (70) reported successful reconstruction using a technique called simultaneous acquisition of spatial harmonics (SMASH), in which a weighted combination of the signals acquired using multiple coils is used to recover the unacquired lines in k-space. Final image is then generated by Fourier transform. In 1999, Pruessmann et al (71) introduced sensitivity encoding (SENSE) method that directly recover the channel combined image free of aliasing using the knowledge of coil sensitivity profiles. This approach removed the restrictions on coil configurations present in SMASH. However, the desired performance generally requires an accurate knowledge of coil sensitivity profiles.

Another popular pMRI technique that followed is the generalized autocalibrating partially parallel acquisitions (GRAPPA) by Griswold et al (72) in 2002. Unlike SENSE, GRAPPA fills the k-space before Fourier transformation using a set of weighting factors estimated from the fully-sampled central region of the k-space. Therefore, it tends to perform better than SENSE in heterogenous body parts where an accurate coil sensitivity profile may not be available. However, at acceleration factors higher than 2 (acceleration factor 2 implies that every other PE line is skipped), SENSE is generally known to provide better image quality and slightly higher signal-to-noise (SNR) measures.

Over a short period of time, parallel imaging technique continued to become established as a standard approach for rapid MRI acquisition. Having been widely employed in most of the clinically used scanners, it brought about a major clinical impact.

2.2 CS Based Reconstruction

In early 2000s, the theory of CS started gaining interest in various fields of research. In 2004, Candès et al (1) proved that CS can correctly reconstruct a sparse signal from randomly measured Fourier coefficients with high probability. Though MR images are not always sparse when interpreted in the image domain, it is highly compressible in many transform domains like wavelets and curvelets. The idea of compressibility or induced sparsity here implies that a few large transform domain coefficients are sufficient to faithfully approximate the image without compromising the quality

standards required for clinical diagnosis. Remaining small coefficients can be safely discarded (set to zero). A typical CS-MRI reconstruction workflow is shown in Fig. 2.3.

The CS based idea of random undersampling and sparsity constrained reconstruction was introduced in MRI by some of the initial works like Lustig et al (6, 73), Block et al (7) and Jung et al (74). In the work of Lusting et al. (6) in 2006, called SparseMRI, randomly undersampled k-space data was reconstructed using wavelet and finite difference sparsity constraints. Specifically, the application to Cartesian sampling was investigated. The solution was obtained by minimizing the l_1-norm of wavelet coefficients and TV norm of the image. A standard TV regularizer minimizes the l_1-norm of image gradients. As dictated by the theory of CS, the sampling of k-space was made random to make the aliasing in the image 'incoherent'. Incoherence here implies that the aliasing appears noise-like. Incidentally, the noise-like information in the image transforms to smaller coefficients in the wavelet domain and can hence be easily thresholded off.

In an intuitive way, this work showed that if one could somehow force the artifacts in an MR image (resulting from the missing samples of k-space) to occupy the discardable transform domain coefficients, it can be eventually removed (due to the inducible sparsity of the signal in the transform domain) and thereby get away with the reduced sampling. It therefore showed promises in different MR imaging applications like the brain imaging where faster acquisition reduces the artifacts due to subject movement, rapid 3-D angiography where faster acquisition is better because the contrast of the flowing blood changes over time, whole-heart coronary imaging

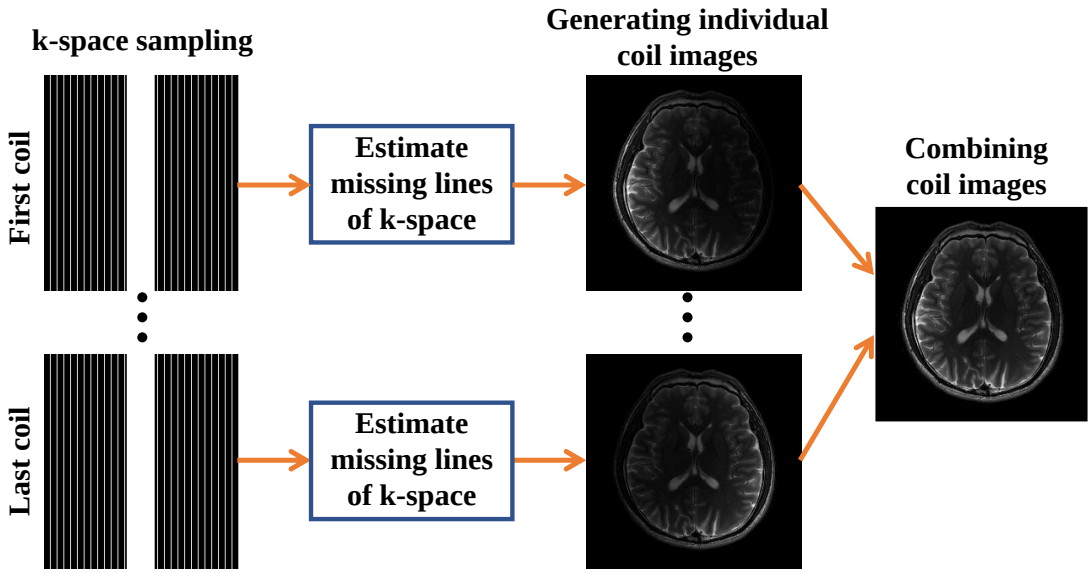

Figure 2.2. An example of pMRI reconstruction workflow.

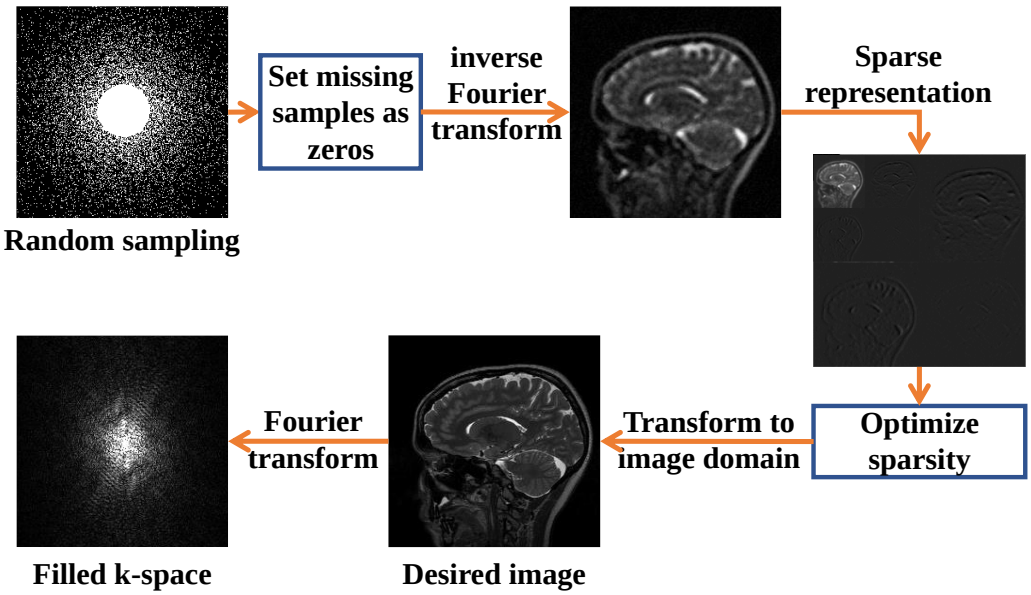

Figure 2.3. A typical CS-MRI reconstruction workflow.

where coronary arteries are constantly in motion and dynamic heart imaging where long acquisition times make it difficult to acquire images of heart due to its movement.

In another work (73), Lustig et al introduced sparsity based reconstruction in dynamic MRI where the objective is to image time varying objects like beating heart. Wavelet sparsity was used in this work as well. Alternatively, Jung et al in (74) used focal underdetermined system solver (FOCUSS) technique (75) to enforce sparsity in the solution by iteratively reweighting the solution based on the result from previous iteration, starting from a low resolution initial estimate. Performance of this approach is however dependent on the availability of a good initial estimate.

Around the same time, Block et al in (7) demonstrated the multi-coil reconstruction of radially undersampled k-space data in the CS framework using TV constraint alone. Even though the radial spokes were collected at uniform angular intervals, the sparsity enforcing TV constraint effectively removed the streaking artifacts caused by the undersampling. They also reported that the reconstruction is sensitive to the weight of TV constraint. When the weight is lower than the appropriate value, it resulted in residual artifacts/noise while higher weights (over-weight) introduced blur. In the works of both Lustig et al and Block et al, l_1-norm minimization was achieved using conjugate gradients method.

Despite the sensitivity of reconstruction to the choice of TV weight, it showed promising edge preservation properties. Therefore, it continued to be a popular choice of sparsity constraint in CS-MRI along with wavelet.

2.2.1 CS in combination with partial Fourier and pMRI

These realizations of CS-MRI led to the proposal of several methods combining CS with partial Fourier, SENSE and GRAPPA type reconstructions in the late 2000s (76-81) and early 2010s (82-87). These methods in general showed that the combined approach can achieve robust reconstructions at higher acceleration factors compared to traditional pMRI or CS-MRI techniques. Lustig et al. (81, 85) proposed a GRAPPA based method called iterative self-consistent parallel imaging reconstruction (SPIRiT) for arbitrary sampling patterns which allows additional sparse constraints like TV and wavelet in the formulation. Results indicated significant noise reduction compared to GRAPPA. Liang et al. (80) proposed a method called CS-SENSE which used SpraseMRI to reconstruct aliased channel images and SENSE to reconstruct the final image. In another work, Doneva et al. (82) combined partial Fourier and CS by enforcing sparse constraint in each iteration of POCS. Liu et al. (84) combined CS-SENSE with partial Fourier to show that it can provide better reconstructed image if only the magnitude data is desired.

2.2.2 Improved reconstruction by sparser representation

Different techniques to improve the CS-MRI reconstructions were also evolving in the meantime. According to CS theory, sparser representation leads to better reconstruction quality and for a given reconstruction quality, better sparsity allows greater acceleration (88). Therefore, sparse representations and sparsity regularizations were rigorously investigated. Besides wavelet transform and finite differences, transform domains like discrete cosine transforms, Shearlet transform (89,

90), and contourlet transform (91) were also explored. Each of these sparsity constraints essentially incorporate different prior knowledge into the reconstruction framework. For example, while wavelets represent point like features better, curvelet and contourlet gives better representation of edges and curves.

Qu et al. in (92) used both wavelet and contourlet transforms together to improve the reconstruction than either transforms when used independently. An additional TV constraint showed further improvement in the quality of reconstructed image measured using peak signal-to-noise ratio (PSNR). Specifically, the combination of wavelets, contourlets, and TV showed better PSNR measures compared to that of wavelets and TV. In another work, Li (41) used a PM Diffusion function instead of TV for edge preserving reconstruction. He showed the reconstruction of a Shepp–Logan phantom from 8 radial lines. However, the reconstruction of in-vivo data was not investigated and it assumes bilateral symmetry in the images for non-local processing, which might not always be valid.

2.2.3 Countermeasures for blocky effects in TV

Though the TV constraint helps to preserve edges, it assumes that the image is piecewise constant. Therefore, it tends to introduce blocky effect (also known as staircasing artifacts) in the solution, especially at higher undersampling rates. Considering the significance of the role played by TV in sparsity based reconstructions, several countermeasures were proposed in the form of higher order derivatives of the image or by methods like non-local TV (NLTV) that uses a weighted nonlocal gradient function instead of TV (38-40, 93).

One of the popular solutions is the second order total general variation (TGV) (94) functional proposed by Knoll et. al. (40) which uses second derivative of the image in the regions of smooth intensity variations and first derivative in the neighborhood of edges. Since the second derivative will be small in the smooth regions compared to first derivative, it will not cause blocky effect. One the flipside, if only the second derivatives are used, it tends to introduce speckle-like effects in the solution. Therefore, a functional combining both first and second derivatives is generally preferred. In another approach, Hu and Jacob (38) proposed higher degree total variation (HDTV) technique which works by minimizing the sum of absolute magnitude of the directional derivatives along all angles and pixels in the image. This approach also showed good resistance to blocky effects.

2.2.4 Learning the sparsity basis for improved sparsity

In further attempts to improve the sparse representation, data-driven learning was introduced which can adaptively learn the sparse representation of image (95-98). An important development in this direction was the use of dictionary learning based sparsity basis (99-101), where the main idea is to use an adaptive data-specific sparsifying transform instead of global ones like Daubechies wavelets and TV, owing to its success in applications like denoising and inpainting (102-105). Basic elements in a sparsifying dictionary are called atoms, whose linear combinations can represent a given signal in sparse form.

In some of the initial applications to CS-MRI reconstruction like Bilgin et al. (106) and Chen et al. (107) during 2010, dictionaries were learned from patches of

previously acquired MR images (reference image) using K-SVD algorithm (100) which updates the dictionary, atom by atom, in an iterative manner. In each iteration, sparse coefficients are updated based on the current estimate of the dictionary and the dictionary atoms are updated to best fit the current sparse representation of the data. Though it improved the reconstruction compared to methods that use fixed sparsity basis, Ravishankar et al. (96) pointed out that the dictionary learnt from such a reference would have limited abilities to sparsify new features in a new scan. Instead, they proposed a K-SVD based adaptive scheme called DLMRI, to adaptively learn the dictionary from zero-filled reconstruction of sampled k-space data. It also performed better than the one-dimensional (1D) dictionary learned using K-SVD from the wavelet sparsity based reference reconstruction by Otazo and Sodickson (108). Superior performance of DLMRI in this case is attributed to the limited capability of 1D dictionary to exploit the 2D local structures in the image.

The fact that multiple sparsity constraints can lead to improved results encouraged the researchers to also use fixed sparsifying transforms alongside learned dictionaries for CS-MRI reconstruction in the mid-2010s (88, 109-111). While Caballero et al. (88) achieved improved results by enforcing finite difference sparsity along temporal direction in dynamic MRI, Wang and Ying (111) applied TV constraint along PE, FE and temporal directions to achieve better results.

In other attempts, superior sparsifying dictionaries were learned from transform domain representation of the data. For example, Ophir et al. (112) learned the dictionary from patches of wavelet coefficients and Liu et al. (113) trained the dictionaries from finite difference representation (horizontal and vertical gradients) of

the image to achieve better results compared to DLMRI. These works indicate that the dictionaries learned from sparser training samples can improve its accuracy and robustness.

2.2.5 Learning the data representation for improved sparsity

The idea of data-driven learning based reconstruction was also realized in the form of modifying the data rather than modifying the sparsity basis. In 2010, Qu et al. (97) introduced a patch-based directional wavelets (PBDW) method to improve the sparsity by image domain pixel rearrangement. Here, the image is divided into several overlapping patches and the pixels in each patch are rearranged into a 1D vector such that the coefficients of its 1D Haar wavelet transform decays faster. Ning et al. (114) modified this method in 2013 for improved sparsity by applying PBDW on the individual subbands of two-dimensional (2D) shift-invariant discrete wavelet transform of the image instead of applying directly on the image.

Later in 2014, Qu et al. (115) introduced a patch-based nonlocal operator (PANO) that operates on a group of similar patches rather than individual patches of the image. They grouped similar 2D patches in a three-dimensional (3D) arrangement and applied a 3D wavelet transform. The sorted wavelet coefficients decayed faster than its 2D wavelet counterpart resulting in a superior image quality. Either a zero-filled reconstruction or a conventional CS-MRI reconstruction was used here as a reference to learn the non-local similarity. A similar approach using the block matching and 3D filtering (BM3D) (116) was proposed by Eksioglu (117) in 2016. In this work, blocks formed by grouping similar patches are sparsified using a separable 3D wavelet

transform. Specifically, a bi-orthogonal spline wavelet transform is applied to individual 2D patches and a 1D Haar wavelet transform is applied over the third dimension. Reconstruction of in-vivo data showed improved signal-to-noise (SNR) compared to PANO. It is also shown that a sequential decrease in regularization parameter enables the algorithm to converge to better reconstructions.

Around the same time, Lai et al. (118) proposed a graph based redundant wavelet transform (GBRWT) that combines a graph based method (119, 120) and redundant wavelet transform to achieve better results than PANO. In this method, wavelet transform is applied on the patches ordered according to the shortest path on a graph formed by considering patches as vertices and their differences as edges. It is shown that reordering the pixels based on the shortest path on graph leads to faster decay of wavelet coefficients. However, at high acceleration rates, very limited information is available to construct a graph, which limits its performance (121).

2.2.6 CS in combination with low-rank representation

In other related works, sparse reconstruction techniques were also implemented in combination with low-rank approximation (122) of MR images (123-126). These methods consider the underlying signal to be both sparse and rank deficient. The low-rank constraint is enforced by minimizing Schatten *p*-norm or nuclear norm of the data matrix in place of the sparsity constraint (l_p-norm minimization) in CS problems (123, 127). For a matrix X of size $m \times n$, the Schatten p-norm is defined as $\|X\|_p = \left(\sum_{i=1}^{\min\{m,n\}} s_i(X)^p\right)^{1/p}$, where $s_i(X)$ are the singular values of X and the nuclear norm is its special case when $p = 1$. Recently, Yao et al. (128) has reported that the use of

TV constraint with low-rank regularization can make the reconstruction of cardiac cine data less sensitive to noise.

The idea of rank constraint is also implemented in the form of structured low-rank approximation alongside sparsity constraints for pMRI (129). This approach tries to exploit the rank deficiency in structured matrices by rearranging the signal samples in multi-coil k-space data to form a structured matrix like Toeplitz or Hankel (126, 130-132). It also makes use of the fact that local k-space correlations in multi-coil data reduces the rank of the matrix. Individual coil k-space data is also shown to be rank deficient in Hankel structured matrix form by Haldar (133, 134) when the underlying channel image contains smoothly varying phase or has a limited spatial support.

2.2.7 Recent trends in MRI reconstruction

Most recently, the reconstruction problem in MRI is rapidly shifting its focus towards deep learning based techniques due to the possibility of real-time reconstruction (135-140). These techniques involve a separate training phase to learn the reconstruction parameters. The significant gain in reconstruction time is mainly because the computation demanding training phase is performed offline. However, the computing power requirements and limited availability of large enough database for training presently pose as a limitation of these methods.

2.3 Summary

Across this review, the presence of finite difference sparsity constraint in the form of TV minimization is clearly noticeable. Though it is used as a standalone reconstruction

method in some of the earlier works like Block et al (7), it became more popular in the role of an auxiliary constraint in the later part of the literature. In this new role, it helps to preserve the edges sharp while other constraints like learned dictionaries tries to approximate the underlying MR image as a smooth function. Despite this important role, minimal effort can be seen to improve its standalone performance in the context of MRI reconstruction to match with some of the more recent state-of-the-art works. Though Li pointed out the possibility of PM diffusion as an edge-preserving regularizer (41), it wasn't investigated any further either. Furthermore, the sensitivity of the reconstruction to the choice of TV weight remains problematic. Due to the superior stand-alone performance of sparsity constraints like learned dictionaries, it also becomes imperative that any edge preserving auxiliary constraints if used, need to perform at a similar level for an efficient reconstruction. The original contributions of this thesis discussed in the next three chapters tries to address these issues.

Chapter 3

Perona-Malik Diffusion Reconstruction

3.1 Introduction

Preservation of structural details is often one of the important requirements while reducing noise in MR images, since it contains important anatomical information that can aid in clinical diagnosis. Non-Linear (NL) diffusion is one such well-known and well-studied denoising technique (42, 141) commonly used to facilitate the edge preservation feature. It is known to be an effective tool to remove Rician and speckle noise in MR images (142, 143) and has also proved to be helpful in compensating for the loss in Signal-to-Noise ratio (SNR) at high spatial resolutions, which reduces the need for averaged multiple measurements of the same object (144).

It describes the popular edge-preserving denoising technique of TV minimization (6, 37, 94) as TV diffusion, widely used in CS-MRI reconstruction problems. Recently, the use of NL diffusion using Perona-Malik (PM) diffusivity has been shown to be effective in reconstructing Shepp-Logan phantom from as few as 8 radial spokes (41). Because of the edge preserving property, both methods have an advantage that the diffusion process will not affect the edges where the image gradient values are

significantly high. Since the gradient magnitudes due to noise in an image is generally smaller than that of true edges, the image is processed in such a manner that the regions having relatively smaller gradient magnitudes are smoothed, while those having larger gradient magnitudes are preserved.

Even though TV is a more popular choice when it comes to edge preserving sparse reconstruction, its performance is often found dependent on the right choice of regularization parameter as well. In this work, a biased form of NL diffusion using PM diffusivity function is introduced to address the MR image reconstruction problem. The statistical estimation of contrast parameter in the proposed method removes the need for searching the critical parameters as in the case of a TV based reconstruction. Considering the wide application areas of TV based strategies in MRI like elimination of truncation artifacts and regularizing Compressed Sensing (CS) imaging techniques (6, 145), the use of NL diffusion as an alternative serves the purpose better.

The chapter is organized into four sections. First section gives a brief overview of the CS reconstruction model using NL diffusion. It describes the theory of NL diffusion, biasing strategy, relation to TV and application to parallel imaging. Next section outlines the description of proposed algorithm and choice of parameters required for implementation. This is followed by a Results section which shows the effect of contrast parameter, sensitivity to regularization and advantages of NL diffusion over TV in learned reconstructions using in vivo data. The chapter concludes with a detailed discussion of its implications and relative advantages.

3.2 Theory

3.2.1 CS Reconstruction model using NL diffusion

CS reconstruction problem is addressed in this work as a biased form of NL diffusion. Given the acquired samples in k-space K, a general edge preserving CS reconstruction method works by minimizing a cost function of the form

$$C(U) = \mathcal{H}(U) + D(U, K), \quad [3.1]$$

where $\mathcal{H}(U)$ is an edge cost that imposes explicit penalty for edges in image U and $D(U, K)$ is a deviation cost ensuring the estimated image to be a faithful approximation of the ideal image. In the proposed method, NL diffusion is used to selectively diffuse noise while preserving significant edge features in the image. Here noise refers to the intensity variations in image introduced by the undersampling of k-space and not to be confused with the noise in acquisition which will be explicitly referred to as 'inherent noise in acquisition'.

Biasing is introduced to ensure that the deviation cost is minimized. This is equivalent to minimizing the cost function

$$\mathcal{H}(U) = \int_{\Omega} f(|\nabla U|) d\Omega, \quad [3.2]$$

subject to the constraint $\|\mathcal{F}_u U - K_u\|_2 < \varepsilon$, where Ω denotes the image domain and $f(|\nabla U|)$ is an increasing function of $|\nabla U|$, that is, $f'(|\nabla U|) > 0$. $K_u = Q \circ K$ for a binary sampling matrix Q that sets the unacquired samples in K as zero. The constraint biases the diffusion to ensure that the solution does not deviate from the ground truth image. $\mathcal{F}_u$ operating on U computes its Fourier Transform followed by setting the

unacquired frequency points to zero. ε controls the fidelity of reconstruction to K_u. Detailed explanation of NL diffusion and the biasing strategy is presented in the subsequent section.

3.2.2 NL diffusion

NL diffusion works on an image by removing unwanted intensity variations in the uniform intensity regions and enhancing edges. From the fact that the difference between an image and its blurred version is proportional to the Laplacian (146), the process of diffusion can be represented in the form of forward heat equation

$$\partial_t U = \omega \nabla^2 U, \qquad [3.3]$$

where ω is the diffusion coefficient and ∇^2 represents the Laplacian of an image U. It measures the extent by which U diffuses over a small time ∂t. In the context of numerical implementation, ∂t represents time between two successive diffusion iterations. This operation, however, does not distinguish between edges and uniform intensity regions in an image, leading to the resultant blurring of edges as well. Alternatively, subtracting a fraction of Laplacian from an image deblurs it (reverse diffusion) (147).

$$U_{deblurred} = U_{blurred} - \lambda \nabla^2 (U_{blurred}). \qquad [3.4]$$

Together with the edges, this reverse operation is known to enhance noise in the image as well. In a noisy image, the desired processing is a combination of both forward and reverse diffusion, enabling noise removal without diffusing the edges. This is achieved by NL diffusivity functions which diffuse the uniform intensity

regions forward and edges backward simultaneously (42). The combined form of diffusion as presented in (148) is

$$\partial_t U = div(g(|\nabla U|)\nabla U), \quad [3.5]$$

where $g(|\nabla U|)$ represents the diffusivity function and div is the divergence operator. An example of g proposed by PM is

$$g(|\nabla U|) = \frac{1}{1+(|\nabla U|/\alpha)^2}, \quad [3.6]$$

where α is the contrast parameter that separates the gradient magnitudes of noise and edges in an image.

From the theory of NL diffusion, diffusivity function $g(|\nabla U|)$ is chosen to be positive and monotonically decreasing, so that the amount of diffusion decreases as $|\nabla U|$ increases (42). Consequently, as the gradient magnitudes become large, $g(|\nabla U|)$ approaches zero and the diffusion is stopped. The flux function $g(|\nabla U|)|\nabla U|$ computed in Eq. [3.5] is increasing for $|\nabla U| < \alpha$ and decreasing for $|\nabla U| > \alpha$. Hence its derivative becomes positive when $|\nabla U| < \alpha$ and negative for $|\nabla U| > \alpha$. This leads to a forward or backward diffusion depending on the value of $|\nabla U|$ relative to α. Therefore, Eq. [3.5] modifies the edges and uniform intensity regions of U differently. This results in a diffused image given by

$$U_{diffused} = U + \gamma \partial_t U, \quad [3.7]$$

where γ is a regularization parameter which controls diffusion strength. When the gradients of an image are calculated along vertical and horizontal directions, the numerical scheme of PM diffusion becomes stable when $0 < \gamma < 1/4$ (148). This will

lead to a sequence of diffused versions of the initial image $U^{(0)}$ by repeatedly diffusing the image.

The diffusion is made dependent on the magnitude of the image gradient to retain structural information. Continued diffusion will finally result in a constant (all edges diffused off). Best result is obtained when artifacts are removed with maximum preservation of the structure. Hence it becomes important to decide when to stop the diffusion process. In addition, the stability of this process depends on its ability to discriminate the gradient magnitudes corresponding to edges and noise. Both these issues can be addressed and the process can be made stable by biasing the algorithm towards original image using the constraint in Eq. [3.2] (149). It enforces consistency with the acquired Fourier measurements. With the inclusion of bias term, diffusion of U becomes

$$\partial_t U = div(g(|\nabla U|)\nabla U) + \beta \mathcal{F}_u'(K_u - \mathcal{F}_u U), \qquad [3.8]$$

where β is a bias relaxation factor and $\mathcal{F}_u'$ operating on k-space computes its inverse Fourier transform after setting the unacquired frequency points to zero ($\mathcal{F}_u'(K) \triangleq \mathcal{F}^{-1}(Q \circ K)$.

Biased diffusion can be intuitively interpreted from the fact that while the diffusion process tends to remove the edges, bias introduces structural information into the current solution, such that the diffusion process does not impair this underlying structure in the next iteration. This stabilizes diffusion and forces the process to converge towards a solution that is consistent with the acquired k-space data instead

of a constant, thereby removing the need for a stopping criterion. Substitution of $\partial_t U$ from Eq. [3.8] into Eq. [3.7] yields

$$U_{diffused} = U + \gamma div(g(|\nabla U|)\nabla U) + c\mathcal{F}_u'(K_u - \mathcal{F}_u U), \quad [3.9]$$

where $c = \gamma\beta$ is the updated bias relaxation factor. This also minimizes the unconstrained form of functional in Eq. [3.2] (42, 150).

3.2.3 Relation to TV

Based on the choice of diffusivity function, the filter in Eq. [3.5] varies. The numerical scheme of NL diffusion becomes equivalent to TV when the diffusivity function used is (151)

$$g(|\nabla U|) = \frac{1}{|\nabla U|}. \quad [3.10]$$

While PM diffusivity form allows to control the diffusion using a contrast parameter, the TV form does not include this option. In the results section, it is shown that this is a crucial factor that allows PM diffusion to adapt to the changes in the noise contained in a dataset.

3.2.4 Application to parallel imaging

When the data is collected using multiple coils, we get only partial information from individual channels. Hence the estimation of α from individual channels may not be efficient because the complete structural information is absent in any single channel and the presence of channel sensitivity degrades the quality of true edges. Therefore, it is preferred to estimate the contrast parameter from combined channel information

($\overline{U}$). Ideally, α should be smaller than the smallest gradient corresponding to the true edges. A workflow of the proposed technique is shown in Fig. 3.1.

3.3 Methods

3.3.1 Reconstruction parameters

Parameters which control the reconstruction performance include (i) relaxation parameter c, (ii) diffusion strength γ, and (iii) contrast parameter α. α is estimated using mean/median absolute deviation (MAD) of ∇U or the noise estimator described by Canny (141). In latter, α is set as 90% value of cumulative sum of the histogram of $|\nabla U|$ in every iteration, so that it will automatically get adjusted to the changes in the image. In literature, both mean and median absolute deviations are abbreviated as MAD. Both are known to be robust estimators because the extreme gradient values have less influence on α (152, 153). Mean absolute deviation being computationally simpler than median absolute deviation, MAD using mean to estimate α is used in this work. It computes the average variation of data (∇U) about its mean.

$$MAD(\nabla U) = mean(|\nabla U - mean(\nabla U)|) \quad [3.11]$$

Implementation using Matlab (The MathWorks, Inc., Natick, MA, USA) shows a two-fold gain in speed with mean as compared to MAD using median.

Choice of c and γ: c and γ are parameters common to both TV and PM diffusion based image reconstruction. In TV, γ is referred to as the step size. While role of c is to minimize the effect of acquisition noise in the reconstructed image, γ controls the extent of diffusion in a single iteration. Typically, γ is determined by solving Eq. [3.2]

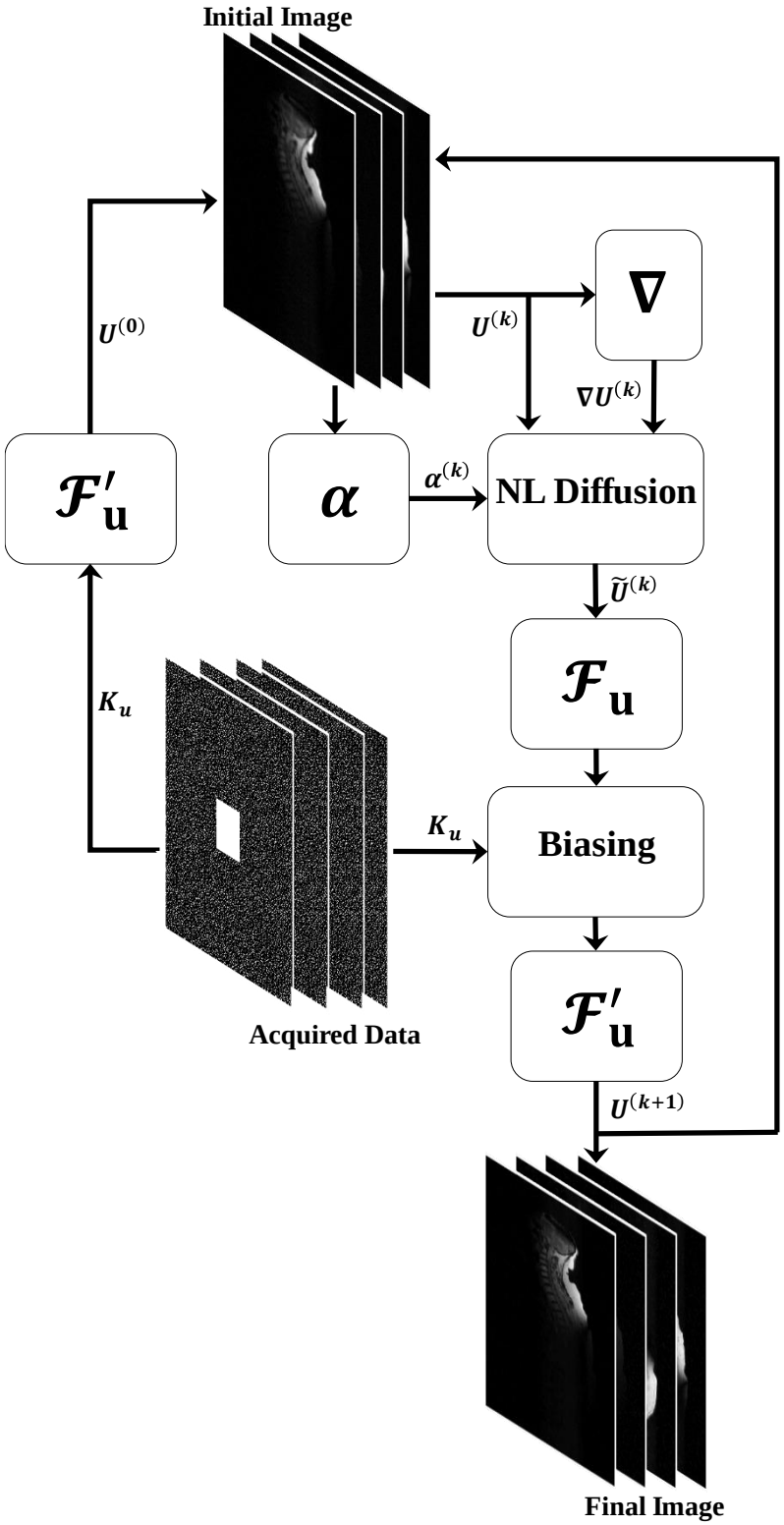

Figure 3.1. Workflow of statistically optimized non-linear diffusion reconstruction.

for different values of γ and selecting the value which minimizes the deviation cost (6). Other methods based on discrepancy principle usually requires the knowledge of noise variance and is reported to oversmooth the solution (154). In the proposed method, adaptation of contrast parameter (α) overcomes the need to fine tune the value of γ, making it a soft parameter. This is not possible in TV based reconstruction.

Relaxation of c in both TV and PM diffusion is desired when the acquired data is noisy. Since there are no known methods to a priori fix the best possible value of c in such cases, the best choice is to monitor the final reconstructions corresponding to different values of c. This adds to the complexity of search in TV reconstruction because it would then require an additional tuning of γ for each c value. Since the reconstruction would converge to a solution that is most consistent with the noisy ground truth image when c is set to 1, it is meaningful to fix the value of c and search for γ that minimizes the effect of inherent noise. Adaptation of α helps to minimize this remnant noise in PM diffusion when c is set to 1. In this manner, the proposed method overcomes the critical requirements for parameter tuning as compared to TV based reconstruction.

3.3.2 Implementation

A proximal forward-backward splitting method is used to implement the technique where biasing and PM diffusion forms the forward and backward steps. The resultant reconstruction framework is given in algorithm 3.1. The acceleration technique of fast iterative soft thresholding algorithm (FISTA) (25) is used to speed up the reconstruction process in steps 6 and 7.

Algorithm 3.1:

0: Set $k = 1$; $t^{(1)} = 1$; % 'k' is the iteration number

1: $U_i^{(0)} = \mathcal{F}_u' K_{u,\ell}$; % '$\ell$' is the channel number

2: $while\ (k < k_{max})$

3: $\widehat{U}_\ell^{(k)} = U_\ell^{(k-1)} + c\ \mathcal{F}_u'\left(K_{u,\ell} - \mathcal{F}_u U_\ell^{(k-1)}\right)$; % biasing

4: $\alpha = MAD\left(\nabla \overline{U}^{(k)}\right)$;

5: $\widetilde{U}_\ell{}^{(k)} = \widehat{U}_\ell{}^{(k)} + \gamma div\left(g\left(\nabla \widehat{U}_\ell{}^{(k)}, \alpha\right) \nabla \widehat{U}_\ell{}^{(k)}\right)$; % diffusion

6: $t^{(k+1)} = \left(1 + \sqrt{1 + 4(t^{(k)})^2}\ \right)/2$;

7: $U_\ell^{(k)} = \widetilde{U}_\ell{}^{(k)} + \left(t^{(k)} - 1\right)\left(\widetilde{U}_\ell{}^{(k)} - \widetilde{U}_\ell{}^{(k-1)}\right)/t^{(k+1)}$; % acceleration

8: $k = k + 1$;

9: end

3.3.3 Evaluation

The error in reconstruction is computed using the relative *l*2 norm error (RLNE)

$$RLNE = \left\|U^{(k)} - U_{ref}\right\|_2 / \left\|U_{ref}\right\|_2, \qquad [3.13]$$

where U_{ref} is the ground truth image.

3.3.4 Datasets

Different in-vivo datasets used in this work are shown in Fig. 3.2(a–e). Datasets I-III (Fig. 3.2(a-c)) are single channel brain datasets shared freely at

http://www.quxiaobo.org/. Datasets IV-V (Fig. 3.2(d-e)) are four-channel spine (T2-weighted spin echo sequence; TE = 98ms, TR = 5520ms, slice thickness = 3.0mm, FOV = 230mm) and six-channel brain (FLAIR spin echo sequence; TE = 89ms, TR = 9000ms, Inversion time (TI) = 2500ms, slice thickness = 5.0mm, FOV = 240mm) data acquired using Siemens 1.5T Magnetom-Avanto clinical MR scanner at Sree Chitra Tirunal Institute of Medical Sciences and Technology, Trivandrum, India. All subjects were scanned with prior written informed consent as recommended by the institutional ethics committee. The fully sampled brain images were acquired with phased-array head coils and spine images with spine-array coils. An example of sampling mask used to retrospectively undersample the k-space data is shown in Fig. 3.2f. Channel images of datasets IV-V are shown in Fig. 3.2(d1-d4, e1-e6).

3.4 Results

All implementations are performed using Matlab (The MathWorks, Inc., Natick, MA, USA) on a PC with an Intel Xeon E5-2609 2.4 GHz processor and 16 GB of RAM running Windows 7 operating system.

3.4.1 Effect of contrast parameter

Plots in Fig. 3.3(a-e) compare the reconstruction errors of datasets shown in Fig. 3.2(a-e) for different values of contrast parameter (α). For all datasets, large values of α result in increased convergence rate and vice-versa. However, fast convergence is obtained at the cost of large steady-state errors. When the inherent noise is low, improved image quality can be achieved using small values of α (Fig. 3.3(a-c)). If the noise is more,

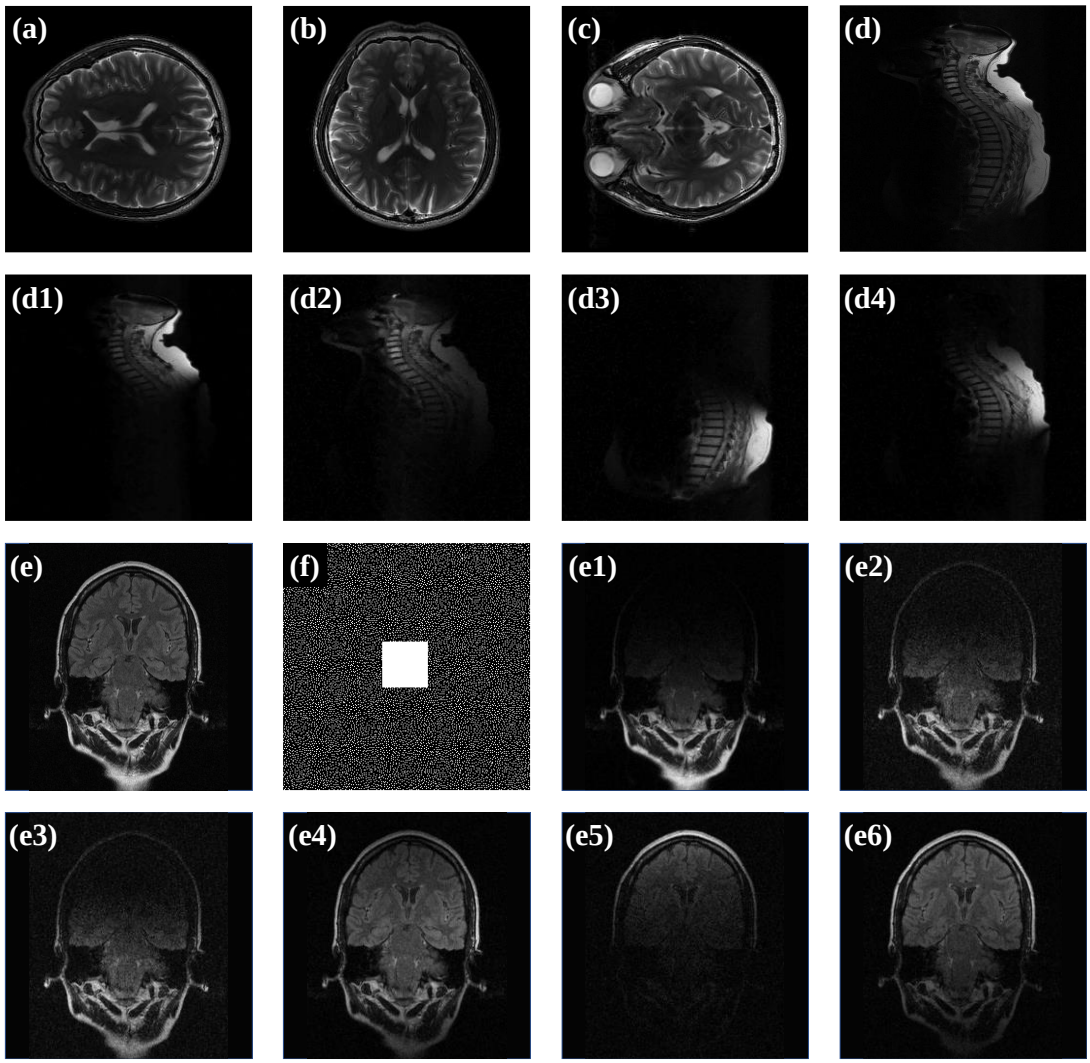

Figure 3.2. Retrospective sampling schemes and fully sampled reference images. (a)-(c) T2-weighted single channel brain image, (d)-(e) channel combined spine and brain data, (f) 20% sampled Poisson disk sampling mask, (d1)-(d4) channel images of multichannel spine data, (e1)-(e6) channel images of multichannel brain data.

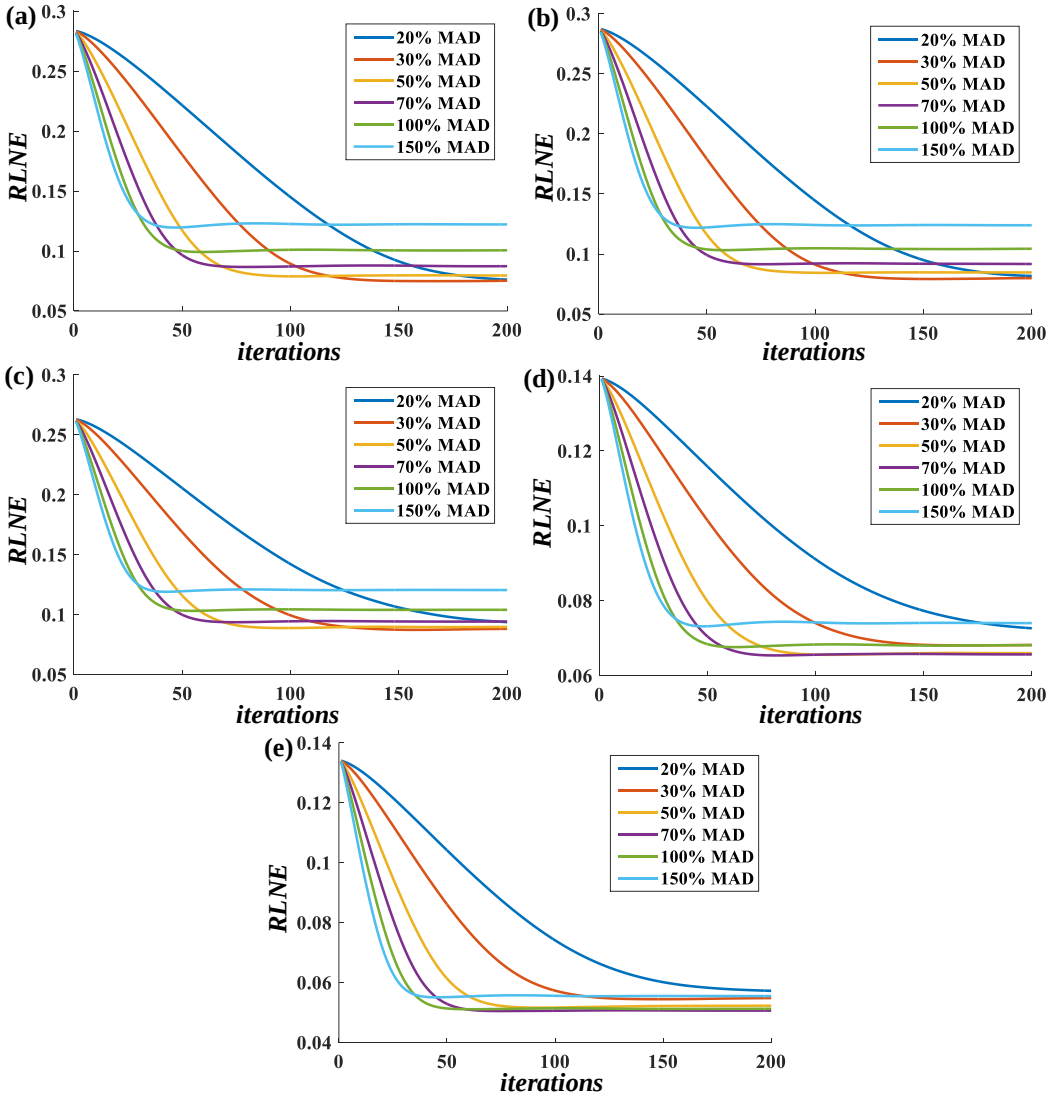

Figure 3.3. Reconstruction errors obtained for different values of α expressed as fractional multiples of MAD(∇U) as a function of iteration number. Plots (a)-(e) correspond to the datasets shown in Fig. 3.2. (a)-(e).

biasing maintains consistency with the noisy acquired samples. Hence the output image of data consistency step (biasing) in each iteration tends to be noisy. In such cases, small values of α tend to preserve this noise resulting in higher steady-state errors (Fig. 3.3(d-e)). In all cases, a good compromise of speed and quality is achieved when α is set as 50% MAD.

3.4.2 Sensitivity to regularization

With c set as 1, the sensitivity to regularization (γ) for TV and PM diffusion is investigated by addition of complex Gaussian noise to the Shepp-Logan phantom. Fig. 3.4 shows plots of RLNE versus gamma for different noise levels. While PM diffusion results in low steady-state errors for a wide range (.01 to .25) of the permissible values of γ (0 to .25), TV is highly sensitive to the change in γ and yields low steady-state error for only a narrow range of γ (.0005-.0030).

3.4.3 Reconstruction of multi-channel data

Reconstructions of spine and head images in Figs. 3.5-3.6, illustrate the need for step size tuning in TV based reconstruction as compared to a statistically optimized PM based reconstruction using a constant step size for 3, 4 and 5-fold accelerations (row-wise panels). Column-wise panels show the zero-filled, PM diffusion, and TV reconstruction together with their respective error images. The zero-filled reconstruction is performed by filling the unacquired locations with zeros followed by inverse Fourier transformation of this zero-filled k-space. For spine data with 3-fold undersampling, an optimal step size in TV based reconstruction is first obtained using

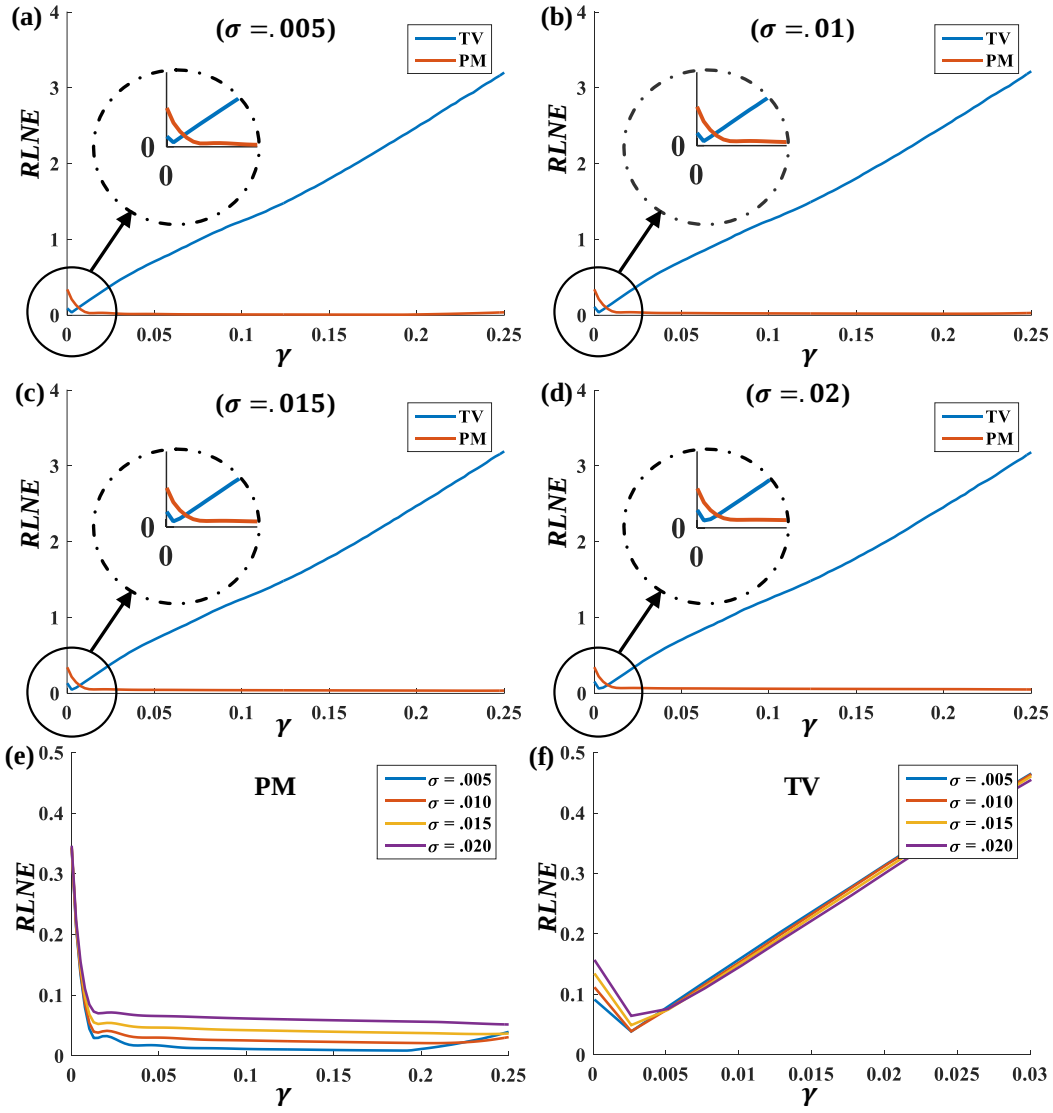

Figure 3.4. Plots of reconstruction error at a predetermined number of iterations (k=100) versus step size for different input noise levels. α is chosen as 30%MAD. (a)-(d) compares TV and PM diffusion for a fixed noise level. Comparisons at different noise levels are provided in panels (e)-(f), which indicates that the PM diffusion results in low steady-state errors for a wide range (.01 to .25) of the permissible values of γ (0 to .25) while TV is highly sensitive to the changes in γ and yields low steady-state error for only a narrow range of γ (.0005-.0030).

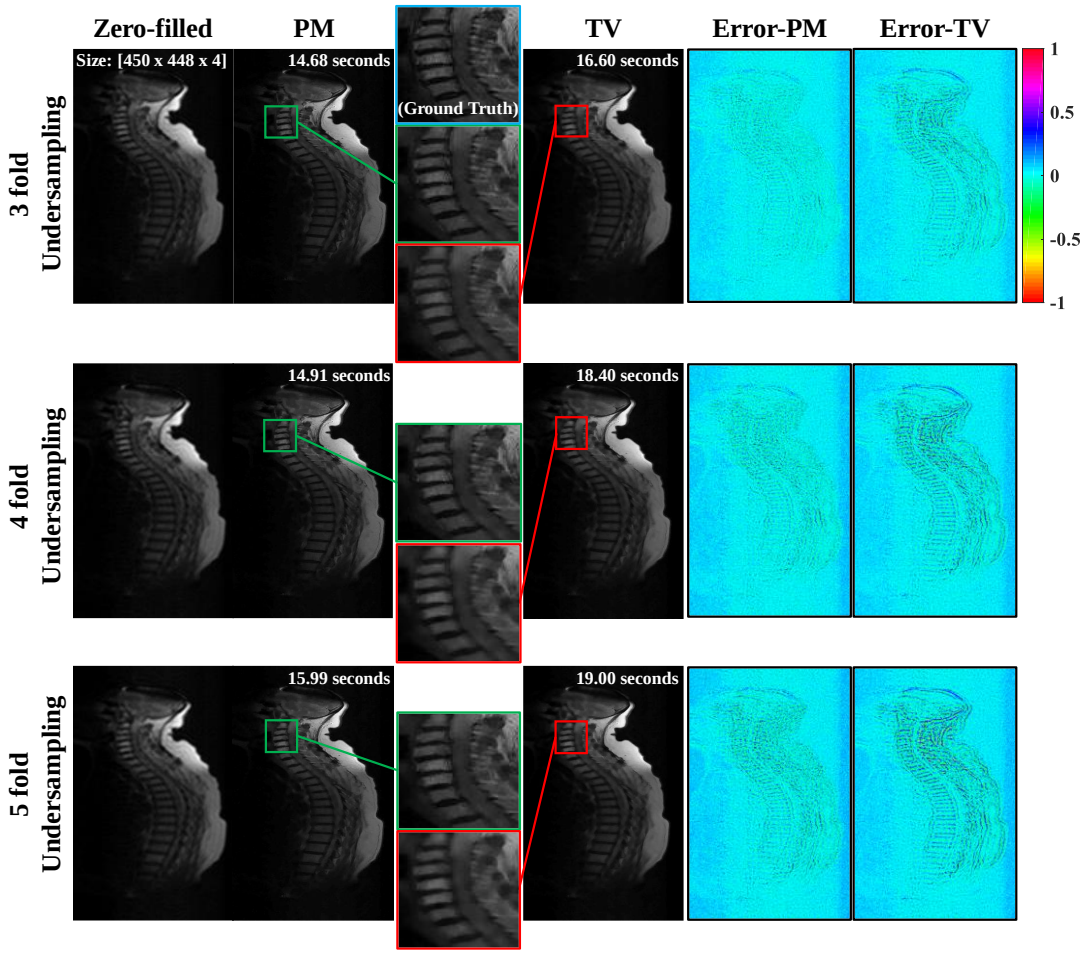

Figure 3.5. Reconstruction using dataset-IV for 3, 4 and 5-fold retrospective subsampling using PM diffusion and TV. Column-wise panels show the results of zero-filled reconstruction, PM diffusion based reconstruction, TV reconstruction and the respective error images of PM diffusion and TV. Computation time (excluding step size search) and matrix size are shown in insets. Panels in first, second and third row correspond to 3, 4 and 5-fold retrospective subsampling. Subpanels with blue, green and red bounding boxes represent enlarged region of interest in the ground truth and reconstructed images.

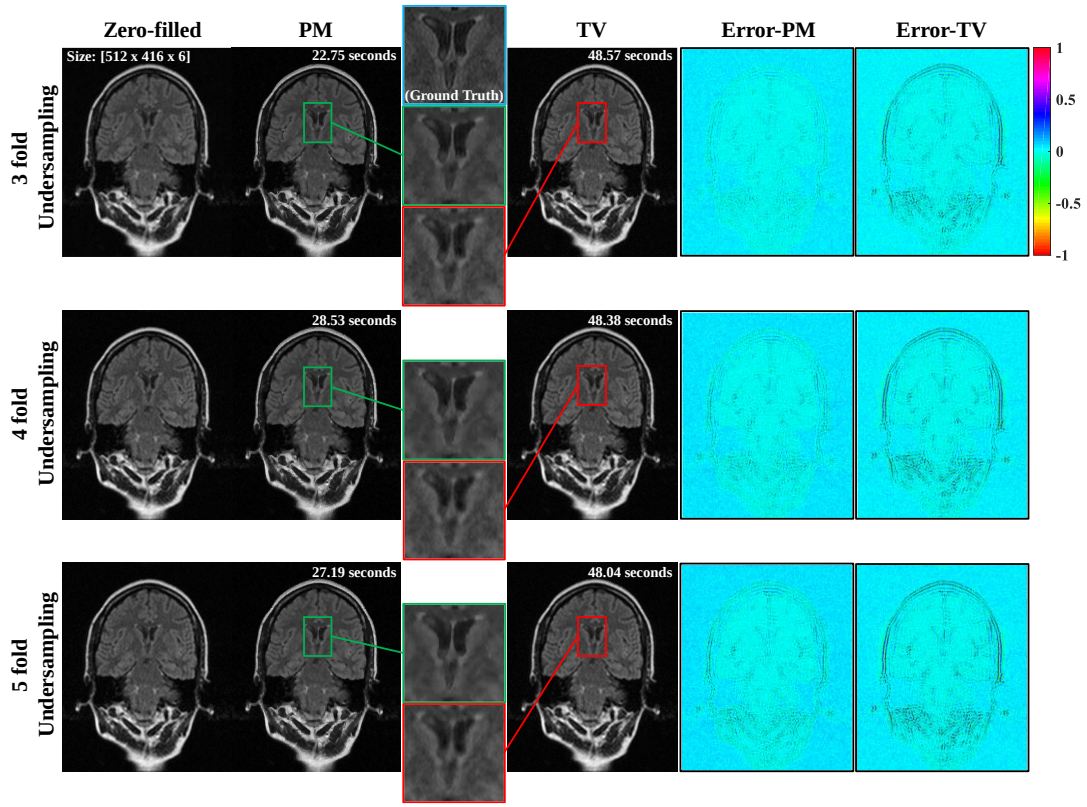

Figure 3.6. Reconstruction using dataset-V for 3, 4 and 5-fold retrospective subsampling using PM diffusion and TV. Column-wise panels show the results of zero-filled reconstruction, PM diffusion based reconstruction, TV reconstruction and the respective error images of PM diffusion and TV. Computation time (excluding step size search) and matrix size are shown in insets. Panels in first, second and third row correspond to 3, 4 and 5-fold retrospective subsampling. Subpanels with blue, green and red bounding boxes represent enlarged region of interest in the ground truth and reconstructed images.

a search procedure. The same step size is then used for reconstructions at acceleration factors of 4 and 5 in spine data, and all three accelerations in head data.

Comparing the structural details present in error images, it is clear that the TV based approach loses more structural details for spine as compared to head data for the same step size. However, when compared with statistically optimized PM diffusion based reconstructions, the error images indicate that the PM diffusion approach preserves more structural details than TV in both datasets, yielding improved quality images. For ease of visual comparison, zoomed regions are shown separately for vertebral bodies in spine data and fornix in head data. With increase in undersampling, TV tends to introduce more smoothing in both datasets as evidenced from the error images and visual inspection of zoomed regions. Whereas PM based diffusion exhibit controlled blur with increased acceleration in both datasets, TV based reconstructions are more artifact-prone in the head dataset.

In spine data, the zoomed regions of TV based reconstruction show blurred vertebral bodies and surrounding regions. While the cervical curvature is clearly seen in both reconstructions, the boundaries of vertebral bodies and spinal cord are not as apparent in TV as in PM diffusion. In the head dataset, TV based reconstruction is seen to introduce high frequency features which are not present in the fully sampled image, for example, at the regions of frontal lobe.

3.4.4 Application to learning based reconstruction

In the context of learning based methods, TV and PM diffusion reconstructions are compared in terms of generating a fast initial approximation of the ground truth image.

In this situation, the sub-optimality of TV based reconstruction is mainly due to the additional computational requirement imposed by the need to search for optimal step size. To illustrate this, a patch based discrete wavelet (PBDW) operator and patch-based nonlocal operator (PANO) are used to learn from the outputs of TV and PM diffusion (97, 115). The step size for TV is searched by solving Eq. [3.2] for different values of γ. Optimum γ is chosen to be that value which minimizes noise in the solution. Time for a search typically depends on the number of iterations used to solve Eq. [3.2].

The reconstruction errors and computation times for dataset-I are listed in Table 3.1. For comparison, reconstruction errors of PANO and PBDW initialized with fully sampled data as reference image are listed in the last column. PM diffusion provides improved image quality and 3 to 4 times faster processing as compared to TV reconstruction due to the inclusion of step size search.

3.5 Discussion

In this work, PM diffusion is introduced as a constrained reconstruction technique applied to multi-channel MR images. This is not a continuous evolution of the noise free image from the initial noisy image. Instead, it is a sequence of single step diffusion processes. At every iteration, the structural information is reinforced by biasing the image before diffusing it further. This can be understood as selecting the solution from a family of denoised images evolved from the initial image (zero-filled reconstruction) by the diffusion process, with frequency components most consistent with the acquired k-space data. The denoising effect is also evident in Fig. 3.7 which compares the cross-

Table 3.1: RLNE measures and computation time for TV and PM diffusion based learned reconstructions.

Size of the data / down sampling rate	Learning method used	PM diffusion MRI					TV MRI					RLNE (Learned from fully sampled ground-truth image)
		PM reconstruction		Learned from the output of PM			TV reconstruction		Learned from the output of TV			
		RLNE	Time (s)	RLNE	Time (s)	Total time (seconds)	RLNE	Time (s)	RLNE	Time (s)	Total time (seconds)	
256x256/ x3	PBDW	0.0706	2.29	0.0599	82.24	84.53	0.0977	42.35	0.0622	82.62	124.97	0.0551
	PANO			0.0595	7.5	9.79			0.0608	7.49	49.84	0.0561
256x256/ x4	PBDW	0.1087	2.3	0.0875	84	86.3	0.1401	43.43	0.0909	82.85	126.28	0.0772
	PANO			0.0856	9.11	11.41			0.0866	9.18	52.61	0.0785
256x256/ x5	PBDW	0.1488	2.23	0.1103	81.96	84.19	0.169	36.89	0.1134	83.26	120.15	0.0953
	PANO			0.1111	10.43	12.66			0.1117	10.72	47.61	0.0992

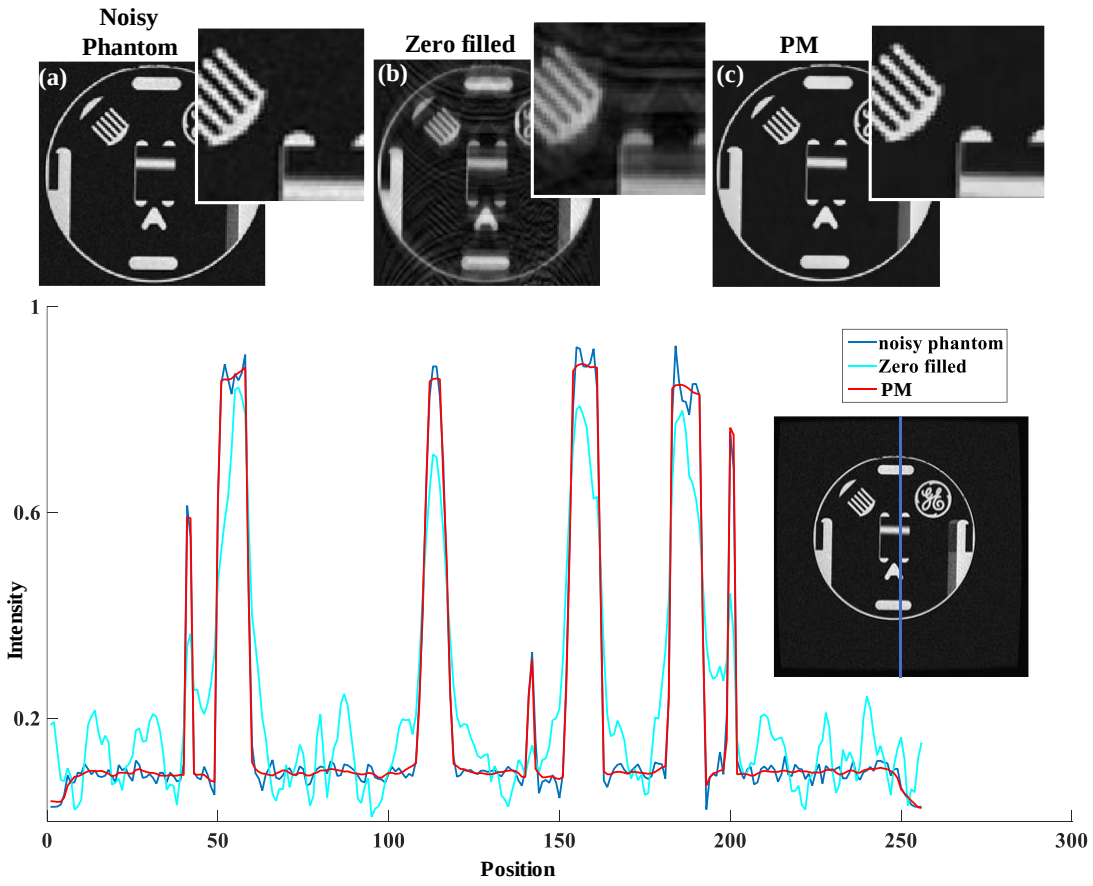

Figure 3.7. Plots comparing cross-sectional intensities in (a) noisy phantom (b) zero-filled reconstruction and (c) PM diffusion based reconstruction. The cross-section is indicated by the blue colored line in the phantom shown in the inset.

sectional intensities of a noisy phantom image (155) with that of zero-filled reconstruction and PM diffusion reconstruction after retrospectively undersampling it by randomly skipping 60% PE lines. The plot shows strong degradation of signal in zero-filled reconstruction while PM diffusion restores and denoises the signal.

Diffusion filter in Eq. [3.5] varies with the choice of diffusivity function. Some of the previously employed diffusivity functions include the ones proposed by Charbonnier et al. (156), Perona and Malik (148), Weickert (42), Andreu at al. (157) and Black et al. (153). In this work, the function proposed by Perona and Malik is used since it gave minimum RLNE and faster convergence compared to others.

The results clearly demonstrate the advantages of PM diffusion over conventional TV. The results in Figs. 3.4-3.5 are actually not very surprising because the step size is a crucial factor for TV denoising. If not properly tuned, it can lead to residual noise or increased blur. For example, the remnant noise of TV reconstruction in Fig. 3.5 could make it difficult to diagnose the white matter lesions in the regions surrounding ventricles. PM diffusion minimizes dependence on step size by adapting the contrast parameter to the changes in data. However, at very high accelerations, the chance of recovering some fine features may be limited with either method.

3.5.1 Computational constraint

The need to search the step size every time is time consuming and is counterproductive in the present trend of learning-based CS frameworks where redundant systems for sparsifying MR images are trained from an initial approximation of the image (96, 97, 114, 115, 118, 158). Since in many practical scenarios, the ground truth image is not

available, an approximation using fast reconstruction is desired. The statistical optimization of the contrast parameter does this job for PM diffusion by eliminating the need for a search, and thereby rendering itself as a better choice over the conventional TV approach.

3.6 Conclusion

In this chapter, NL diffusion is presented as an alternative to TV regularization because of its advantage over TV when only a rough estimate of the regularization parameter is available. The estimation of the contrast parameter from the combined channel information removes the need for a parameter search and hence result in faster reconstruction.

Chapter 4

Mixed-order Diffusion Reconstruction

4.1 Introduction

In the previous chapter, an NL diffusion penalty (148, 149) using PM diffusivity function is introduced as an alternative to TV (37, 159) in MR image reconstruction application (41, 160). While these edge preserving penalty functions encourage recovery of images with sparse gradients, the assumption of piecewise constant regions in the image often lead to staircase artifacts in reconstructed images giving it a patchy appearance (38, 40, 42, 161). Even though the use of data consistency correction in the context of CS reconstruction model limits these artifacts to a certain extent, blocky effect can become prominent as the degree of sampling reduces.

Similar to the higher order solutions for avoiding staircase artifacts in TV (38, 40), use of fourth-order Partial Differential Equations (PDEs) is known to control the blocky effects in the denoising applications of NL diffusion (161-163). However, it also tends to introduce speckle effects in the solution (161). Since the functional using combined first and second degree derivatives of the image are reported to give better edge preservation properties (164, 165), researchers have previously attempted to

combine second (uses first degree derivative) and fourth (uses second degree derivative) order diffusion solutions by weighted averaging (43) to nullify both staircase and speckle effects.

This approach however, attempts to remove staircase/speckle after it has formed in the solution using an arbitrary choice of global weight for the solutions of second and fourth-order diffusion. This implicitly assumes similar strength of intensity modulation due to speckle/staircase in all regions of the image which is likely to be violated in most practical scenarios. Though such an approach can be made effective with the use of spatially varying weights, it is again limited by the accuracy in estimation of the staircase/speckle effects. Therefore, in this chapter, a mixed-order diffusion reconstruction is introduced which aims at preventing the formation of staircase/speckle during the reconstruction process rather than trying to remove it from the solution.

It is shown that the proposed method produces both quantitatively and qualitatively improved results compared to TV, conventional second-order diffusion and fourth-order diffusion. Remaining part of this chapter is organized into four sections. In the first section, a brief overview of the second order NL Diffusion Reconstruction (NLDR) model, theory of mixed-order NL diffusion (NLDR$^{\mathbf{M}}$) strategy and its application to dictionary learning (DL) approaches is described. Next section describes the implementation of NLDR$^{\mathbf{M}}$. The final section includes illustrations of NLDR$^{\mathbf{M}}$ applied to in vivo data and comparison with state-of-the-art solutions for TV. The chapter concludes with a detailed discussion of its implications

and relative advantages. It may be noted that wherever the reconstruction is denoted as NLDR, it is assumed that a PM diffusivity function is used.

4.2 Theory

4.2.1 Second-order NLDR model

Second-order NL diffusion based edge preserving reconstruction explained in the previous chapter removes the undersampling artifacts from zero-filled reconstructed image to generate an estimated image by diffusing the image (U) as

$$U_{diffused}^{O2} = U + \gamma div(g(|\nabla U|)\nabla U) + c\mathcal{F}_u'(K_u - \mathcal{F}_u U), \qquad [4.1]$$

where K_u denotes the acquired k-space samples, g is the diffusivity function, γ is a regularization parameter which controls diffusion strength and c is the bias relaxation factor. Second term in Eq. [4.1] imposes explicit penalty for edges and third term constraints diffusion to ensure that the solution does not deviate from K_u. Using the PM diffusivity function (148) in Eq. [3.6], we have the contrast parameter α that separates the gradient magnitudes of edges and noise (artifacts) in image so that diffusion of region that generates gradient magnitudes below α is encouraged.

4.2.2 Blocky effect

Edge preserving denoising techniques are generally designed to diffuse smooth areas in an image faster than less smooth ones (42). Consequently, these denoising techniques like TV and PM diffusion can generate staircasing artifacts and result in a blocky effect. Eventhough the biased form of NL diffusion used in the present context

can limit the formation of these artifacts by bias correction, influence of bias reduces as the undersampling factor increases.

Since staircase effects are manifested as artificial edges, setting the value of contrast parameter in NLDR^2 to be higher than the gradient magnitudes of staircase edges will serve to suppress these effects. This however addresses the problem by removing all the edges that have similar gradient magnitudes as those of the artificial steps. This is not the best solution due to the loss of true edges whose gradient strengths fall below α.

4.2.3 Combined second and fourth-order diffusions

Fourth-order PDEs are known to be an effective tool to counteract the blocky effect in NL diffusion denoised images (161, 162). This class of PDEs optimize the trade-off between noise removal and edge preservation by minimizing an increasing function of the absolute value of the Laplacian of image intensity. The edge cost thus defined diffuses U over a small time ∂t by (161)

$$\partial_t U = \nabla^2(g(|\nabla^2 U|)\nabla^2 U). \qquad [4.2]$$

In the context of numerical implementation, ∂t represents time between two successive diffusion iterations. From Eqs. [4.1-4.2], the resulting numerical solution of regularized diffusion is given by

$$U_{diffused}^{mix} = U_{diffused}^{O2} + \lambda\nabla^2(g(|\nabla^2 U|)\nabla^2 U)\,, \qquad [4.3]$$

where λ is a regularization parameter that controls the strength of fourth-order diffusion. The second term in the right-hand side of Eq. [4.3] acts as a regularizer

which restricts formation of staircase artifacts in the planar regions, resulting in a more natural looking image.

4.2.4 Application to dictionary learning methods

DL based methods work by learning a basis that can approximate the image sparsely devoid of the noise-like properties (88, 96). Since the random sampling used in CS provides sufficient aliasing incoherence (6), undersampling artifacts appear more noise-like and hence DL methods are effective (88). Since the ground truth image is not available as reference, DL based MRI (DLMRI) generally learns the sparse operator from either the zero-filled reconstructed image or an approximation of the ground truth image obtained using conventional CS-MRI reconstruction techniques (166, 167).

Better approximation of the reference image can not only improve the image quality but also result in faster convergence. In the context of these learning based methods, main role of NLDR is to generate a fast approximation of the image that can be used to learn the sparsifying operator (160). Learning the basis from NLDR filtered data can be considered as sparsifying the data in both finite difference domain and the learned basis. This ensures better reproducibility of structural details by enforcing additional penalty for edges. Although the staircase edges due to first order derivatives in TV or NLDR$^{\mathbf{2}}$ will not be apparent in such cases due to the smooth approximation of image by the learned basis, they can implicitly affect the quality of training data. Hence, use of NLDR$^{\mathbf{M}}$ can serve the purpose better.

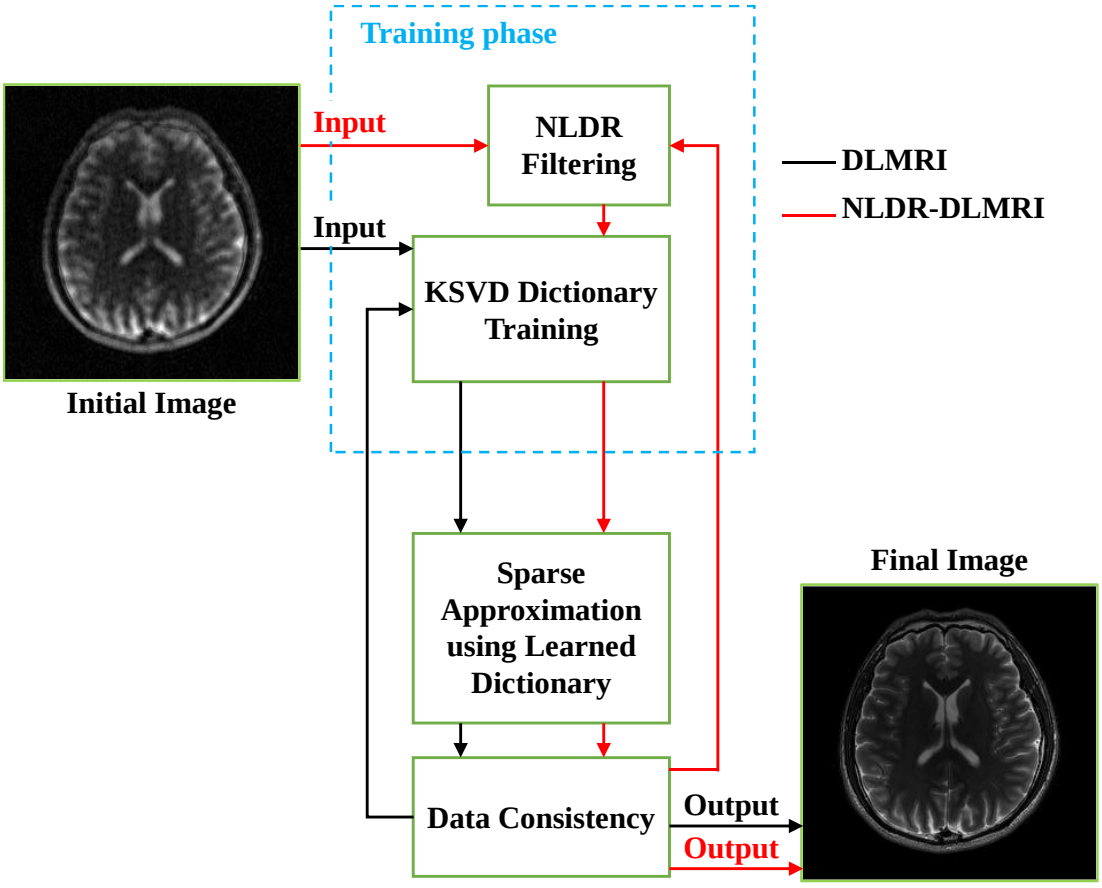

Figure 4.1. Workflow of DLMRI and NLDR-DLMRI. Black and red arrows indicate the process flow of DLMRI and NLDR-DLMRI respectively.

The algorithmic workflow of NLDR based DLMRI is summarized in Fig. 4.1. Black and red colored arrows indicate the process flow of DLMRI (96) and NLDR-DLMRI respectively. The main difference in the latter from the former is the addition of NLDR filtering in the training phase. In the proposed method, the standard K-SVD algorithm (100) learns an overcomplete sparsity basis from the output of $NLDR^{M}$ which is used to sparsify the image. The data consistency step biases the reconstruction process by enforcing fidelity with the acquired k-space samples K.

4.3 Methods

4.3.1 Implementation

An algorithmic framework similar to that of $NLDR^{\mathbf{2}}$ in the previous chapter is used to implement $NLDR^{\mathbf{M}}$. Main difference is the fourth-order term in the diffusion update step. The resultant reconstruction framework is given in algorithm 4.1. For comparison, the implementations of DLMRI, second-order total generalized variation (TGV) (40) and higher degree TV (HDTV) (38, 93) shared by the authors in (25, 166-169) are used. Error in reconstruction is computed using RLNE.

The implementation of DLMRI available in (167) with its default choice of parameters is also used to implement the proposed NLDR-DLMRI reconstruction model. 10 iterations of NLDR filtering in the training step are used in all the reconstructions performed in this study. The corresponding pseudo-code of NLDR-DLMRI is given in Algorithm 4.2. NLDR filtering step processes the image according to the Algorithm 4.1.

Algorithm 4.1: NLDR^{M}

0: $k = 1;\ U^{(0)} = \mathcal{F}_u' K;\ t^{(1)} = 1;$

1: $while\ (k < k_{max})$

2: $\widehat{U}^{(k)} = U^{(k-1)} + c\ \mathcal{F}_u'\left(K_u - \mathcal{F}_u U^{(k-1)}\right);$

3: $\widetilde{U}^{(k)} = \widehat{U}^{(k)} + \gamma div\left(g\left(\nabla\widehat{U}^{(k)}, \alpha_1\right)\nabla\widehat{U}^{(k)}\right) + \lambda div\left(g\left(\nabla^2\widehat{U}^{(k)}, \alpha_2\right)\nabla^2\widehat{U}^{(k)}\right);$

4: $t^{(k+1)} = \left(1 + \sqrt{1 + 4(t^{(k)})^2}\right)/2;$

5: $U^{(k)} = \widetilde{U}^{(k)} + \left(t^{(k)} - 1\right)\left(\widetilde{U}^{(k)} - \widetilde{U}^{(k-1)}\right)/t^{(k+1)};$

6: $k = k + 1;$

7: end

4.3.2 Choice of reconstruction parameters

Parameters that control the reconstruction performance of NLDR$^{\mathbf{M}}$ include (i) relaxation parameter c, (ii) second and fourth order contrast parameters α_1 and α_2, and (iii) second and fourth order diffusion strengths γ and λ. Both c and diffusion strength parameters (step size) are common to both NL diffusion and TV. Similar to NLDR$^{\mathbf{2}}$, role of c in NLDR$^{\mathbf{M}}$ is also to minimize the effect of acquisition noise in the reconstructed image. Relaxation of c in both TV and NL diffusion is desired when the acquired data are noisy. Because there are no known methods to a priori fix the best possible value of c in such cases, the best choice is to monitor the final reconstructions corresponding to different values of c.

Algorithm 4.2: Pesudo-code of NLDR-DLMRI

Input : zero-filled image

Output : Reconstructed MR image

Iteration:

1. NLDR filtering
2. Learn dictionary using KSVD
3. Sparse approximation of the individual patches of image
4. Form image from patches by averaging pixel values that appear in multiple patches
5. Restore acquired frequency samples in the k-space after Fourier transformation
6. Inverse Fourier transform to compute the image from k-space

In the case of NL diffusion, adaptation of contrast parameter helps to minimize the inherent noise in image as shown in the previous chapter. Therefore, c is set to 1 and α_1 and α_2 are updated in each iteration using the mean absolute deviation (MAD) of 1st and 2nd order gradients (∇U and $\nabla^2 U$) as

$$MAD(\nabla U) = mean(|\nabla U - mean(\nabla U)|) \quad [4.4]$$

and

$$MAD(\nabla^2 U) = mean(|\nabla^2 U - mean(\nabla^2 U)|) \quad [4.5]$$

Alternatively, one can use approaches like the noise estimator described by Canny (141, 160) to estimate contrast parameter.

The previous chapter also shows that an improved image quality can be achieved using small values of contrast parameter by compromising the convergence rate when the inherent noise is low. Since the role of contrast parameter in NLDR$^{\mathbf{M}}$ is same as that of NLDR$^{\mathbf{2}}$, this effect of contrast parameter holds true for mixed order reconstruction as well. If one has a prior knowledge that the inherent noise in acquisition is low, it is a good idea to set the contrast parameter less than 50% of MAD and 100% MAD for high noise levels. A good compromise of speed and quality is achieved when the contrast parameter is set as 50% MAD.

Diffusion strength controls the extent of diffusion in a single iteration. As pointed out in the previous chapter, diffusion strength parameter can be determined by solving the cost function for different values of γ and λ and selecting the value that minimizes the cost (6). Alternatively, L-curve theory (170) is a widely used approach for this purpose. Since NL diffusion based reconstruction is known to be less sensitive to the step size (148, 149), an experimental approach (161) is used in this work to determine γ and λ. In this approach, sensitivity of NLDR$^{\mathbf{M}}$ to γ and λ is investigated by reconstructing a Shepp-Logan phantom with added complex Gaussian noise to k-space for different choices of γ and λ (171). It is seen that the reconstruction is stable for all values of $0 < \gamma < 0.1$ and $0 < \lambda < 0.01$ (shown in Fig. 4.2).

4.4 Results

Results are demonstrated using publicly available datasets which were previously used to demonstrate the performance of CS reconstruction in MRI. These include cardiac cine dataset publicly available in (167), head scan of 3 subjects and abdominal scan of 28 subjects. In addition, the proposed methods are also tested on four-channel spine and six-channel brain data (shown in the previous chapter) acquired using Siemens 1.5T Magnetom-Avanto clinical MR scanner at Sree Chitra Tirunal Institute of Medical Sciences and Technology, Trivandrum, India.

All implementations are performed using Matlab (The MathWorks, Inc., Natick, MA, USA) on a PC with an Intel Xeon E5-2609 2.4 GHz processor and 16 GB of RAM running Windows 7 operating system.

4.4.1 Sensitivity to regularization

The sensitivity of NLDR$^{\mathbf{M}}$ to γ and λ is investigated by reconstructing a Shepp-Logan phantom with added complex Gaussian noise for different choices of γ and λ. Fig. 4.2(a)-(b) plots the maximum value of λ that minimizes the steady state RLNE of NLDR$^{\mathbf{M}}$ against different choices of γ for pseudo-random and pseudo-radial sampling patterns, respectively. Lines of different color represent different noise levels. It is seen that the reconstruction is stable for all values of $0 < \gamma < 0.1$ and $0 < \lambda < 0.01$. Panels (c) and (d) depict plot of RLNE versus λ for a particular choice of γ in (a) and (b). Adhering to the above range for γ and λ, the values for γ and λ are set as 0.1 and 0.01 for all numerical experiments conducted in this study.

4.4.2 Reconstruction of in vivo datasets

In Fig. 4.3, NLDR$^{\mathbf{2}}$, fourth-order NLDR (NLDR$^{\mathbf{4}}$) and NLDR$^{\mathbf{M}}$ reconstruction performance at different undersmapling levels are compared. Column-wise panels correspond to two different datasets and row-wise panels correspond to Poisson-disk and pseudo-radial sampling patterns (shown in insets of Fig. 4.2). Each panel show both RLNE and convergence time as functions of undersampling level. Blue and orange lines depict RLNE and computation time, respectively. The datasets used are T2-weighted brain images of size 256 x 256 acquired from a healthy volunteer at a 3T Siemens Trio Tim MRI scanner with 32 coils using the T2-weighted turbo spin echo sequence (TR/TE=6100/99 ms, FOV = 220 x 220 mm^2, slice thickness = 3 mm) publicly available in (33).

In all cases, one can see that RLNE of NLDR$^{\mathbf{2}}$ is lower than NLDR$^{\mathbf{4}}$ and higher when compared to NLDR$^{\mathbf{M}}$. Reduced RLNE of proposed method with increasing undersampling rates is attributable to the accompanying staircase effects. On the flipside, plots show that computation times for NLDR$^{\mathbf{M}}$ are higher as compared to those for NLDR$^{\mathbf{2}}$.

4.4.3 DL based reconstruction

When used as an auxiliary constraint in DL, the smooth approximation of image by the learned basis can remove any possible staircase effect due to NLDR$^{\mathbf{2}}$. Hence, the improvement with the use of NLDR$^{\mathbf{M}}$ will rather reflect in the quality measures and computation time. Therefore, PSNR values of DLMRI reconstruction with and without

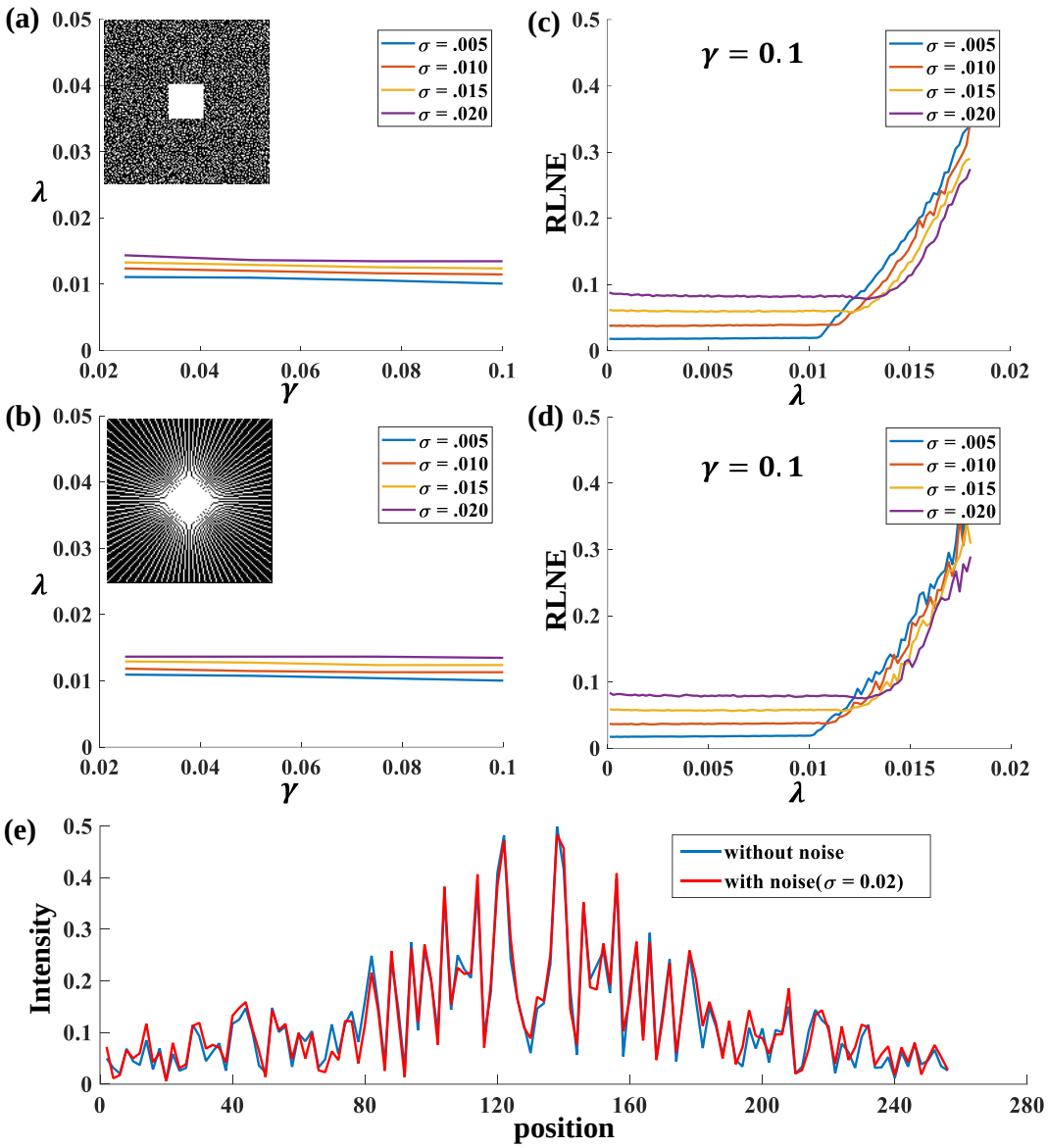

Figure 4.2. (a)-(b) Maximum value of λ that minimizes the steady state RLNE of mixed order NLDR plotted against different choices of γ for pseudo-random and pseudo-radial sampling patterns, respectively. Lines of different color represent different noise levels. Respective sampling patterns used are shown in insets. (c)-(d) RLNE versus λ plotted for a particular choice of γ in (a) and (b). σ indicate the standard deviation of noise added to data. (e) A representative comparison of cross-sectional intensities in k-space with and without added noise.

NLDR$^{\mathbf{M}}$ filtering in the training phase at 3, 4 and 5 fold undersampling levels are plotted against iterations in Fig. 4.4.

Panels (a) and (b) correspond to two different datasets. Top panels show the ground truth images and the pseudo-radial sampling masks used for 5-fold undersampling. While the gain in PSNR is less than 2dB for NLDR based DLMRI, it can be seen that the PSNR saturates almost twice as fast as traditional DLMRI approach when the dictionaries are learned from the NLDR filtered data. For a detailed comparison, RLNE, PSNR and computation times for three head datasets are listed in Table 4.1.

For dynamic imaging, the state-of-the art method of DLTG (88) extends DL method to the temporal dimension and imposes additional sparsity constraint along this dimension by minimizing the l_1-norm of the temporal gradient (TG). Results shown in Fig. 4.5 compares the use of NLDR$^{\mathrm{M}}$ filtering as an alternative to TG in DL based dynamic MR image reconstruction. This is denoted as DLTG-NLDR$^{\mathrm{M}}$.

Acquisition details of the fully sampled short-axis cardiac cine dataset (167) used in this study can be obtained from (88). It contains 30 temporal frames of size 256 x 256 with a 320 x 320 mm field of view and 10 mm slice thickness, generated using an optimal combination of 32-channel data. A magnitude temporal frame and the corresponding sampling pattern for 4 fold undersampling are illustrated in panel (a). While PE dimension is undersampled, both FE and temporal dimensions are fully sampled. Temporal profiles along two lines (1 and 2) are used for comparison. ROI is indicated using yellow bounding box. Panel (b) plots PSNR as a function of iteration for TG, NLDR^{2} and NLDR$^{\mathrm{M}}$ based DLTG reconstruction.

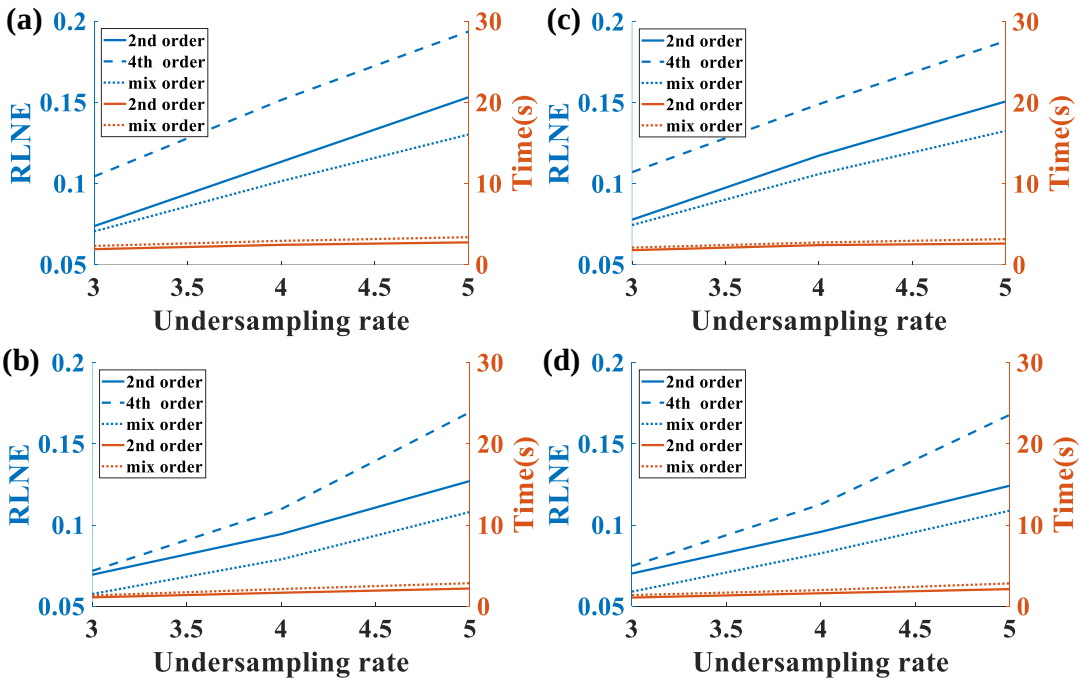

Figure 4.3. Reconstruction errors (RLNE) and convergence time of NLDR$^{\mathbf{2}}$, NLDR$^{\mathbf{4}}$ and NLDR$^{\mathbf{M}}$ at different undersmapling levels are plotted as a function of iterations. Blue and orange lines depict RLNE and computation time, respectively.

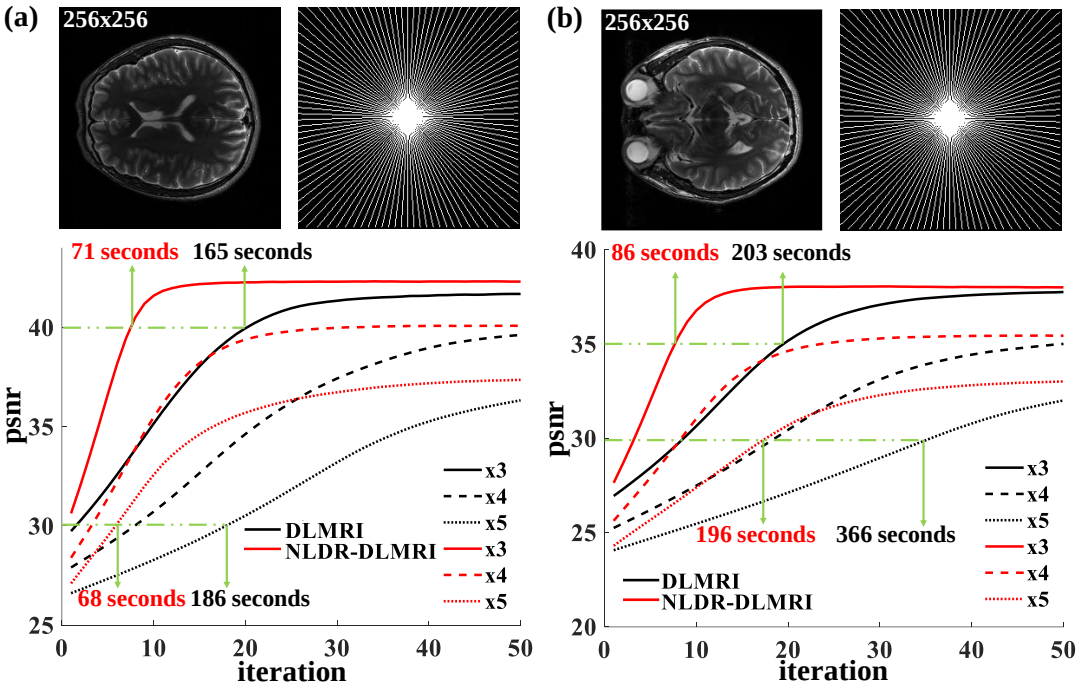

Figure 4.4. (a)-(b) PSNR values of DLMRI reconstruction of two different datasets plotted as function of iteration number. In each, the red and black curves correspond to DLMRI reconstruction with and without mixed-order NLDR. Different line styles represent 3, 4 and 5-fold undersampling as indicated in the legends. Top panels show the ground truth images and the pseudo-radial sampling masks used for 5-fold undersampling.

Table 4.1: Quality Measures and Computation Time for Conventional DLMRI and NLDR Based DLMRI.

Dataset (size)	**DLMRI**			**NLDR^{2}-DLMRI**			**NLDR^{M}-DLMRI**		
	RLNE	**PSNR**	***Time*(s)**	**RLNE**	**PSNR**	***Time*(s)**	**RLNE**	**PSNR**	***Time*(s)**
				Undersampling x3					
Head1 (256x256)	0.0578	41.68	*202*	0.0527	42.06	*135*	**0.0518**	**42.42**	***104***
Head 2 (256x256)	0.0589	40.74	*200*	0.0551	41.11	*118*	**0.0543**	**41.38**	***96***
Head 3 (256x256)	0.0600	37.76	*362*	0.0587	37.82	200	**0.0574**	**38.01**	***169***
				Undersampling x4					
Head 1 (256x256)	0.0688	39.69	*376*	0.0684	40.01	*244*	**0.0673**	**40.19**	***208***
Head 2 (256x256)	0.0790	38.40	*309*	0.0769	38.93	*204*	**0.0740**	**39.13**	***184***
Head 3 (256x256)	0.0811	35.01	*447*	0.0801	35.35	296	**0.0784**	**35.45**	***265***
				Undersampling x5					
Head 1 (256x256)	0.1014	36.32	*411*	0.0982	37.28	*320*	**0.0960**	**37.42**	***295***
Head 2 (256x256)	0.1082	35.08	*406*	0.1050	36.15	*301*	**0.1040**	**36.27**	***273***
Head 3 (256x256)	0.1146	32.01	*473*	0.1058	32.89	*400*	**0.1048**	**33.02**	***369***

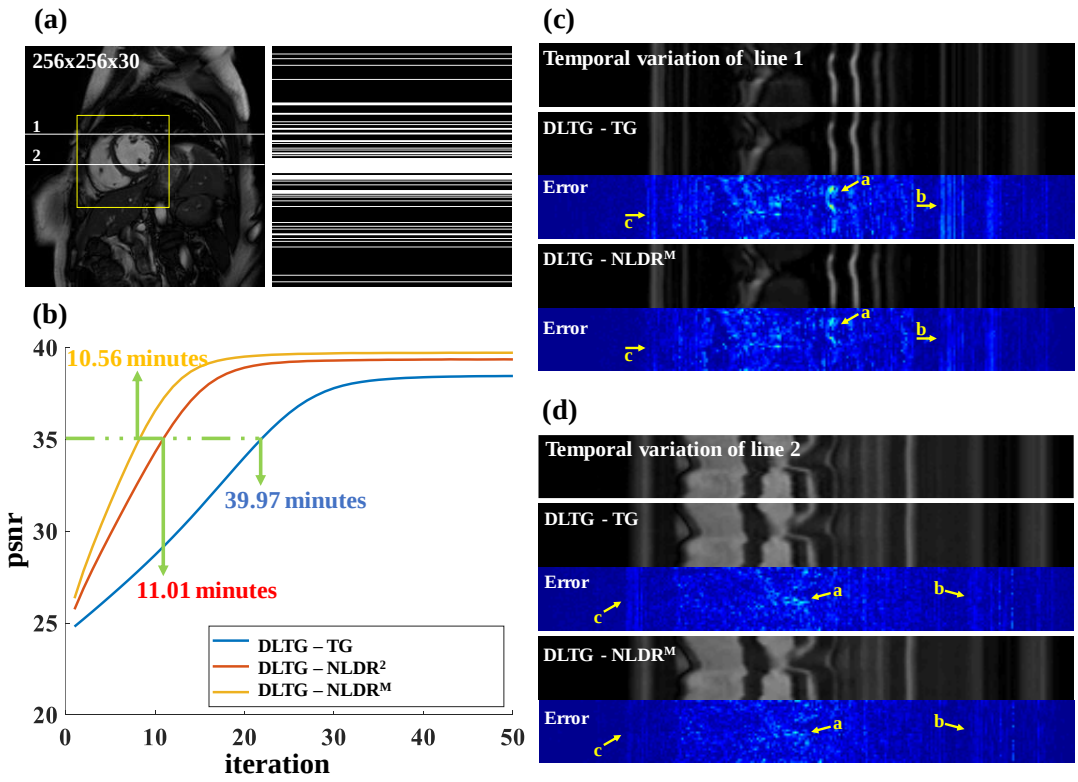

Figure 4.5. (a) A magnitude temporal frame of the dynamic MRI dataset and the corresponding sampling pattern for 4 fold undersampling. Temporal profiles along two lines (1 and 2) are used for comparison. ROI is indicated using yellow bounding box. (b) PSNR plotted as a function of iteration. Green arrows indicate the computation time for TG and NLDR based DLTG reconstruction to attain PSNR value of 35dB. (c)-(d) Ground truth and reconstructed temporal profiles of lines 1 and 2 using TG and NLDR^{M} based reconstructions and their corresponding error images amplified by 6.

Similar to the results in Table 4.1, it is observed that both PSNR and computation time improves with the application of NLDR^{M}. Panels (c)-(d) compares the ground truth and reconstructed temporal profiles of lines 1 and 2 using TG and NLDR^{M} based DLTG. Corresponding error images (amplified by 6) are shown for comparison. Yellow arrows a-c indicates the regions both inside and outside the ROI where NLDR^{M} based DLTG approximates the temporal profiles better than TG. It may be noted that these local regions of improved error measures correspond to edges in the image. This can be attributed to the improved reproduction of structural details by NLDR^{M}.

4.4.4 Comparison with state-of-the-art methods for TV

In this section, image quality of the proposed method is compared with state-of-the-art solutions for blocky effect in TV based reconstructions (38, 40, 93). The head dataset shown in the top left panel of Fig. 4.6 is retrospectively undersampled using Poisson-disk sampling pattern. Remaining panels compare the ROI of reconstructed image at 4 and 5 fold undersampling levels. The respective undersampling level and reconstruction technique used are shown in insets. The amplified absolute difference from ground truth is illustrated on the right side in each panel. White colored circles in the difference image highlights the regions that NLDR$^{\mathbf{M}}$ approximates better. Yellow and red arrows point out the regions affected by speckles and blocky effects in NLDR$^{\mathbf{4}}$ and NLDR$^{\mathbf{2}}$ respectively.

In all cases, it is observed that NLDR$^{\mathbf{M}}$ approximates ventricular margins, cortical grey white interface and sulcal margins better compared to others. It may be noted that the blocky effect is more pronounced in the magnitude image of 5 fold undersampling, indicating that NLDR$^{\mathbf{M}}$ is more useful when the data consistency correction is less

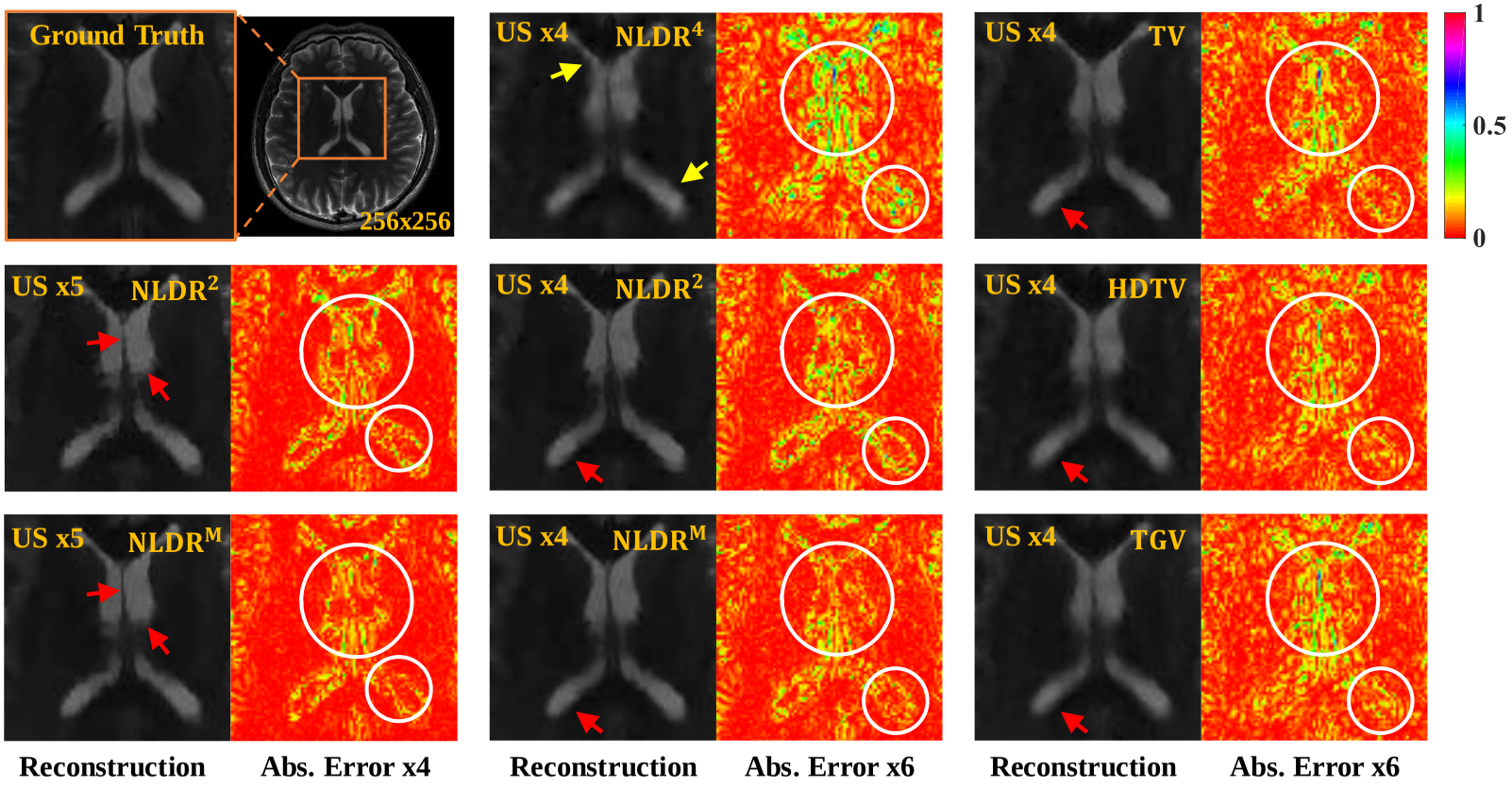

Figure 4.6. Comparison of the ROI of reconstructed head dataset at 4 and 5 fold undersampling levels. Ground truth image is shown in the top left panel. The respective undersampling level and reconstruction technique used are shown in the inset. The absolute difference from ground truth amplified 6 times for 4 fold undersampling and 4 times for 5 fold undersampling is illustrated on the right side in each panel. White colored circles in the difference image marks the regions in the image that NLDR$^{\mathbf{M}}$ approximates better. Yellow and red arrows point out the region affected by speckles and blocky effects in the results of NLDR^{4} and NLDR^{2}.

Table 4.2: RLNE Measures and Computation Time for NLDR and TV Based Reconstructions.

Dataset (size)	**TV**		**NLDR^2**		**NLDR^4**		**NLDR^M**		**HDTV**		**TGV**	
	RLNE	***Time*(s)**	**RLNE**	***Time*(s)**	**RLNE**	***Time*(s)**	**RLNE**	***Time*(s)**	**RLNE**	***Time*(s)**	**RLNE**	***Time*(s)**
Undersampling x3												
Head 1 (256x256)	0.0975	*50.0529*	0.0704	***2.6867***	0.0973	*3.4026*	**0.0669**	*3.7394*	0.082	*17.4401*	0.0918	*50.5134*
Head 2 (256x256)	0.1011	*43.6568*	0.0737	***2.6218***	0.1043	*3.3653*	**0.0704**	*3.8452*	0.0877	*17.1311*	0.1006	*49.0326*
Head 3 (256x256)	0.1014	*43.4695*	0.0777	***2.6184***	0.1065	*3.3575*	**0.0744**	*3.8475*	0.1012	*17.6789*	0.1010	*49.1904*
Spine (450×448×4)	0.098	*410.373*	0.0848	***29.5865***	0.0880	*45.1270*	**0.0812**	*52.6565*	0.0976	*310.32*	0.0972	*307.722*
Head 4 (512×416×6)	0.1036	*436.196*	0.0903	***45.2465***	0.0939	*66.8859*	**0.0875**	*71.341*	0.0947	*483.1*	0.1004	*401.373*
Undersampling x4												
Head 1 (256x256)	0.1378	*49.5836*	0.1081	***3.0224***	0.1403	*3.4540*	**0.0962**	*3.8237*	0.122	*17.0361*	0.1372	*49.4847*
Head 2 (256x256)	0.1426	*43.6482*	0.1134	***2.6099***	0.1514	*3.3186*	**0.1014**	*3.9374*	0.1328	*17.3044*	0.1345	*49.2047*
Head 3 (256x256)	0.1355	*43.4262*	0.1173	***2.5893***	0.1490	*3.3023*	**0.1059**	*3.8333*	0.1269	*17.082*	0.1343	*49.1096*
Spine (450×448×4)	0.1005	*410.337*	0.0992	***29.6115***	0.1037	*43.4657*	**0.0944**	*51.2523*	0.1001	*309.069*	0.0979	*308.733*
Head 4 (512×416×6)	0.1113	*435.96*	0.106	***44.0742***	0.1099	*67.3991*	**0.1022**	*75.1422*	0.1093	*481.387*	0.1064	*396.915*

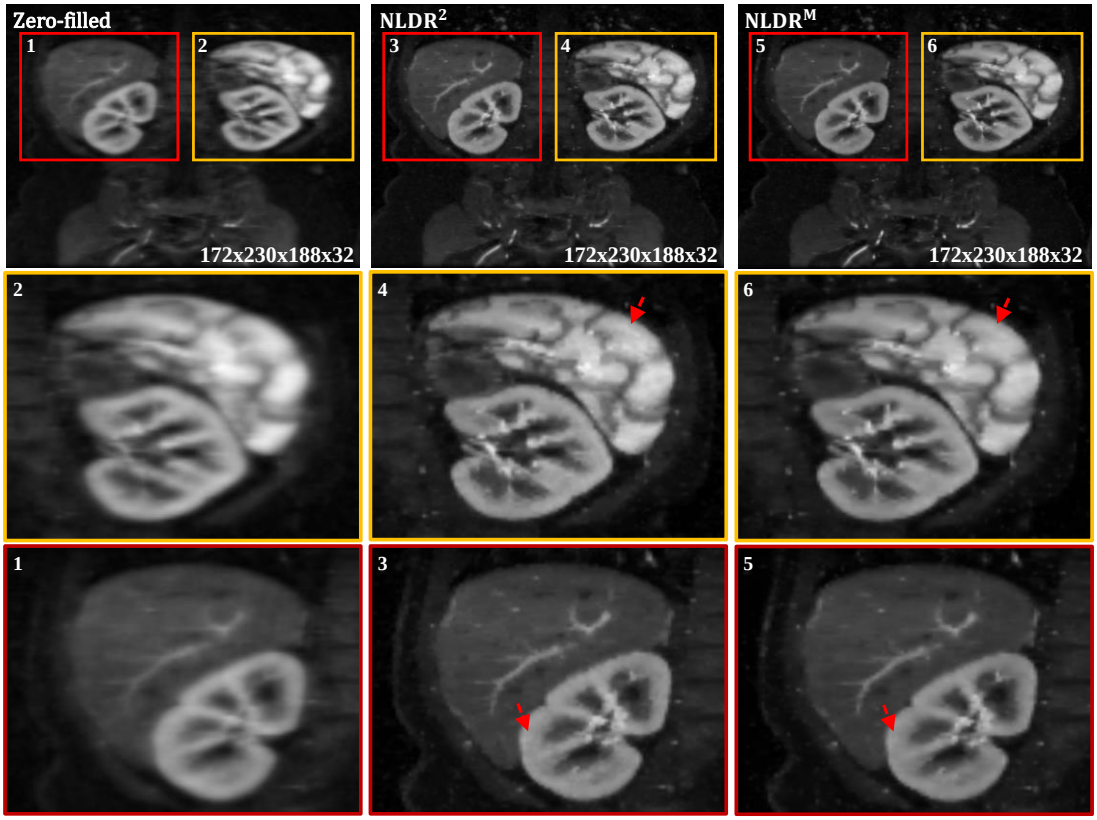

Figure 4.7. Reconstructions of abdominal data prospectively undersampled (using the 3D sampling pattern shown in Fig. 4.8) and compared across two different ROIs shown in red and orange bounding boxes. Column-wise panels depict zero-filled (Left column), NLDR^{2} (Middle column) and NLDR$^{\mathbf{M}}$ (Right column) reconstructions.

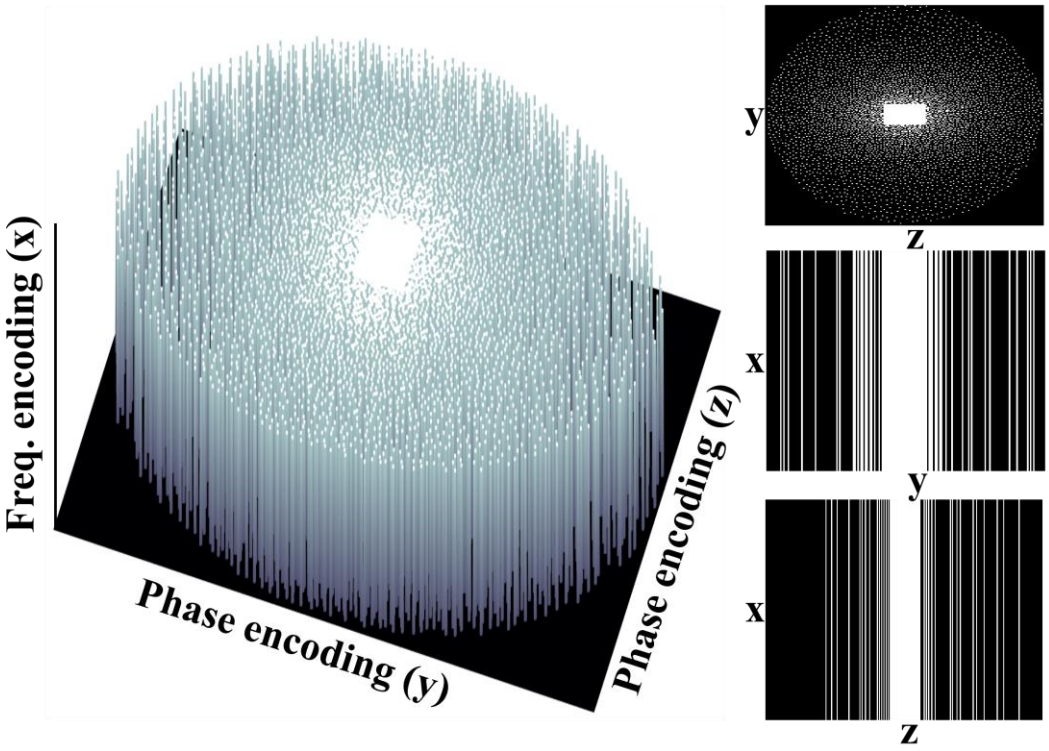

Figure 4.8. 3D sampling pattern for acquisition with 11% acquired samples. Frequency encoding dimension (x) is fully sampled and both phase encoding dimensions (y and z) are randomly undersampled. The sticks represent sampled locations of k-space. Panels on the right side show the resultant undersampling along y-z, x-y and x-z planes where white coloured pixels represent the sampled locations.

effective. Though HDTV and TGV show no apparent blocky effects, it tends to smooth out the boundaries, as evident in the error images. The reconstruction errors and computation time for five different datasets are listed in Table 4.2.

In the case of 24% undersampling, there is some extent of resolution loss and artifacts for all types of reconstruction considered in this study. Achievable acceleration factor in the CS reconstruction models mainly depend on the sparsity of the image in the domain in which it is assumed to be sparse (15, 88) and the incoherence of the aliasing interference caused by sampling pattern (6). Although fine details are lost with all the methods compared, a more satisfactory reconstruction is obtained using NLDR$^{\mathbf{M}}$.

The 2D Poisson-disk sampling pattern simulates the plane formed by two undersampled phase-encoding dimensions of a typical 3D acquisition. As a proof of concept, NLDR^{2} and NLDR^{M} reconstruction of prospectively undersampled multi-channel 3D abdomen data publicly available in (172) are shown in Fig. 4.7. This dataset was acquired on a GE clinical 3T scanner with 32 coils (FOV = 260 x 208 mm^2, slice thickness = 1 mm). Each coil data is of size 192 x 256 x 184. More details about the dataset are available in (172). 11% samples are collected using the sampling pattern shown in Fig. 4.8. Frequency-encoding dimension (x) is fully sampled and both phase-encoding dimensions (y and z) are randomly undersampled. Thick lines in the 3D representation of the sampling pattern correspond to sampled locations of k-space. The resultant undersampling along y-z, x-y and x-z planes are shown in the panels on the right in which white colored pixels represent the sampled locations.

Square root of sum-of-square (SSOS) images was used to combine individual coil images (61). Column-wise panels in Fig. 4.7 depict zero-filled, NLDR^{2} and NLDR^{M} reconstructions. Panels in second and third rows correspond to the enlarged ROIs shown in red and orange bounding boxes. Since the data was prospectively undersampled, reconstructions were subjectively evaluated by expert radiologists and graded using a 5-point score of image quality listed in Table 4.3.

The scores 1-5 is based on the following criteria:

1 - worst image quality (no findings detectable).

2 - poor image quality (findings can be detected but the margin or internal characteristics are difficult to evaluate).

3 - fair image quality (partially indistinct findings can be detected and the margin or internal characteristics can be evaluated).

4 - good image quality (some indistinct findings can be detected and the margin or internal characteristics can be evaluated).

5 - excellent image quality (findings are extremely clear and easy to detect and the margin or internal characteristics can be evaluated)

The scores suggest that both reconstructions produce similar diagnostic qualities in the regions of fat planes while NLDR$^{\mathbf{M}}$ produced comparatively better reconstructions in visceral capsular interface, solid organ internal architecture, vascular margins and lesion visualization. This indicate that the mixed-order reconstruction technique would be particularly beneficial for images with fine structural details like angiographic images at high undersampling rate where the chances of blocky effect are high.

Table 4.3: Blind radiologist scoring of abdominal data reconstruction in Fig. 4.7, showing average scores of listed features by five expert radiologists.

Sl. No.	Features	Blind Average Score (out of 5)		Remarks
		Reconstruction 1 ($NLDR^M$)	Reconstruction 2 ($NLDR^2$)	
1.	Visceral capsular interface	4	3.5	Reconstruction 1 is closest to diagnostic quality
2.	Vascular margins	3	2.5	
3.	Solid organ internal architecture	3	2.5	
4.	Lesion visualization	3	2.5	
5.	Fat planes	3	3	

4.5 Discussion

4.5.1 Working principle and relative advantages

In this work, a fourth-order regularization is introduced as a preventive measure for blocky effect (staircase artifacts) in NL diffusion based MR image reconstruction. Basic idea is to allow the reconstruction model to include a planar image as a possible solution using fourth-order diffusion terms. In the absence of proposed regularization, if a staircase forms in the initial diffusion iterations in a region of the image where intensity varies smoothly, the diffusion process tends to keep it in the final solution

when the bias correction is weak. In the presence of fourth-order terms in the reconstruction model, however, the smoothness is preserved due to the Laplacian being minimum in such regions. Consequently, the error maps in Fig. 4.6 along with scoring by radiologists in Supporting Table 4.3 suggest that NLDR$^{\mathbf{M}}$ reconstruction better approximates the details of image and is closest to diagnostic quality.

It is to be noted that the NLDR$^{\mathbf{2}}$ in Fig. 4.7 appears slightly sharper than NLDR$^{\mathbf{M}}$. It has been reported that in some situations, the enhanced piecewise constant features (artificial step-like features) resulting from the use of first order derivative of the image as smoothness measure (as in the case of second order diffusion) might actually be desirable because of the resulting sharper visual appearance and the apparent increase in resolution that comes with it (40). In such cases, if the step effects can enhance the diagnostic quality, it can be a good idea to reduce the regularization used even though the regularized result has smaller RLNE measure.

4.5.2 Computational constraint

One of the major advantages of conventional NL diffusion reconstruction is its computational efficiency compared to TV. Even though the computation time per iteration for NLDR$^{\mathbf{M}}$ is higher than NLDR$^{\mathbf{2}}$, it takes lesser number of iterations to converge. This reduction in the number of iterations can be understood from the fact that mixed-order solution removes more artifacts per iteration than its second-order counterpart. This is also supplemented with the fact that the mixed-order diffusion prevents formation of staircase artifacts, thereby reducing the need for its correction in the later iterations.

4.6 Conclusion

This chapter presented a fourth-order regularization of NL diffusion based MR image reconstruction to prevent formation of staircase artifacts in the solution and its application to DL based methods. Since NL diffusion is known to be an effective alternative to TV for edge preserving reconstruction, the crucial aspect of staircase artifact removal is addressed. Since the reconstruction is found to be stable for the experimentally determined range of the regularization parameter, a parameter search is not involved. Hence the computational simplicity of second-order diffusion is retained.

Chapter 5

Directionality-guided Non-Linear Diffusion Reconstruction

5.1 Introduction

Improving the image quality of CS-MRI reconstruction (1, 3, 6) has been investigated extensively in the last decade. In the previous two chapters, NL diffusion using PM diffusivity function (41, 42, 141, 148) is shown to be a better alternative to TV (37, 94, 160, 173-175), which has been the center feature of the edge-preserving reconstructions in CS-MRI (7, 38, 40, 93). Both these filters mainly rely on the underlying structure (edges/high-frequency information) of an image identified by its gradients to recover/reconstruct it. Despite not being superior to learning based approaches (96, 115, 117, 176, 177), application of edge-preserving filters as an auxiliary constraint continued to be highly popular (88, 113). This is because the preservation of sharp features by these filters can effectively complement the smooth approximation of the image by learned basis, and additionally has the advantage of representing the data using multiple sparse transform domains (113). It is also widely used in applications involving reconstruction of temporal variations due to their highly sparse nature in the finite difference representation (88, 111, 174, 178, 179). In order

to exploit these advantages of edge-preserving filters as an auxiliary constraint to learning based methods while achieving a stand-alone performance similar to that of learned reconstructions if not superior, it is imperative that the shortcomings of the conventional filters are addressed.

Due to the complex nature of the structural details present in an MR image, edges can be oriented along all possible angular directions. This can have a significant influence on the local variations in the rate of diffusion. For example, if we generate n filtered versions of the image by applying an edge preserved denoising filter along n different angular directions, different edges in the image are approximated better in different filtered versions. This strongly points towards the scope of an improved denoising routine if we can smartly choose the edges from those n filtered versions of the image, so as to efficiently combine them. The conventional approaches do not tune the reconstruction for these local variations and are therefore prone to miss important structural details in the image.

In a recent work of higher degree TV (HDTV) (38, 93), an anisotropic smoothing is proposed to enhance edges along all orientations. It is achieved by summing the absolute magnitude of directional derivatives along all angles and pixels instead of limiting the derivatives to just horizontal and vertical directions. This is shown to have a clear advantage over the classical TV based approaches in terms of image quality. However, in the presence of artifacts, summation of gradients along all directions is not desired if it leads to the preservation of intensity variation due to artifacts along some direction.

In this chapter, a sophisticated approach to map the individual edges from different filtered versions of the image is introduced so that for each individual edge, only the diffusion along its corresponding direction is considered. This helps to adapt the direction of diffusion to local variations in the directionality of edges and employs a precise diffusion in the local regions of the image on a sub-pixel level, leading to the preservation of the complex nature of edges.

5.2 Edge-Preserving CS-MRI

Given the acquired samples in k-space K with a support $\Omega \subset \mathbb{C}^{M\times N}$, as pointed out in the third chapter, an edge-preserving CS-MRI reconstruction problem can be formulated as the minimization of a cost function of the form

$$\underset{U}{\operatorname{argmin}}\ \mathcal{H}(U)\ such\ that\ \|K_u - \mathcal{F}_u U\|_2 < \varepsilon, \qquad [5.1]$$

where $\mathcal{H}(U)$ is a sparsifying filter that imposes explicit penalty for edges in U, $\|K_u - \mathcal{F}_u U\|_2$ measures the deviation of the reconstructed k-space from K_u and ε controls the fidelity of reconstruction to the acquired k-space.

5.2.1 Non-linear filtering using anisotropic diffusion

The objective of NL diffusion used in CS-MRI is to promote the sparsity in image gradients (∇U) by diffusing U over a small time ∂t as

$$\partial U = \gamma div(g(|\nabla U|)\nabla U). \qquad [5.2]$$

The reconstruction model biases the diffusion of U by enforcing fidelity to the acquired k-space at each iteration (k) as shown in Eqs. [5.3a-5.3b].

$$\widehat{U}^{(k)} = U^{(k-1)} + \gamma div\left(g\left(\left|\nabla U^{(k-1)}\right|\right)\nabla U^{(k-1)}\right), \quad [5.3a]$$

$$U^{(k)} = \widehat{U}^{(k)} + c\mathcal{F}_u'\left(K_u - \mathcal{F}_u\widehat{U}^{(k)}\right). \quad [5.3b]$$

As described in chapter 3, the diffusivity function used in PM diffusion reconstruction is given by

$$g(|\nabla U|) = \frac{1}{1+(|\nabla U|/\alpha)^2}, \quad [5.4]$$

where α is the contrast parameter which is a threshold that separates the gradient magnitudes of noise and true edges and the numerical scheme of NLDR becomes equivalent to that of TV when the diffusivity function (151) is

$$g(|\nabla U|) = \frac{1}{|\nabla U|}. \quad [5.5]$$

Since the technique proposed in this chapter is independent of the choice of g, it is directly applicable to reconstruction using TV as well. Therefore, hereon in this chapter, readers may also interpret all mentions of NL diffusion as TV. Furthermore, wherever not specifically denoted as NLDR^{M}, PM reconstruction refers to NLDR^{2}.

5.3 Influence of Gradient Direction on Reconstruction Performance

5.3.1 Diffusion of edges

Discretization of PM diffusion generally approximates the gradients at pixel p to horizontal and vertical directions by a finite difference operation on its 4-pixel neighborhood, $\eta_p^0 = \{N, S, E, W\}$, where N, S, E and W are the neighboring pixels of

p in the North, South, East and West directions. For example, the explicit numerical scheme of Perona and Malik updates p as

$$U^{(k+1)}(p) = U^{(k)}(p) + \gamma \sum_{n \in \eta_p^0} g\left(\left|\nabla U^{p,n\,(k)}\right|\right) U^{p,n\,(k)}, \qquad [5.6]$$

where $\nabla U^{p,n}$ represents the difference in intensity between p and its neighbor n, $n \in \eta_p^0$.

While these approximations are computationally efficient, they work better when the edges are mostly oriented along the horizontal and vertical directions. For example, consider the diffusion of a synthetic image shown in Fig. 5.1(a) having three edges (lines in the figure are considered as edges) that are oriented along 0^0, 90^0 and -45^0 (vertical edge is considered to have an angular orientation of 0^0). Fig. 5.1(b) depicts the result of diffusion after 100 iterations using Eq. [5.2].

Here gradients are computed along horizontal and vertical directions. Consequently, the edges aligned perpendicularly with these directions diffuse at a similar rate, different from the rate at which the other edge diffuses. This indicates that the gradients computed based on the actual orientation of edges has distinct advantage in terms of its preservation.

5.3.2 Diffusion of artifacts

Although the fidelity term in biased reconstruction generally helps to preserve relevant edges, the sensitivity to diffusion direction will factor in more at higher undersampling rates where biasing is less effective. In fact, even in the presence of strong bias, the

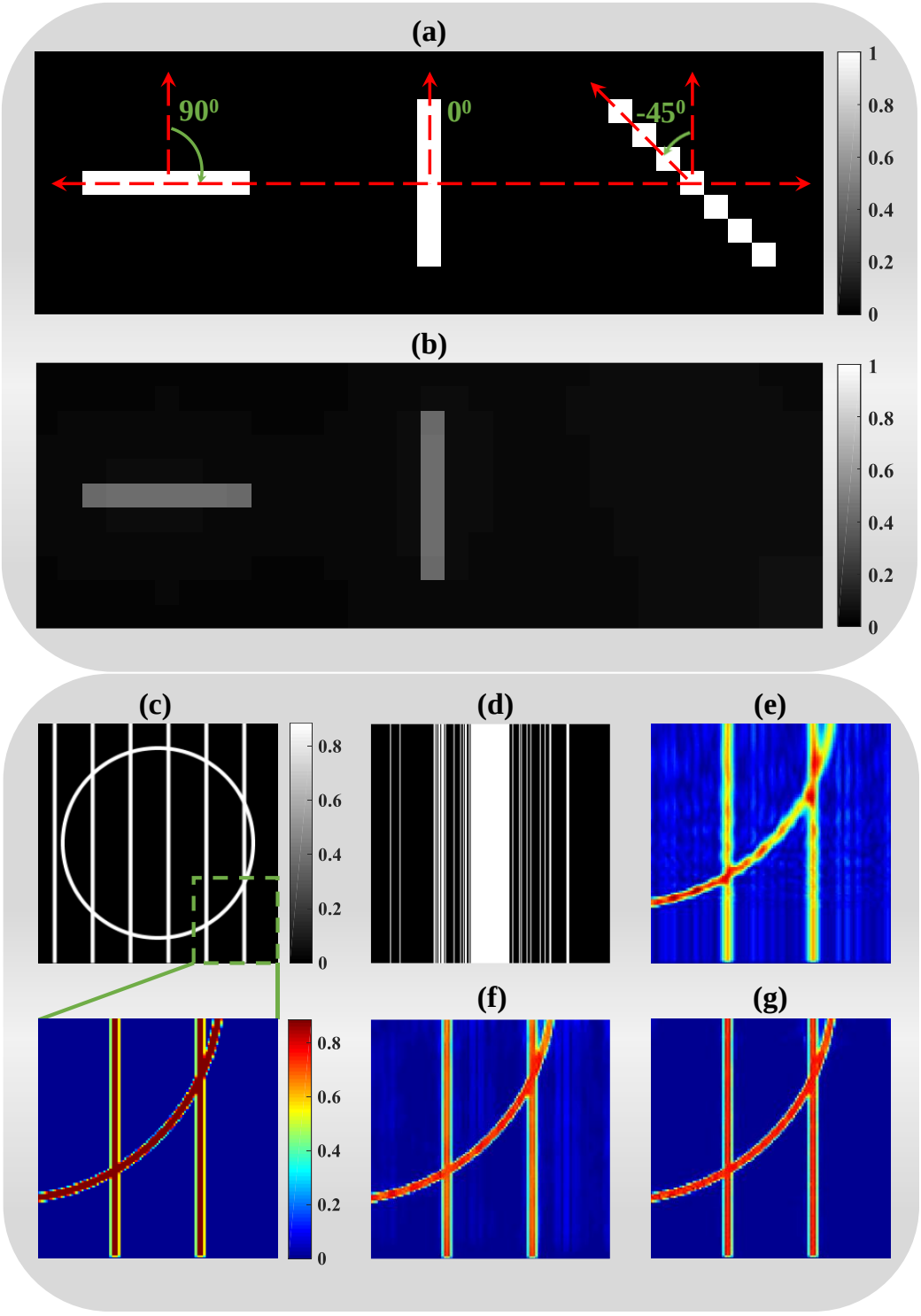

Figure 5.1. Diffusion of synthetic edge image. (a) ground truth-1. (b) reconstructed image after 100 iterations of diffusion. (c) ground truth-2. (d) sampling mask. (e) inverse Fourier transform of k-space having zeros at unacquired locations. (f) image reconstructed with 100 iterations of biased diffusion along horizontal and vertical directions. (g) image reconstructed with 100 iterations of biased diffusion when directions of diffusion are changed by 45 degrees.

rate of diffusion of artifacts is still dependent on the direction of the gradient computation.

For example, consider the reconstruction of the ground truth shown in Fig. 5.1(c) undersampled using the binary sampling mask shown in panel (d). Inverse Fourier transform after setting the unacquired samples of k-space as zeros is depicted in panel (e). It shows strong intensity variations in the horizontal direction due to aliasing interference. The image reconstructed by 100 iterations of biased NL diffusion along the horizontal and vertical directions is shown in panel (f). The reconstructed image shown in panel (g) is obtained after the same number of iterations when the directions of diffusion are changed by 45 degrees.

With biasing, most of the structural details in the ground truth are preserved in both reconstructions. However, the remnant aliasing appears stronger in panel (f). This is because the gradients used in this case suggest that the variations in intensity function at the locations of the artifacts are significant and are preserved.

5.4 Reconstruction by Directionality Guided NL Diffusion

The main idea is to exploit the connection between gradient direction and directional orientation of edges to diffuse off artifacts and best retain structural details. This involves (i) biased NL diffusion in different directions using an extended neighborhood and (ii) mapping of edges from the images diffused along different directions. The mapping process includes an option to guide the diffusion directions based on the state-of-the-art techniques like patch based non-local operator (PANO)

(115) or the optimization of sparsity in a learned dictionary (96). This is described in detail in the following subsections.

5.4.1 Extended neighborhood and gradients

With the assumption that the edges defining the boundaries of anatomical features in U are aligned in q different directions, U should be ideally diffused along q different directions (as discussed in section 2.2) to best retain its structural integrity. To realize this, a custom neighborhood is defined for p as illustrated in Fig. 5.2.

The conventional 4-pixel neighborhood η_p^0 of p is depicted in Fig. 5.2(a). One can consider an additional system of n neighborhoods η_p^i, $i = 1, \dots, n$, each separated by an angle θ and all neighbors located at the same distance d from p. Following this convention, Fig. 5.2(b) shows the neighborhood η_p^1 and Fig. 5.2(c) illustrate the collection of all such $n + 1$ neighborhoods of p.

Given all the intensity values in U (red and black pixels), standard interpolators like the conventional bilinear interpolator or a bicubic spline interpolator (180-184) can be used to estimate η_p^i (blue colored pixels). Denoting the pixel locations of neighbors W_i as (x_{W_i}, y_{W_i}) and the central pixel as (x_p, y_p), a location (x, y) with distance d from (x_p, y_p) and subtending an angle θ with the line joining (x_{W_0}, y_{W_0}) and (x_p, y_p) is given by

$$\begin{bmatrix} x \\ y \end{bmatrix} = \begin{bmatrix} x_p \\ y_p \end{bmatrix} + \begin{bmatrix} cos(\theta) & sin(\theta) \\ -sin(\theta) & cos(\theta) \end{bmatrix} \begin{bmatrix} (x_{W_0} - x_p) \\ (y_{W_0} - y_p) \end{bmatrix}. \quad [5.7]$$

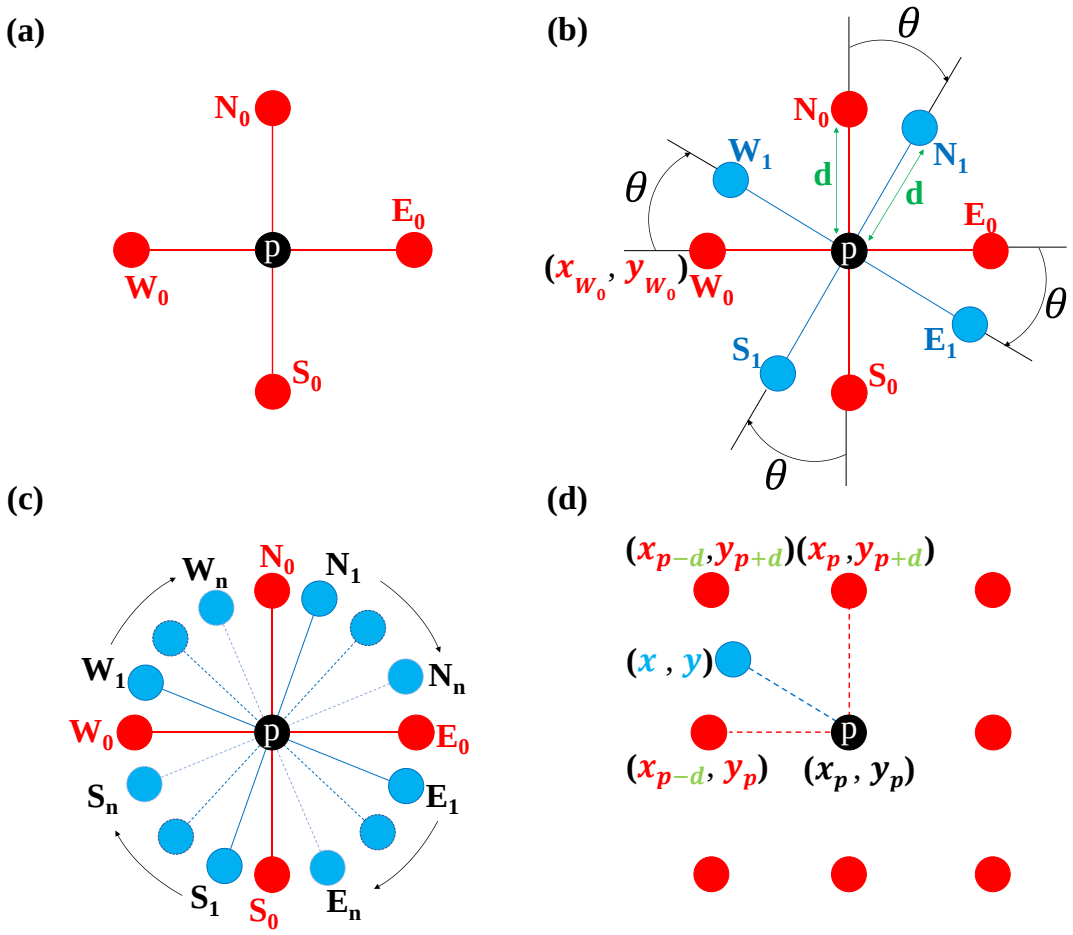

Figure 5.2. Extended neighborhood representation. (a) 4-pixel neighborhood (η_p^0) of pixel p. (b) set of four pixels (blue circles) located at an angle θ from η_p^0 (red circles). (c) complete set of neighborhoods of p. (d) an extended neighborhood system. Intensities are known at the red colored grid locations and estimated at the blue colored locations.

Using bilinear interpolation, for example, if the values at the grid locations (x_p, y_p), (x_{p-d}, y_p), (x_p, y_{p+d}) and (x_{p-d}, y_{p+d}) enclosing (x, y) in Fig. 5.2(d) are known, then the interpolated value at (x, y) is given by

$$U(x,y) \approx a_0 + a_1 x + a_2 y + a_3 xy, \qquad [5.8]$$

where the coefficients a_0, a_1, a_2 and a_3 are obtained by solving the linear system

$$\begin{bmatrix} 1 & x_{p-d} & y_{p+d} & x_{p-d}y_{p+d} \\ 1 & x_p & y_{p+d} & x_p y_{p+d} \\ 1 & x_{p-d} & y_p & x_{p-d}y_p \\ 1 & x_p & y_p & x_p y_p \end{bmatrix} \begin{bmatrix} a_0 \\ a_1 \\ a_2 \\ a_3 \end{bmatrix} = \begin{bmatrix} U(x_{p-d}, y_{p+d}) \\ U(x_p, y_{p+d}) \\ U(x_{p-d}, y_p) \\ U(x_p, y_p) \end{bmatrix}. \qquad [5.9]$$

Similar to Eq. [5.9] for quadrant-1, the desired locations can be expressed with reference to the angle θ measured clockwise with respect to lines joining N_0, E_0 or S_0 with p. Accordingly, the four neighborhood points enclosing (x, y) will differ. With the estimated intensity values of the extended neighbors, the gradient can be computed as $\nabla_i U(p) = \left[U(x_{E_i}, y_{E_i}) - U(x_p, y_p), U(x_{N_i}, y_{N_i}) - U(x_p, y_p)\right]^T$ in η_p^i.

5.4.2 Biased diffusion in extended neighborhood

From Eqs. [5.3a-5.3b], the biased diffusion of U in η^i would result in

$$\widehat{U}_i^{(k+1)} = U^{(k)} + \gamma div\left(g\left(\left|\nabla_i U^{(k)}\right|\right)\nabla_i U^{(k)}\right), \qquad [5.10a]$$

$$U_i^{(k+1)} = \widehat{U}_i^{(k+1)} + c\mathcal{F}_u'\left(K_u - \mathcal{F}_u \widehat{U}_i^{(k+1)}\right). \qquad [5.10b]$$

Diffusing $U^{(k)}$ over $n+1$ sets of neighbors would therefore yield

$$\mathbb{U}^{(k+1)} = \left\{U_0^{(k+1)}, U_1^{(k+1)}, \ldots, U_n^{(k+1)}\right\}, \qquad [5.11]$$

where $\mathbb{U}$ is the set of all diffused versions of U. Now, we need to generate $U^{(k+1)}$ from $\mathbb{U}^{(k+1)}$ such that individual edges in $U^{(k+1)}$ are mapped from different elements of $\mathbb{U}^{(k+1)}$.

5.4.3 Mapping of edges based on directionality property

Let U^{ideal} be an ideal image that exhibit the desired true directional properties at a location (x, y). Then the mapping of $\mathbb{U}$ to U (denoted as $map(\mathbb{U} \longrightarrow U)$) can be defined as

$$U(x,y) = U_j(x,y) \mid j = \min_i \left(dir\left(U^{ideal}(x,y)\right) - dir\left(U_i(x,y)\right)\right), \quad [5.12]$$

where the function $dir(p)$ defines the direction of gradient of p. However, this is not reliable when a prior information about $dir\left(U^{ideal}(x,y)\right)$ is not available. This limitation can be mainly attributed to the difficulty in estimation of underlying true structural details from an artifact corrupted MR image. In the frequency domain, however, we generally have a partial information available that Fourier encodes the true structural details. Therefore, it is more meaningful to define a surrogate rule based on the principle that the mapping of individual edges which minimizes the deviation of the solution from a reliable set of k-space samples is the best possible solution.

Following this principle, let us assume that there exist a k-space $\mathbb{K}$ such that $\mathbb{K} = \mathcal{F}\left(U^{ideal}\right)$, where $\mathcal{F}$ is the Fourier transform operator. Then the deviation of each element in $\mathbb{U}$ from $\mathbb{K}$ can be measured as

$$\mathrm{E}_i = |\mathcal{F}^{-1}(\mathcal{F}(U_i) - \mathbb{K})|, \; i = 0,1,\dots,n. \quad [5.13]$$

Algorithm 5.1:

0: Set $k = 1$; $t^{(1)} = 1$;

1: $U_{\ell}^{(0)} = \mathcal{F}_u'\left(K_{u,\ell}\right)$; % '$\ell$' is the channel number

2: $while\ (k < k_{max})$

3: $\widehat{U}_{\ell}^{(k)} = U_{\ell}^{(k-1)} + c\,\mathcal{F}_u'\left(K_{u,\ell} - \mathcal{F}_u U_{\ell}^{(k-1)}\right)$; % biasing

4: $for\ \ i = 1{:}n$

5: $U_{\ell,i}{}^{(k)} = \widehat{U}_{\ell}{}^{(k)} + \gamma div\left(g\left(\nabla_i \widehat{U}_{\ell}{}^{(k)}\right)\nabla_i \widehat{U}_{\ell}{}^{(k)}\right)$; % diffusion

6: end

7: $map\left(\left\{U_{\ell,0}^{(k)}, U_{\ell,1}^{(k)}, \ldots, U_{\ell,n}^{(k)}\right\} \longrightarrow U_{\ell}^{(k)}\right)$; % edge mapping

8: $t^{(k+1)} = \left(1 + \sqrt{1 + 4(t^{(k)})^2}\ \right)/2$;

9: $U_{\ell}^{(k)} = U_{\ell}{}^{(k)} + \left(t^{(k)} - 1\right)\left(U_{\ell}{}^{(k)} - U_{\ell}{}^{(k-1)}\right)/t^{(k+1)}$; % acceleration

10: $k = k + 1$;

11: end

This enables us to formulate a surrogate mapping rule given by

$$U(x,y) = U_j(x,y) \mid j = \min_i\left(E_i(x,y)\right). \qquad [5.14]$$

Since U^{ideal} and $\mathbb{K}$ are directly related by the Fourier operation, $\mathrm{E}_i(x,y)$ will be minimum always for that i for which the directional orientation of $U_i(x,y)$ matches the most with $U^{ideal}(x,y)$. Therefore, it can be used in place of Eq. [5.12] to choose i. While reconstructing individual channels, mapping is performed for each channel as

$map\left(\mathbb{U}_{\ell}^{(k+1)} \longrightarrow U_{\ell}^{(k+1)}\right)$, where v is the channel number and $\mathbb{U}_{\ell}^{(k+1)} = \left\{U_{\ell,0}^{(k+1)}, U_{\ell,1}^{(k+1)}, \dots, U_{\ell,n}^{(k+1)}\right\}$. Individual channel k-space with unacquired frequency points set to zero is then denoted as $K_{u,v}$. A basic workflow of the proposed reconstruction and the associated mapping operation are illustrated in Figs. 5.3-5.4.

Algorithm 5.1 describes the algorithmic steps of proposed directionality guided non-linear diffusion reconstruction. The acceleration technique of FISTA (25) is used to speed up the reconstruction process in steps 8 and 9. Shaded blocks in Fig. 5.3 represent the major changes to conventional NLDR model. 'Custom prior optimization' is a customizable block based on the choice of $\mathbb{K}$**.** This is explained in the subsequent subsection. Dotted arrows indicate that the step is optional.

5.4.4 Choice of $\mathbb{K}$

Equation [5.14] relies on the information contained in $\mathbb{K}$ as a guide for mapping the edges. Below, two ways of choosing $\mathbb{K}$ are proposed.

A) $\mathbb{K}$ based on **acquired k-space**: We would expect that some information about the directionality of edges in the to-be-reconstructed image is Fourier encoded in the acquired samples of K. Therefore, a straightforward choice of $\mathbb{K}$ would be K_u, which modifies Eq. [5.13] as

$$\mathrm{E}_i = |\mathcal{F}_u'(\mathcal{F}_u(U_i) - K_u)|, \; i = 0,1, \dots, n. \qquad [5.15]$$

While it serves the purpose well, the reliability of the deviation measure can be dependent on the sampling rate as well. This reconstruction is denoted as $\mathbf{K_UTV}$ or $\mathbf{K_UPM}$, indicating whether TV or PM diffusivity function is used.

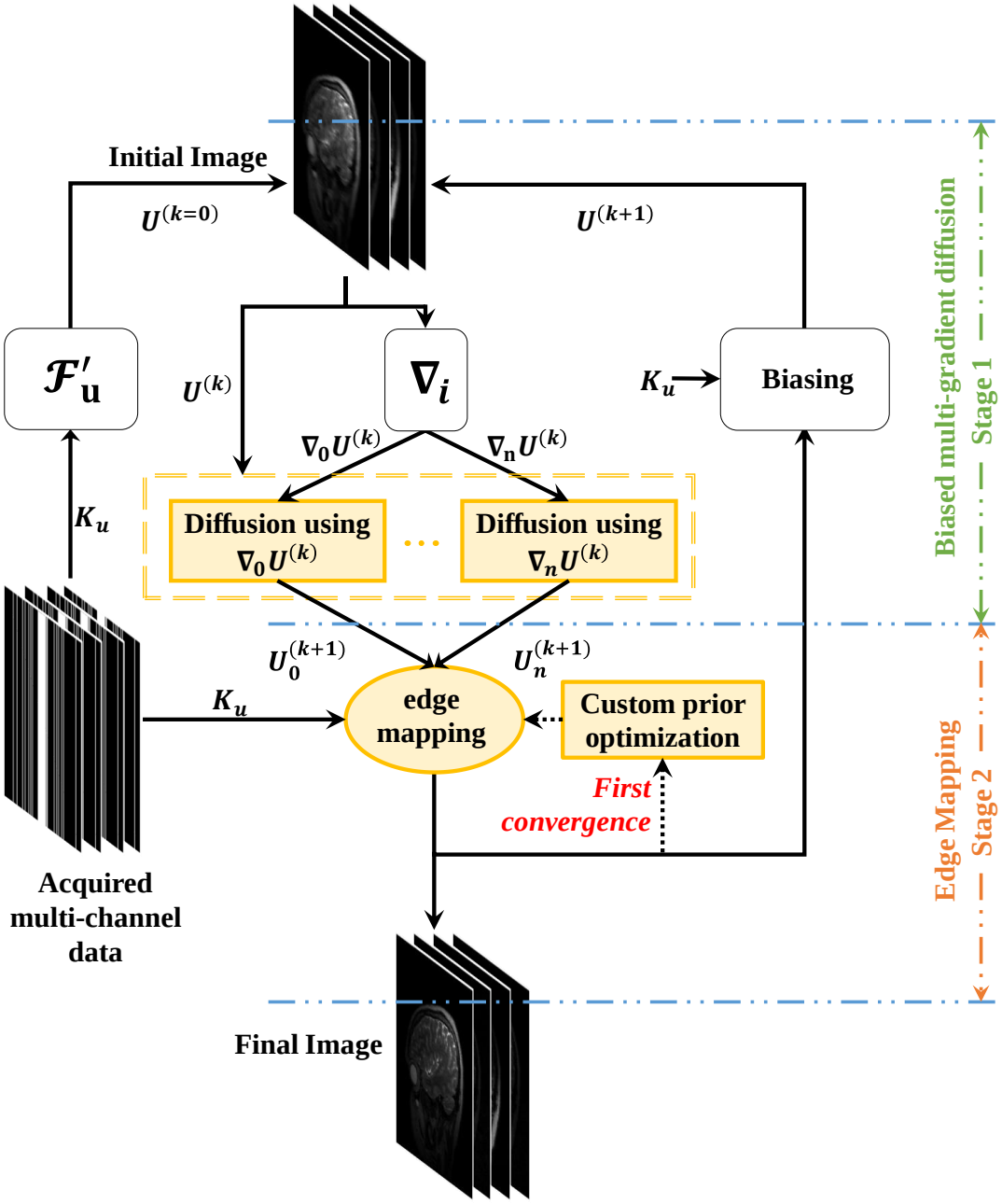

Figure 5.3. Process flow of multi-gradient biased diffusion reconstruction with edge mapping. The edge-mapping process is detailed in Fig. 5.4.

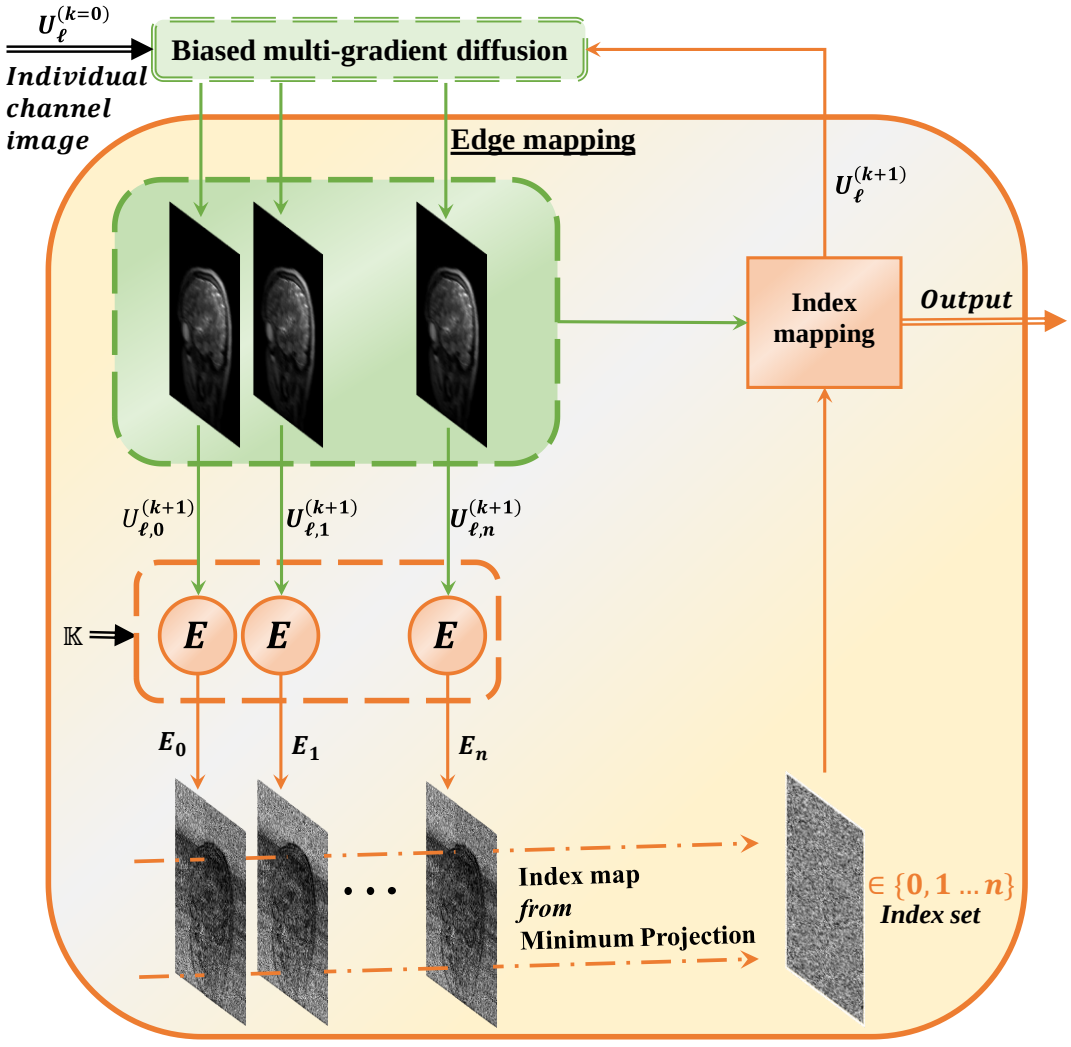

Figure 5.4. Process flow of edge mapping procedure.

B) $\mathbb{K}$ based on **custom prior optimizable k-space**: Each reconstruction technique tries to optimize a prior information about the data during reconstruction, like the sparsity in a learned dictionary, or a non-local similarity in the underlying structure which also influences the directionality of edges that are recovered. This in turn gets Fourier encoded in its k-space. Such a custom prior optimized k-space (K_{po}), can therefore be used as a guide for mapping the edges. At the locations of acquired samples in the k-space, however, the values in K_u are the closest reliable information that we have to the solution which we are seeking.

Therefore, we can use a synthesized k-space K_s as $\mathbb{K}$ where $K_s = K_u(\Omega^+) \cap K_{po}(\Omega^-)$. Ω^+ and Ω^- denotes the locations of acquired and unacquired samples of $\mathcal{F}(U)$, respectively. Then, Eq. [5.13] becomes

$$\mathrm{E}_i = |\mathcal{F}^{-1}(\mathcal{F}(U_i) - K_s)|,\ i = 0,1,\dots,n. \qquad [5.16]$$

For example, let us consider PANO that optimizes the non-local structural similarity in the image using a patch-based similarity mapping. We can incorporate this in the proposed framework by choosing $K_s = K_u(\Omega^+) \cap K_{PANO}(\Omega^-)$, where K_{PANO} is the structural similarity optimized k-space.

In fact, a better performance may be achieved by using a two-step reconstruction in which PANO is used to optimize the structural similarity in the output of $\mathrm{K_U}$TV/$\mathrm{K_U}$PM to generate K_{po}. This is denoted as **$\mathbf{K_P}$TV**/**$\mathbf{K_P}$PM**. This workflow is indicated by the dotted arrows in Fig. 5.3. Similarly, the state-of-the-art dictionary learning MRI (DLMRI) (96) can be used to generate K_{po} by enhancing sparsity in the

output of K_UTV/K_UPM when represented using dictionaries learned from it (denoted as **K_DTV/K_DPM**).

The custom prior optimization can be independent of the output of K_UTV/K_UPM as well. For example, the state-of-the-art method of block matching and 3D filtering (BM3D) (117, 185) can generate K_{po} by enhancing sparsity in the initial image by grouping similar blocks and shrinking its sparse transform domain coefficients (denoted as **K_BTV/K_BPM**).

5.4.5 Edge emphasis correction

Edge-preserving filters like PM diffusion and TV also have an inherent property of enhancing the edges (42). This in effect emphasizes the discontinuities in the intensity function. While edge enhancement is a handy post-processing tool and can favor the diagnosis in many cases, the modulation of higher frequencies in the k-space due to these enhanced edges may not always be favorable in the reconstruction process, especially in the initial iterations where the edges can also be due to artifacts.

The increasing sharpness of edges correspond to an extended support in the frequency domain. Therefore, we can limit the overemphasis of edges by extending the fidelity/data-consistency constraint to regions outside the acquired k-space denoted by $\bar{\Omega}, K(\bar{\Omega}) \in \{0\}$ at the cost of increased matrix size/computation. This extension implies that the spatial frequencies in extended support region should not be present in the absence of sharpened edges.

5.5 Methods

5.5.1 Implementation

Proposed method can be implemented in two ways. In the absence of channel sensitivity ($\mathcal{C}_\ell$) information, both diffusion and edge mapping are performed channel-wise. Otherwise, both operations are performed on the channel combined image ($\mathcal{U}$). The iterations are then initialized by combining channel images using the sensitivity profile ($\mathcal{U}^{(0)} = \sum_v \left(\mathcal{C}_v^* * U_\ell^{(0)}\right)$, where $\mathcal{C}_\ell^*$ is the complex conjugate of $\mathcal{C}_\ell$ and $U_\ell^{(0)} = \mathcal{F}_u'\left(K_{u,\ell}\right)$). The data fidelity (bias) update term in Eq. [5.10b] then becomes $c\sum_\ell \left(\mathcal{C}_\ell^* * \mathcal{F}_u'\left(K_{u,\ell} - \mathcal{F}_u\left(\mathcal{C}_\ell * \hat{\mathcal{U}}^{(k+1)}\right)\right)\right)$, where $\hat{\mathcal{U}}^{(k+1)}$ is the diffused version of $\mathcal{U}^{(k)}$.

Among the different state-of-the-art edge preserving reconstruction techniques compared in this work, total generalized variation (TGV) (168) operates directly on $\mathcal{U}$. Therefore, the proposed method operates on $\mathcal{U}$ when compared with TGV for fair comparison. When the numerical experiments require direction of edges to be known a priori, ground truth is used as a guide ($\mathbb{K}$) to choose the direction of diffusion (denoted as **$\mathbf{K_{GT}}$TV**/**$\mathbf{K_{GT}}$PM**).

5.5.2 Reconstruction parameters

Parameters controlling the reconstruction are c, γ, α and n. In multi-channel MRI, complete structural information is absent in individual channels and the presence of channel sensitivity degrades the quality of true edges. Therefore, α is better estimated

from $\mathcal{U}$ as reported in chapter 3**,** where it is estimated as the mean absolute deviation (MAD) of $\nabla\mathcal{U}$ (160). With the availability of $\mathcal{C}_\ell$, we have $U_\ell = \mathcal{C}_\ell\mathcal{U}$. Therefore, diffusion can be directly applied on $\mathcal{U}$ as opposed to reconstructing individual channels by diffusion and then combining it (40, 61). Furthermore, in such cases, conjugate gradient method also can be used to solve the fidelity constraint (bias) to enforce an accurate data consistency (139).

5.5.3 Choice of reconstruction parameters

As opposed to PM diffusivity function, the reconstruction using TV diffusivity function is known to be sensitive to the choice of γ (160). Therefore, TV requires search optimization of γ. In either case, relaxation of c is desired when the acquired data are noisy and the best choice in such cases requires monitoring final reconstructions corresponding to different values of c. With c is set to 1, the adaptation of α helps to minimize the remnant noise in PM diffusion (160).

Diffusion in η_p^i for each i is similar to that of the conventional NL diffusion in η_p^0. Therefore, the choice of c, γ and α are independent of the number of sets of neighbors used and behaves similar to that of the conventional NLDR reconstruction. For both TV and PM, a steady decrease in reconstruction error is observed when n is incremented from 2 to 10 (shown in Fig. 5.5). However, this gain is found to be minimal for $n > 10$. Following this result, $n = 10$ is used for all numerical experiments in this work. However, the ideal directions of gradient to be used depend on the structural details of the image at hand and hence can vary from dataset to dataset. Therefore, the best practice is to include all possible choices of directions.

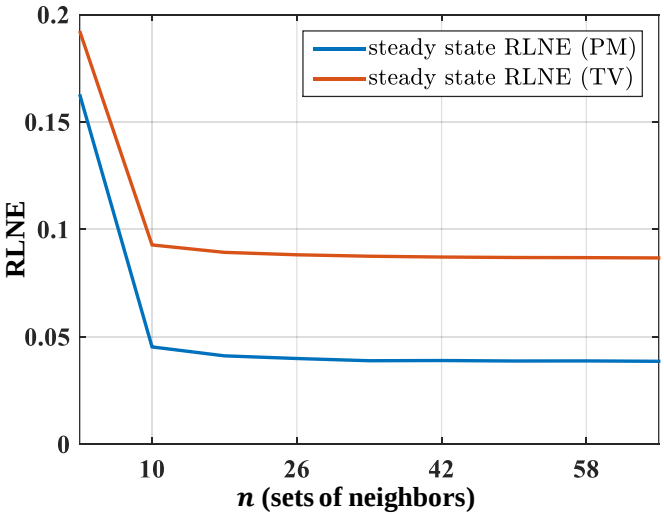

Figure 5.5. Influence of n on steady-state error. steady-state RLNE is plotted against n for TV and PM diffusion based K$_U$NLDR reconstruction.

5.5.4 Hypothesis test

Z-test is used to check whether the PSNR measures have significant difference across different ROIs. The measured variable is the PSNR value in each ROI. ROIs are chosen randomly with different sample sizes across the image. Using a collection of 10^4 ROIs, estimates of the population mean (μ) and population variance (σ^2) are obtained. For each sample ROI, the z-score is calculated using

$$z = (\mathbb{M} - \mu)/\sqrt{\sigma^2/\aleph}, \qquad [5.17]$$

where $\mathbb{M}$ is the sample mean and $\aleph$ denotes the sample size. The probability measure, p-value (186) associated with the computed z-score indicates whether the hypothesis that the 'PSNR measure of sample does not differ significantly from the population' is acceptable. If the p-value is greater that a confidence level of 0.01, the hypothesis is accepted.

5.5.5 Datasets

Different datasets used in this study include (i) physical phantom acquired on a 3T MRI scanner using a turbo spin-echo sequence with a 220mm×292mm field of view (FOV) on a 256×340 cartesian sampling grid with 16 receiver coils. This is publicly available in (155), (ii) brain images of size 256×256 acquired from a healthy volunteer on 3T MRI scanner using T2-weighted turbo spin echo sequence (TR/TE=6100/99ms, FOV=220×220mm^2, slice thickness = 3mm) and (iii) 12-channel brain images acquired using 3D T2 CUBE sequence with Cartesian readouts having matrix dimensions of 256×232×208 with 1 mm isotropic resolution. The same in vivo datasets were previously used to evaluate the performance of CS-MRI reconstructions in (97, 114, 115, 139). The coil sensitivity maps of 12-channel brain images were estimated from the central k-space regions of each slice using ESPIRiT (87) and were assumed to be known during experiments.

5.6 Results

Experimental results and their comparison with state-of-the-art techniques are presented in this section. The promising potential of directionality optimized reconstruction applied to multi-channel real MRI dataset for the limiting cases of 95-97% undersampling is illustrated first. Then the results of more practical ways of choosing the direction of diffusion is shown and illustrate how the errors and convergence in each case are influenced by the choice of parameters such as the number of gradient directions and step-size. All implementations are performed using Matlab (The MathWorks, Inc., Natick, MA, USA) on a PC with an Intel Xeon E5-

2630v3 2.4 GHz processor and 32GB of RAM running Windows 7 operating system. Links to the source codes for Matlab implementations of all the state-of-the-art methods compared in this work are listed in (166, 168, 169, 187, 188).

5.6.1 Reconstruction of 95-97 percent undersampled data

In this numerical experiment, it is assumed that the directional properties of edges are known a priori. Reconstructed images are depicted in Fig. 5.6. Panels from left to right in the top row shows undersampling masks and the ground truth. Panels from left to right in rows 2 to 4 illustrate the results of PM, K_{GT}PM, TV and K_{GT}TV respectively. Corresponding PNSR values are indicated in the inset.

The results indicate that an additional information about the direction of diffusion has the potential to bring forth a massive 12.33dB improvement for PM diffusion and around 7dB improvement for TV on average. In the very limiting cases of 3% and 5% sampling studied, this improves the output of state-of-the-art reconstructions to visually acceptable standards. The sampling pattern acquiring only 13 phase-encoding lines corresponds to approximately 3% samples for phantom and 5% samples for the head data. 52 PE lines correspond to approximately 20% samples for the head data. It may be noted that the phantom despite sampled at a lower percentage, tend to generate higher PSNR measures. This can be attributed to the fact that structural complexity of the phantom is lower than that of the head dataset, which is obvious from a visual comparison of the ground truths.

After using z-test to test different ROIs of size ranging from 16x16 to 128x128, it was concluded that there is no significant difference between the PSNR measures of

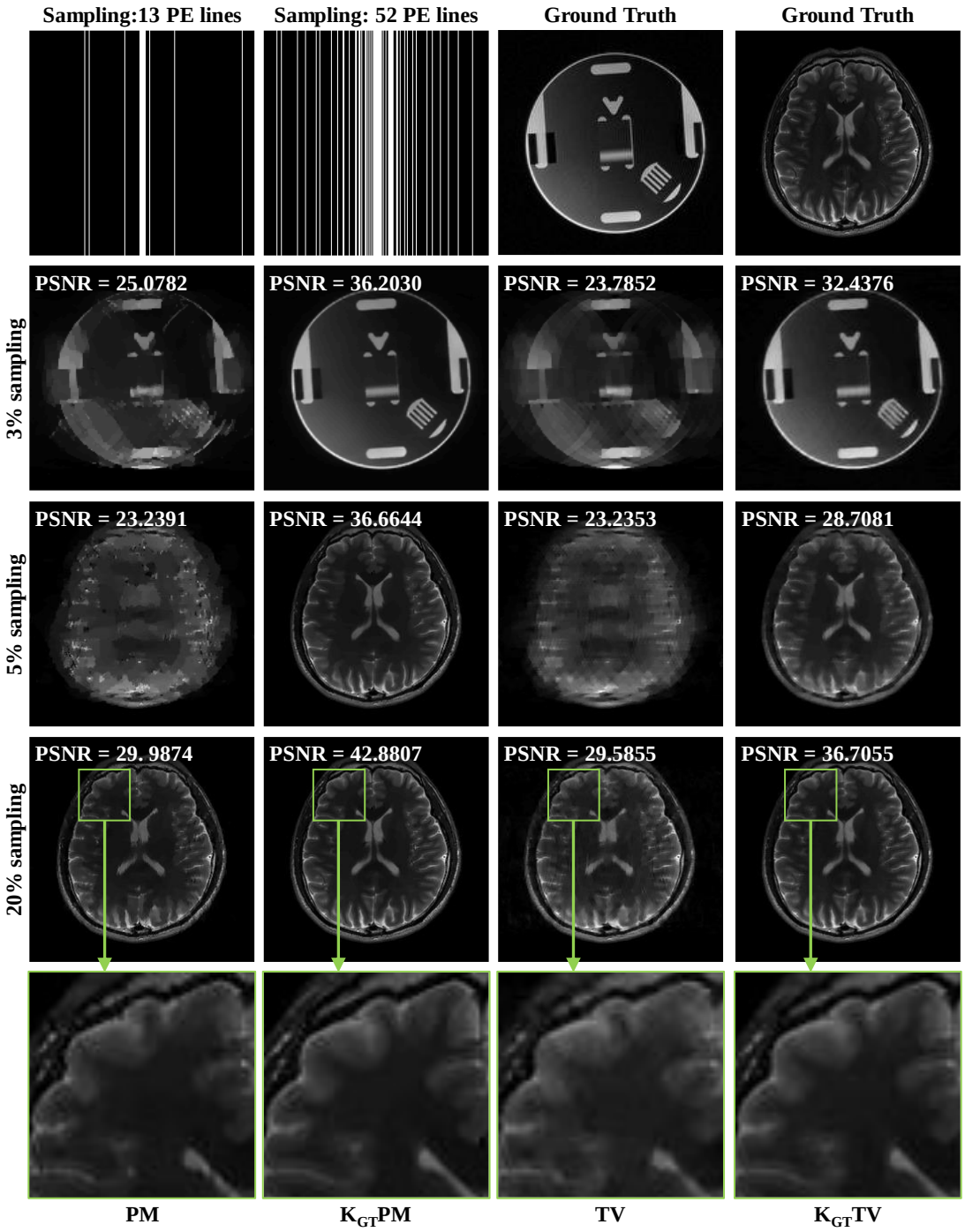

Figure 5.6. Reconstruction of phantom and in vivo MRI data with random phase encoding (PE) sampling. Panels in the first row show the ground truth images and sampling patterns used. Remaining panels in a column-wise arrangement show images reconstructed using TV and PM diffusion with and without diffusion direction optimization. Here, the direction of diffusion is assumed to be known apriori. Corresponding PSNR measures for the whole images are shown in the insets.

randomly drawn ROIs from the mean PSNR value of the total population of ROIs. For example, a 1000 randomly drawn ROIs of size 64x64 give an z-score of -1.5599. The associated p-value of 0.11876 is greater than the confidence level of 0.001, indicating that there is no significant difference in PSNR values.

5.6.2 Effect of number of directions

The effect of number of sets of neighborhoods (n) in reconstruction is studied by observing the steady-state RLNE for different choices of n. This is illustrated in Fig. 5.7 along with a comparison of how TV and PM diffusion choose the gradient directions for the reconstruction. Top-left panel shows the ground truth and enlarged view of the neighborhoods of two pixels p1 and p2. p1 can be considered as a pixel belonging to two different edges, one at ~30^0 (to its left side) and the other at 90^0 (to its right side). p2 on the other hand can be considered to be a part of an edge at 0^0. Ground truth is retrospectively undersampled by sampling 76 PE lines out of 256 to achieve a sampling rate of 30%.

Panels in right column show the number of times (ϱ) diffusion is performed along a given direction as a function of the angular direction used. It is observed that the choice of direction is more distributed in PM as compared to TV, especially for p1. That is, in TV, the choice of direction for p1 is mostly confined to 90^0. For p2, however, it is more distributed. Consequently, the difference in RLNE of TV and PM (shown in the inset) is higher for p1 than p2. The reconstructed neighborhoods and their respective error images are shown in the bottom-left panel.

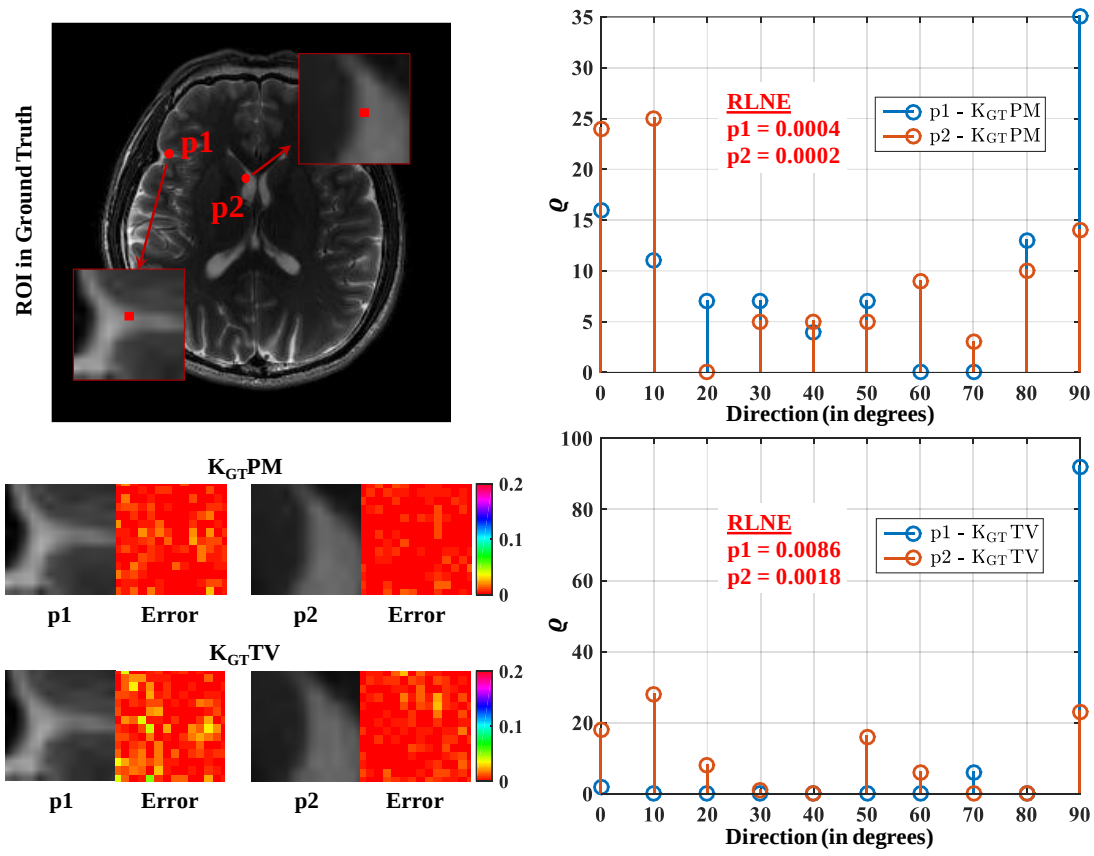

Figure 5.7. Effect of number of diffusion directions on image quality. Panels in the first column show the ground truth image and reconstructed pixel neighborhoods. Panels in second column show the number of times (ϱ) diffusion is performed along a given direction, as a function of the angular direction used.

5.6.3 Custom prior guided reconstruction

Images of head dataset reconstructed using proposed method guided by different custom prior optimizations are shown in Fig. 5.8. Ground truth is retrospectively undersampled to achieve a sampling rate of 30%. Corresponding PSNR measures are indicated in the inset. Panels in the bottom row depict sampling mask and difference images. While K_PTV, K_PPM and BM3D indicates an improvement close to 2dB, K_DTV and K_DPM show 3dB improvement in PSNR over TV and PM reconstructions. The difference images clearly indicate that the proposed method leads to a more faithful reproduction of structural details, especially in the regions of ventricular margins and cortical gray-white interface. While blocky effects are clearly visible in PM and TV reconstructions, the proposed directionality guided diffusion appears to be tolerant to these effects as well. This is also evident from the PSNR measures compared with that of $NLDR^M$ reconstruction listed in Table 5.1.

A detailed comparison with different state-of-the-art reconstructions (38, 96, 115, 117) are listed in Table 5.1. These values are averaged from reconstructions of the dataset undersampled using Poisson-disc, radial and random phase-encode sampling patterns. As expected, K_{GT}TV and K_{GT}PM show a significant improvement of 7.78dB and 10.99dB on average over TV and PM. The next best results are observed for K_DPM with an improvement of 4.25dB and 3.88dB on average over TV and PM and 2.36dB, 1.92dB and 1.59dB over BM3D, PANO and DLMRI respectively.

In Fig. 5.9, K_UPM and K_{GT}PM are compared with TGV and conventional PM diffusion reconstruction techniques. Row-wise panels show the ground truth and images reconstructed after retrospectively undersampling the ground truth by sampling

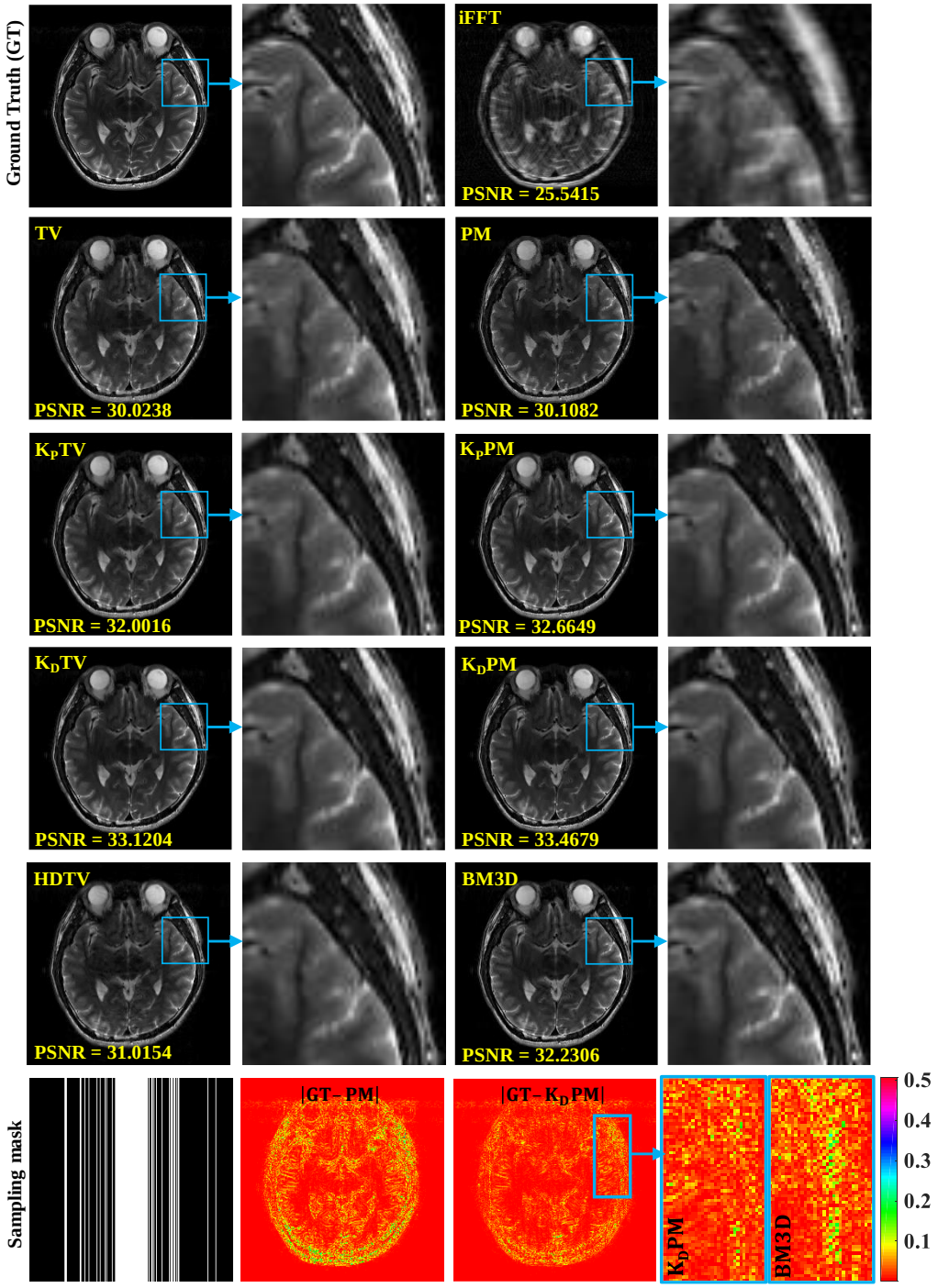

Figure 5.8. Reconstruction of in vivo MRI data using custom prior optimized multi-directional diffusion. Left and right panels in the first row depict the ground truth image and inverse Fourier transform of k-space filled with zeros at unacquired locations. Bottom left panel shows the sampling mask for random phase encode lines. Remaining panels in rows three to six show the images reconstructed using HDTV, BM3D, TV, PM diffusion and custom prior optimizations of PANO and DL. A region of interest indicated by the blue bounding box is enlarged and shown on the right side of each image. Second to fourth panels in the bottom row depict the difference images from the ground truth. Respective PSNR measures are shown in the insets.

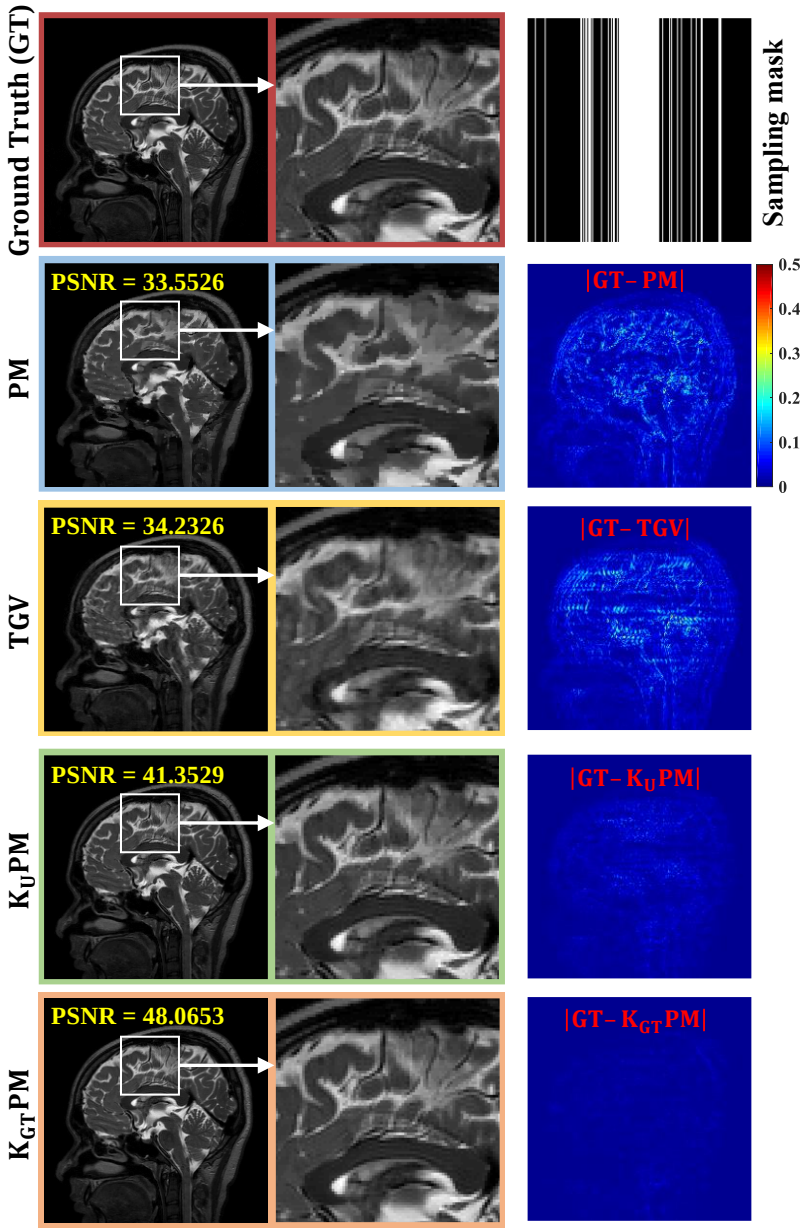

Figure 5.9. Comparison of directionality guided diffusion reconstruction with TGV and PM diffusion using sagittal slices of four different 12-channel T2 weighted MRI datasets. Row-wise panels show the ground truth and reconstructed images. Panels in the right most column show difference images and sampling pattern used to retrospectively undersample the ground truth. Respective PSNR measures are shown in the insets.

Table 5.1: Comparison of PSNR measures with different state-of-the-art reconstruction techniques averaged over pseudo-random, radial and random phase encoding lines sampling patterns.

Dataset (sampling%)	TV	K_UTV	K_PTV	K_DTV	K_BTV
Dataset I (20%)	32.9060	33.4085	35.5879	36.7753	36.1154
Dataset I (25%)	34.9772	35.6439	38.0352	39.1806	38.2912
Dataset I (33%)	38.0727	38.9116	41.1393	41.9091	40.7291
Dataset II (20%)	31.7682	32.1357	34.5566	35.5909	34.9438
Dataset II (25%)	33.8528	34.3010	36.7620	37.8260	36.9457
Dataset II (33%)	36.9961	37.7882	40.1275	40.9105	39.7312
Dataset III (20%)	29.3195	29.6922	31.3127	32.5324	31.7336
Dataset III (25%)	31.3081	31.7728	33.5428	34.6838	33.6253
Dataset III (33%)	34.2389	34.9124	36.5692	37.7037	36.1795

Table 5.1 (continued)

PM	K_UPM	K_PPM	K_DPM	K_BPM	$NLDR^M$
32.7388	35.1614	36.8442	37.5134	36.9265	34.4321
35.4548	37.6439	39.3202	39.7121	39.0731	36.6742
39.1725	40.9350	42.2972	42.4092	41.2610	40.5201
31.6694	34.0392	35.8682	36.2415	35.8375	33.8554
34.3358	36.4864	38.1837	38.3713	37.7949	35.7845
37.9706	39.8841	41.2503	41.4439	40.4040	38.9521
29.1328	31.1543	32.3957	32.9479	32.4735	30.8845
31.4248	33.4782	34.6381	35.0285	34.3394	33.5348
34.9406	36.5682	37.6173	38.0950	36.8103	35.9584

Table 5.1 (continued)

HDTV	PANO	DL	BM3D	$K_{GT}TV$	$K_{GT}PM$
33.2997	35.4558	35.1157	35.8605	*40.4238*	*45.2623*
35.7352	37.7127	38.1141	37.4551	*43.1008*	*46.7523*
39.4267	40.5263	41.2353	38.8156	*46.3274*	*48.7045*
32.2108	34.3985	34.1187	34.8339	*39.0451*	*44.1048*
34.5329	36.5862	36.6203	36.2841	*41.5952*	*45.5658*
38.4900	39.6454	40.1916	38.1187	*45.2072*	*47.6256*
30.0215	31.1711	31.0235	31.5349	*36.4091*	*40.5601*
33.1251	33.7535	32.9568	38.8648	*42.3205*	*32.4845*
35.8751	37.2466	34.6669	42.4587	*44.8297*	*36.0997*

76 out of 232 PE lines. Panels in the right most column depict difference images. The corresponding PSNR measures are shown in the insets. Results indicate an average gain of 7dB in PSNR for K_UPM compared to TGV. The enlarged regions of interest and difference images further confirm improved preservation of structural details obtained with the directionality guided reconstructions in regions like the boundaries of gray and white matter. The results using three additional datasets are shown in Fig. 5.10.

5.6.4 Effect of sampling rate and sampling patterns

In Fig. 5.11, steady-state RLNE is plotted versus sampling rate for TV, PM and guided diffusion reconstructions. These are averaged RLNE values from the reconstruction of three different datasets undersampled using Poisson-disc, radial and random PE lines sampling patterns. Plots indicate that the difference between the proposed methods and conventional TV/PM is higher for smaller sampling rates. The larger difference for PM indicates that for higher undersampling, proposed method benefits PM more than TV.

5.6.5 Influence of sampling patterns

To investigate the influence of different sampling patterns, in-vivo datasets are retrospectively undersampled using (i) Poisson-disc random sampling, (ii) Gaussian random sampling, (iii) Uniform PE lines, (iv) Random PE lines and (v) Radial sampling. A comparison of the reconstruction performance is shown in Fig. 5.12. Sampling rates of 33% and 25% are used. This correspond to 77 and 58 PE lines out of 232 for the uniform and random PE line sampling patterns and 90 and 66 radial lines

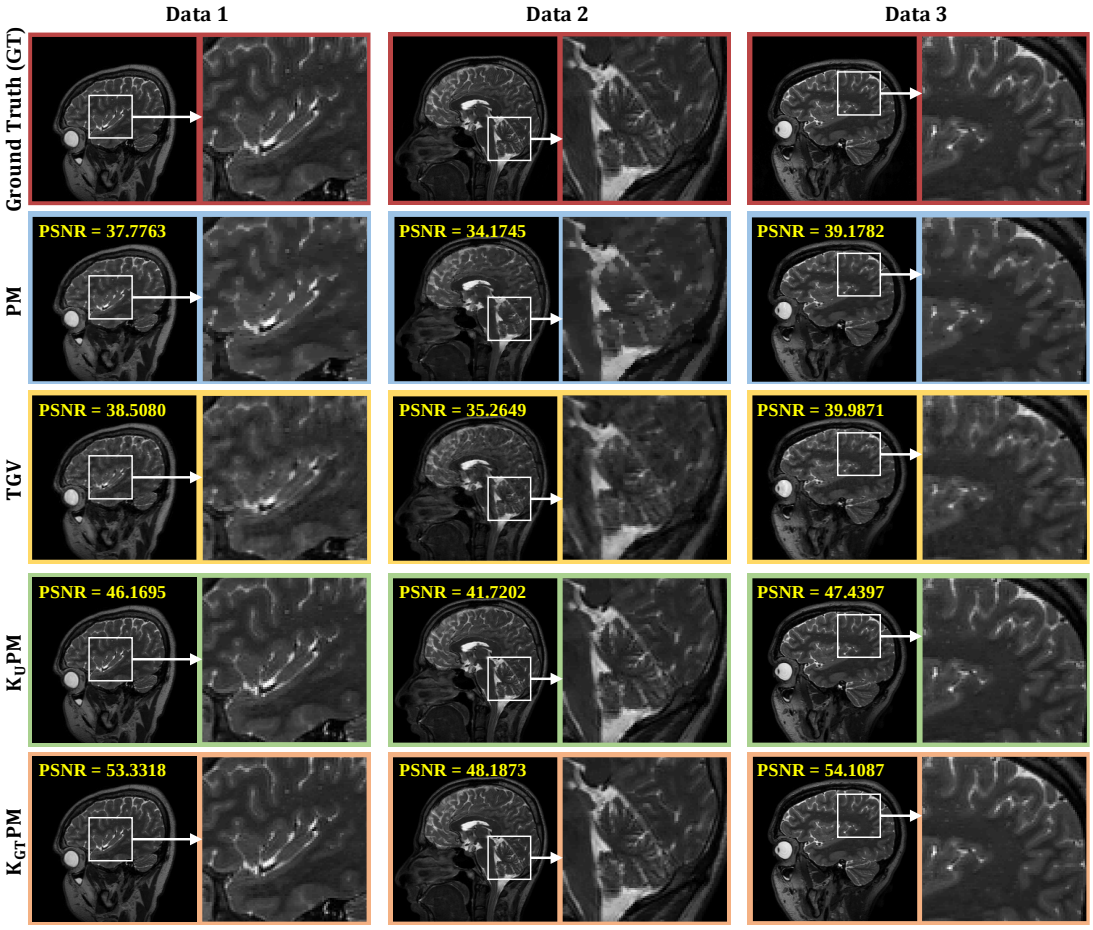

Figure 5.10. Comparison of directionality guided diffusion reconstruction with TGV and PM diffusion using sagittal slices of four different 12-channel T2 weighted MRI datasets. Row-wise panels show the ground truth and reconstructed images. Respective PSNR measures are shown in the insets.

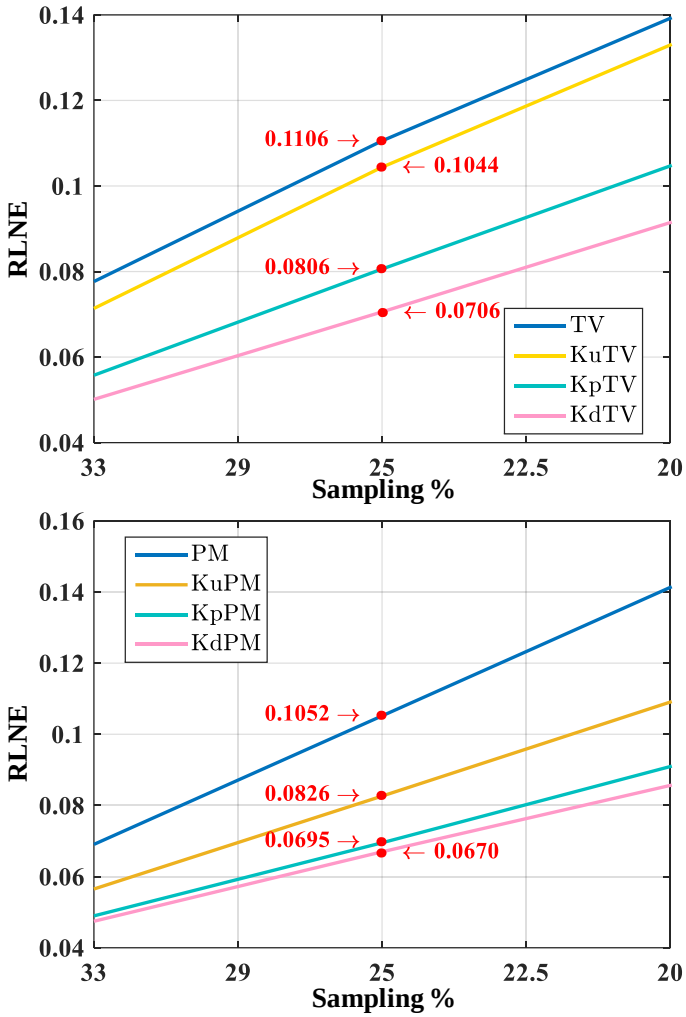

Figure 5.11. Plots of steady-state RLNE versus sampling rate. Top and bottom panels show the results of TV and PM diffusion, respectively, with and without custom prior optimized diffusion technique.

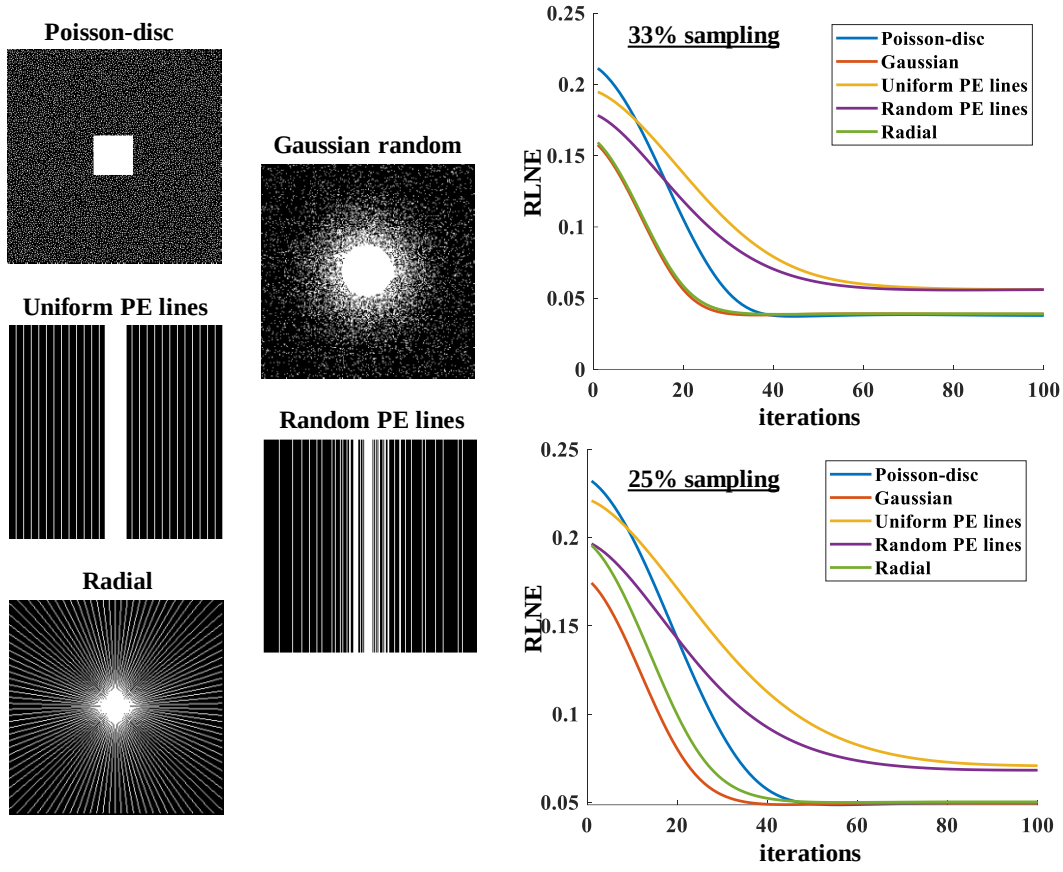

Figure 5.12. Performance comparison for different undersampling patterns. Panels on the left-hand side show the sampling patterns used. Panels on the right-hand side show plots of RLNE versus iteration number.

for the radial patterns, respectively. In the case of radial sampling, the actual non-Cartesian radial trajectory in 2D imaging is approximated with its closest Cartesian trajectory (189).

It is observed that best performance is obtained with radial, Gaussian and Poisson-disc sampling patterns as compared to the random and uniform PE lines. This is expected because incoherent sampling schemes such as Gaussian random and Poisson disc that subsamples the k-space along multiple dimensions causes the artifact to appear more noise-like, which is recommended by the CS theory. The comparison between different sampling rates shows that Random PE lines tend to perform better than the uniform PE lines at higher undersampling rates. For practical applications involving Cartesian sampling, skipping random phase encoding steps are preferred. Phase encoding steps are the main time-consuming factor in MRI acquisition. The impracticality of the random sampling of k-space points across all dimensions is mainly because the k-space trajectories have to be relatively smooth due to the hardware constraints (6). However, in the case of multidimensional acquisition that involve multiple phase encoding dimensions, random sampling can be applied to multiple phase encoding dimensions as shown in Fig. 4.8.

5.6.6 Convergence analysis

Fig. 5.13 shows the empirical convergence of K_{GT}PM for different choices of γ, α and n. Here, RLNE is plotted against reconstruction time for 200 iterations. It is observed that larger γ achieves faster convergence without compromising the steady-state

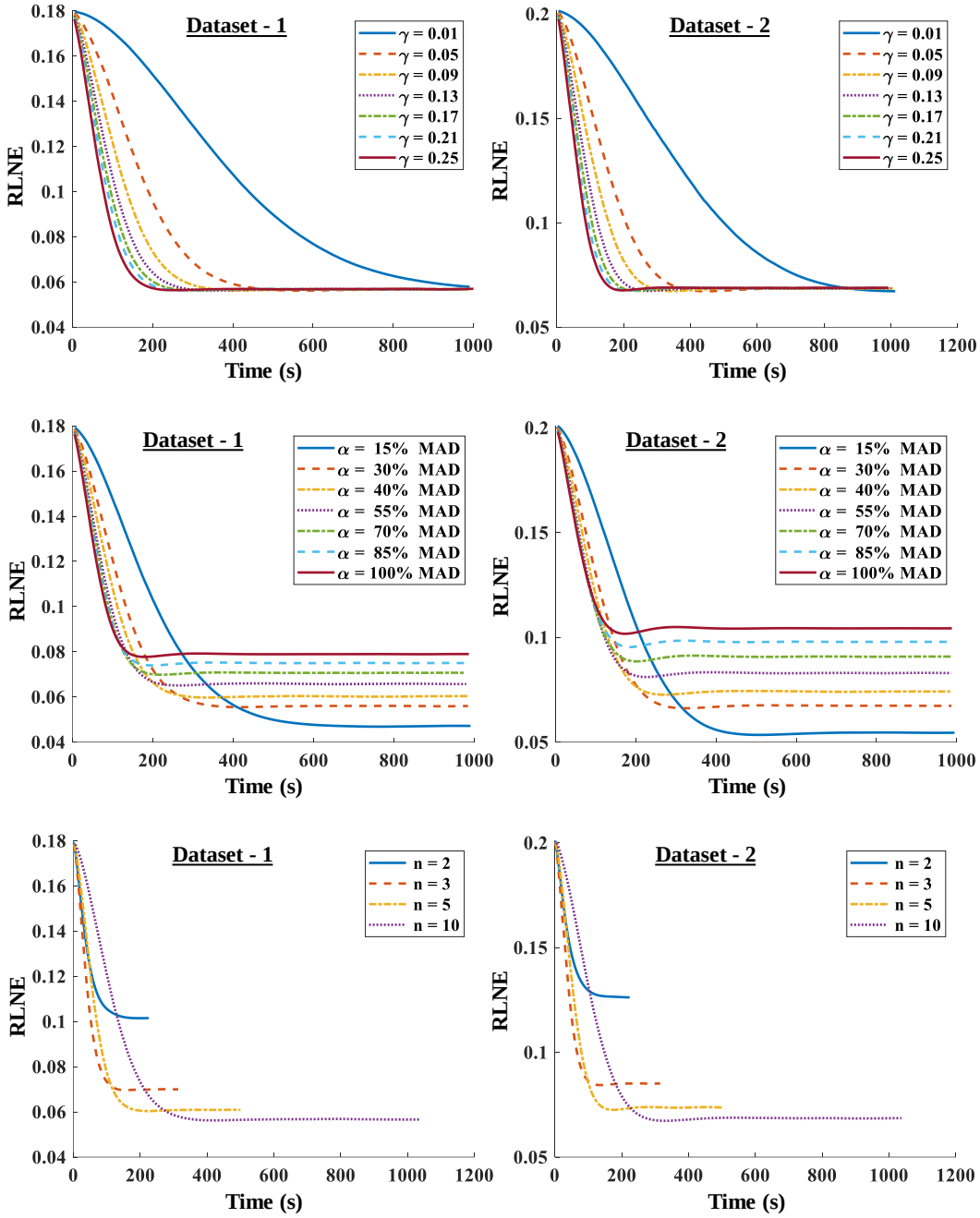

Figure 5.13. Empirical convergence of $K_{GT}PM$ for different choices of γ, α and n. RLNE is plotted against reconstruction time for 200 iterations.

errors. Faster convergence in this case can be attributed to the fact that larger γ encourages more diffusion per iteration.

With γ set as 0.1, larger values of α shows faster convergence at the cost of steady-state error. This does not come as a surprise since α is a threshold parameter which encourages the diffusion of edges whose gradient magnitudes fall below this threshold. The extent to which convergence speed can be compromised for better steady-state error generally depends on the gradient magnitudes of the inherent noise in the dataset (160).

In the case of n, it is observed that a significant improvement in steady-state error is achieved by increasing n from 2 to 10 at the cost of convergence rate. The reduced rate of convergence is due to the fact that the diffusion in each set of neighbors is computed one at a time. A parallel implementation (190) should significantly improve the convergence rate for the cases of $n > 1$ to make it closer to that of $n = 1$.

5.7 Discussion

The directionality guided NL diffusion approach proposed in this work describes how the information about diffusion direction can be used to improve the reconstruction performance.

5.7.1 Working principle

The proposed method works by approximating the underlying structure of an image from its gradients and non-linearly filter it based on the knowledge of locations of edges. This essentially varies the strength of denoising applied to true edges and

artifacts to preserve the structural details while diffusing artifacts. This is repeated for gradients computed in different angular directions and individual edges are mapped from these different filtered versions of the image. Since the variations in intensity function due to artifacts are minimized, it promotes sparsity in ∇U.

The directional gradients can be estimated using either a projection of the horizontal and vertical gradients onto the desired directions, or by finite difference operations performed on the interpolated intensities. While projection based approach can be used for implementing the diffusion equation using 4-neighbor explicit numerical scheme of Perona and Malik (191), interpolation enables implementation using the classical forward and backward finite difference operators at sub-pixel resolution as shown in (181). This is also a preferred choice since it is known that a proper description of the salient features (edges) in an image often requires sub-pixel accuracy of diffusion (192).

5.7.2 Reference reconstruction to choose diffusion direction

When the data from another reconstruction helps to choose the direction of diffusion, the resulting diffusion process can be considered to be in agreement with the orientation of edges recovered by that reconstruction. This results in an improved quality of reconstructed image as evident from the PSNR measures in Table 5.1.

5.7.3 Computational complexity

Computational complexity of the proposed filtering is mainly dependent on the number of gradient directions used in the model. It is observed that computing

gradients at every 10 to 20^0 angular intervals is sufficient to provide good quality reconstructions. Increment in image quality achieved using even more number of gradient directions is observed to be minimal. However, it is advisable to include all possible angular directions due to the unpredictability of structural details (orientation of edges) in the image at hand.

5.8 Conclusion

The rate of diffusion of edges oriented at different directions in an MR image varies with the direction in which they are diffused. Therefore, a directionality guided reconstruction technique is developed that uses a sophisticated mapping technique to choose the most reliable edges from a set of filtered versions of the image generated by diffusing it along different directions. This introduces a local variation in the direction of diffusion that promotes an accurate diffusion of artifacts while retaining true edges. In addition, customizability of the proposed reconstruction framework helps to incorporate the benefits of other known prior optimization techniques to guide the direction of diffusion.

Chapter 6

Summary and Conclusions

In this thesis, a biased NL diffusion technique using PM diffusivity function is presented as a more effective and efficient choice for edge-preserving sparse reconstruction of MR images, as opposed to other state-of-the-art techniques. Its significance is mainly due to the fact that the sharp and undistorted preservation of edges during an MR image reconstruction process often holds distinct advantages in terms of diagnostic quality. The key contributions of this thesis are summarized below.

1. NLDR reconstruction technique as a better alternative to TV for edge preserved reconstruction for pMRI.
    - NL diffusion reconstruction model selectively diffuses smooth regions of the image while preserving the structural details by restricting diffusion across true edges. The developed model gives more control over denoising (diffusion) by controlling the intensity modulations introduced by the undersampling of k-space using contrast parameter which is not possible in TV. This results in reduced blur/noise in the reconstructed images compared to those obtained using TV based method.

2. Sensitivity to regularization parameter is minimized using a statistically optimized contrast parameter.
    - NL diffusion involves a contrast parameter that separates the gradient magnitudes attributed to noise and true edges in an image so that diffusion can modify edge and uniform intensity regions differently. This parameter is estimated as the mean absolute deviation of the gradient magnitude so that it can adapt to the changes in the data. While regularization parameter plays a critical role in achieving the right amount of denoising using TV, adaptation of contrast parameter in NL diffusion significantly reduces the sensitivity to regularization parameter, thereby removing the need for search optimization and results in faster reconstruction.
3. A mixed order NLDR method that uses higher order diffusion to prevent the formation of step artifacts and speckle effects during reconstruction.
    - A fourth order regularization is introduced as a solution for blocky effect (step artifacts) in NLDR. Basic idea is to allow the reconstruction model to include a planar image as a possible solution using fourth order diffusion terms. While second order diffusion uses first order derivative of the image as a measure of smoothness, fourth order diffusion uses the second order derivative (Laplacian) as its smoothness measure which can better approximate smooth intensity variations.
    - In the absence of proposed regularization, if a step forms in the initial diffusion iterations, in a region of the image where intensity varies smoothly, the diffusion process tends to keep it in the final solution. In the presence of fourth

order terms in the reconstruction model, however, the smoothness is preserved because Laplacian will be minimum in such regions.

4. Developed a directional diffusion optimization technique for NLDR with edge emphasis correction.
    - The method developed is a sophisticated approach to map the individual edges from different filtered versions of the image so that for each individual edge, only the diffusion along its corresponding direction is considered. This helps to adapt the direction of diffusion to local variations in the directionality of edges and employ a precise diffusion in the local regions of the image on a sub-pixel level, leading to the preservation of the complex nature of edges.

6.1 Future Directions

Though the proposed methods, especially the directionality guided diffusion based reconstruction, demonstrate promising edge preservation properties at high undersampling rates, it is also limited by some of the factors like clinical feasibility of runtimes and the choice of gradient directions for diffusion. Therefore, further studies could be directed along different ways like automated selection of gradient directions based on the problem at hand and parallel implementation of the workflows to achieve clinically feasible runtime.

The increased computational complexity associated with the directionality guided diffusion is particularly due to large number of interpolations that restricts its practical application. Therefore, a main direction of future work should be towards reducing the computational complexity of this method without compromising on the image quality.

This can be achieved by reducing the number of interpolations required to compute the pixel values in extended neighborhoods.

6.1.1 Reducing the number of interpolations

One possibility is to choose the location of pixels in extended neighborhood in Fig. 5.2 such that it lies on the lines joining the pixels in a typical 4-pixel neighborhood, with the pixels in a typical 8-pixel neighborhood. This will transform the interpolations in 2D space to 1D interpolations by relaxing the distance constraint on neighboring pixels in extended neighborhood. While the distance of neighbors remains constant within a single neighborhood set, it is allowed to be different for different sets of extended neighborhoods. For the directional diffusion using 10 sets of neighborhoods, this approach should reduce the number of linear interpolations from 108 to 36 for each pixel.

6.1.2 Interpolation free approach

Another option is an interpolation-free approach that uses the known pixels in the grid at multiple orders away from a pixel p as its neighbors. This further relaxes the distance constraint on extended neighborhood pixel locations. By choosing the known pixel values in the grid along different directions as the extended neighbors, we can reduce the number of interpolations to zero. This will also keep the distance of neighboring pixel locations fixed within a single neighborhood, while allowing it to change between different sets of neighborhoods. While the former solution that reduces interpolation from 2D space to 1D space also allows diffusion along any arbitrary direction, the latter approach allows diffusion only along a fixed number of directions.

Bibliography

1. Candès EJ, Romberg J, Tao T. Robust uncertainty principles: Exact signal reconstruction from highly incomplete frequency information. IEEE Transactions on information theory. 2006;52(2):489-509.
2. Candes EJ, Tao T. Near-optimal signal recovery from random projections: Universal encoding strategies? IEEE transactions on information theory. 2006;52(12):5406-25.
3. Donoho DL. Compressed sensing. IEEE Transactions on information theory. 2006;52(4):1289-306.
4. Herman MA, Strohmer T. High-resolution radar via compressed sensing. IEEE transactions on signal processing. 2009;57(6):2275-84.
5. Herrmann FJ, Wang D, Hennenfent G, Moghaddam PP. Curvelet-based seismic data processing: A multiscale and nonlinear approach. Geophysics. 2007;73(1):A1-A5.
6. Lustig M, Donoho D, Pauly JM. Sparse MRI: The application of compressed sensing for rapid MR imaging. Magnetic Resonance in Medicine: An Official Journal of the International Society for Magnetic Resonance in Medicine. 2007;58(6):1182-95.

7. Block KT, Uecker M, Frahm J. Undersampled radial MRI with multiple coils. Iterative image reconstruction using a total variation constraint. Magnetic Resonance in Medicine: An Official Journal of the International Society for Magnetic Resonance in Medicine. 2007;57(6):1086-98.
8. Hahn EL. Spin echoes. Physical review. 1950;80(4):580.
9. Elster AD. Gradient-echo MR imaging: techniques and acronyms. Radiology. 1993;186(1):1-8.
10. Winkler ML, Ortendahl D, Mills T, et al. Characteristics of partial flip angle and gradient reversal MR imaging. Radiology. 1988;166(1):17-26.
11. Donoho DL, Elad M. Optimally sparse representation in general (nonorthogonal) dictionaries via ℓ1 minimization. Proceedings of the National Academy of Sciences. 2003;100(5):2197-202.
12. Gribonval R, Nielsen M. Sparse representations in unions of bases. IEEE transactions on Information theory. 2003;49(12):3320-5.
13. Candes EJ. The restricted isometry property and its implications for compressed sensing. Comptes rendus mathematique. 2008;346(9-10):589-92.
14. Candes EJ, Romberg JK, Tao T. Stable signal recovery from incomplete and inaccurate measurements. Communications on Pure and Applied Mathematics: A Journal Issued by the Courant Institute of Mathematical Sciences. 2006;59(8):1207-23.
15. Candes EJ, Tao T. Decoding by linear programming. IEEE transactions on information theory. 2005;51(12):4203-15.
16. Elad M, Milanfar P, Rubinstein R. Analysis versus synthesis in signal priors. Inverse problems. 2007;23(3):947.

17. Selesnick IW, Figueiredo MA. Signal restoration with overcomplete wavelet transforms: Comparison of analysis and synthesis priors. Wavelets XIII; 2009 Sep 4 (Vol. 7446, p. 74460D): International Society for Optics and Photonics.
18. Natarajan BK. Sparse approximate solutions to linear systems. SIAM journal on computing. 1995;24(2):227-34.
19. Candès EJ. Compressive sampling. Proceedings of the international congress of mathematicians; 2006 Aug 22 (Vol. 3, pp. 1433-1452): Madrid, Spain.
20. Chartrand R. Exact reconstruction of sparse signals via nonconvex minimization. IEEE Signal Processing Letters. 2007;14(10):707-10.
21. Daubechies I, DeVore R, Fornasier M, Güntürk CS. Iteratively reweighted least squares minimization for sparse recovery. Communications on Pure and Applied Mathematics: A Journal Issued by the Courant Institute of Mathematical Sciences. 2010;63(1):1-38.
22. Candes EJ, Romberg JK. Signal recovery from random projections. Computational Imaging III; 2005 Mar 11 (Vol. 5674, pp. 76-86): International Society for Optics and Photonics.
23. Daubechies I, Defrise M, De Mol C. An iterative thresholding algorithm for linear inverse problems with a sparsity constraint. Communications on Pure and Applied Mathematics: A Journal Issued by the Courant Institute of Mathematical Sciences. 2004;57(11):1413-57.
24. Elad M, Matalon B, Zibulevsky M. Image denoising with shrinkage and redundant representations. 2006 IEEE Computer Society Conference on Computer Vision and Pattern Recognition (CVPR'06); 2006 Jun 17 (Vol. 2, pp. 1924-1931): IEEE.

25. Beck A, Teboulle M. A fast iterative shrinkage-thresholding algorithm for linear inverse problems. SIAM journal on imaging sciences. 2009;2(1):183-202.
26. Zhang Y, Dong Z, Ji G, Wang S. An improved reconstruction method for CS-MRI based on exponential wavelet transform and iterative shrinkage/thresholding algorithm. Journal of Electromagnetic Waves and Applications. 2014;28(18):2327-38.
27. Zhang Y, Wang S, Ji G, Dong Z. Exponential wavelet iterative shrinkage thresholding algorithm with random shift for compressed sensing magnetic resonance imaging. IEEJ Transactions on Electrical and Electronic Engineering. 2015;10(1):116-7.
28. Combettes PL, Pesquet J-C. Proximal splitting methods in signal processing. Fixed-point algorithms for inverse problems in science and engineering: Springer; 2011. p. 185-212.
29. Combettes PL, Wajs VR. Signal recovery by proximal forward-backward splitting. Multiscale Modeling & Simulation. 2005;4(4):1168-200.
30. Mallat SG, Zhang Z. Matching pursuits with time-frequency dictionaries. IEEE Transactions on signal processing. 1993;41(12):3397-415.
31. Tropp JA, Gilbert AC. Signal recovery from random measurements via orthogonal matching pursuit. IEEE Transactions on information theory. 2007;53(12):4655-66.
32. Needell D, Vershynin R. Uniform uncertainty principle and signal recovery via regularized orthogonal matching pursuit. Foundations of computational mathematics. 2009;9(3):317-34.

33. Needell D, Tropp JA. CoSaMP: Iterative signal recovery from incomplete and inaccurate samples. Applied and computational harmonic analysis. 2009;26(3):301-21.

34. Chen SS, Donoho DL, Saunders MA. Atomic decomposition by basis pursuit. SIAM review. 2001;43(1):129-59.

35. Tibshirani R. Regression shrinkage and selection via the lasso. Journal of the Royal Statistical Society: Series B (Methodological). 1996;58(1):267-88.

36. Chen S, Donoho D. Basis pursuit. Proceedings of 1994 28th Asilomar Conference on Signals, Systems and Computers; 1994 Oct 31 (Vol. 1, pp. 41-44): IEEE.

37. Rudin LI, Osher S, Fatemi E. Nonlinear total variation based noise removal algorithms. Physica D: nonlinear phenomena. 1992;60(1-4):259-68.

38. Hu Y, Jacob M. Higher degree total variation (HDTV) regularization for image recovery. IEEE Transactions on Image Processing. 2012;21(5):2559-71.

39. Liang D, Wang H, Chang Y, Ying L. Sensitivity encoding reconstruction with nonlocal total variation regularization. Magnetic resonance in medicine. 2011;65(5):1384-92.

40. Knoll F, Bredies K, Pock T, Stollberger R. Second order total generalized variation (TGV) for MRI. Magnetic resonance in medicine. 2011;65(2):480-91.

41. Li X. The magic of nonlocal Perona–Malik diffusion. IEEE Signal Processing Letters. 2011;18(9):533-4.

42. Weickert J. Anisotropic Diffusion in Image Processing (Stuttgart: Teubner). 1998 Jan.

43. Liu T, Xiang Z. Image restoration combining the second-order and fourth-order PDEs. Mathematical Problems in Engineering. 2013;2013.

44. Rabi II, Zacharias JR, Millman S, Kusch P. A new method of measuring nuclear magnetic moment. Physical Review. 1938;53(4):318.

45. Lauterber P. Image formation by induced local interactions: examples employing nuclear magnetic resonance. Nature. 1974;246:469.

46. Cohen MS, Weisskoff RM. Ultra-fast imaging. Magnetic resonance imaging. 1991;9(1):1-37.

47. Margosian P, Schmitt F, Purdy D. Faster MR imaging: imaging with half the data. Health Care Instrum. 1986;1(6):195.

48. Cuppen J, van Est A. Reducing MR imaging time by one-sided reconstruction. Magnetic Resonance Imaging. 1987;5(6):526-7.

49. Xu Y, Haacke EM. Partial Fourier imaging in multi-dimensions: a means to save a full factor of two in time. Journal of Magnetic Resonance Imaging: An Official Journal of the International Society for Magnetic Resonance in Medicine. 2001;14(5):628-35.

50. Paul JS, Pillai UKS. A higher dimensional homodyne filter for phase sensitive partial Fourier reconstruction of magnetic resonance imaging. Magnetic resonance imaging. 2015;33(9):1114-25.

51. Luo J, Zhu Y, Li W, Croisille P, Magnin IE. MRI reconstruction from 2D truncated k-space. Journal of Magnetic Resonance Imaging. 2012;35(5):1196-206.

52. Schenck JF. The role of magnetic susceptibility in magnetic resonance imaging: MRI magnetic compatibility of the first and second kinds. Medical physics. 1996;23(6):815-50.

53. Port JD, Pomper MG. Quantification and minimization of magnetic susceptibility artifacts on GRE images. Journal of computer assisted tomography. 2000;24(6):958-64.

54. Smith TB, Nayak KS. MRI artifacts and correction strategies. Imaging in Medicine. 2010;2(4):445–57.

55. Wood ML, Mark Henkelman R. Truncation artifacts in magnetic resonance imaging. Magnetic resonance in medicine. 1985;2(6):517-26.

56. Schomberg H. Off-resonance correction of MR images. IEEE transactions on medical imaging. 1999;18(6):481-95.

57. Noll DC, Nishimura DG, Macovski A. Homodyne detection in magnetic resonance imaging. IEEE transactions on medical imaging. 1991;10(2):154-63.

58. Haacke E, Lindskogj E, Lin W. A fast, iterative, partial-Fourier technique capable of local phase recovery. Journal of Magnetic Resonance (1969). 1991;92(1):126-45.

59. Liang Z-P, Lauterbur PC. Principles of magnetic resonance imaging: a signal processing perspective: SPIE Optical Engineering Press; 2000.

60. Pauly J. Partial k-space reconstruction. http//users fmrib ox ac uk/~ karla/reading_group/lecture_notes/Recon_Pauly_read pdf. 2005.

61. Roemer PB, Edelstein WA, Hayes CE, Souza SP, Mueller OM. The NMR phased array. Magnetic resonance in medicine. 1990;16(2):192-225.

62. Hutchinson M, Raff U. Fast MRI data acquisition using multiple detectors. Magnetic resonance in Medicine. 1988;6(1):87-91.

63. Kwiat D, Einav S, Navon G. A decoupled coil detector array for fast image acquisition in magnetic resonance imaging. Medical physics. 1991;18(2):251-65.

64. Ra JB, Rim C. Fast imaging using subencoding data sets from multiple detectors. Magnetic resonance in medicine. 1993;30(1):142-5.

65. Jakob PM, Grisowld MA, Edelman RR, Sodickson DK. AUTO-SMASH: a self-calibrating technique for SMASH imaging. Magnetic Resonance Materials in Physics, Biology and Medicine. 1998;7(1):42-54.

66. Heidemann RM, Griswold MA, Haase A, Jakob PM. VD-AUTO-SMASH imaging. Magnetic Resonance in Medicine: An Official Journal of the International Society for Magnetic Resonance in Medicine. 2001;45(6):1066-74.

67. Bydder M, Larkman DJ, Hajnal JV. Generalized SMASH imaging. Magnetic Resonance in Medicine: An Official Journal of the International Society for Magnetic Resonance in Medicine. 2002;47(1):160-70.

68. Griswold MA, Jakob PM, Nittka M, Goldfarb JW, Haase A. Partially parallel imaging with localized sensitivities (PILS). Magnetic Resonance in Medicine. 2000;44(4):602-9.

69. Kyriakos WE, Panych LP, Kacher DF, et al. Sensitivity profiles from an array of coils for encoding and reconstruction in parallel (SPACE RIP). Magnetic Resonance in Medicine: An Official Journal of the International Society for Magnetic Resonance in Medicine. 2000;44(2):301-8.

70. Sodickson DK. Simultaneous acquisition of spatial harmonics (SMASH): ultra-fast imaging with radiofrequency coil arrays. Magnetic resonance in medicine. 1997 Oct;38(4):591-603.

71. Pruessmann KP, Weiger M, Scheidegger MB, Boesiger P. SENSE: sensitivity encoding for fast MRI. Magnetic resonance in medicine. 1999;42(5):952-62.

72. Griswold MA, Jakob PM, Heidemann RM, et al. Generalized autocalibrating partially parallel acquisitions (GRAPPA). Magnetic Resonance in Medicine: An Official Journal of the International Society for Magnetic Resonance in Medicine. 2002;47(6):1202-10.

73. Lustig M, Santos JM, Donoho DL, Pauly JM. kt SPARSE: High frame rate dynamic MRI exploiting spatio-temporal sparsity. Proceedings of the 13th annual meeting of ISMRM, Seattle; 2006 May 6 (Vol. 2420).

74. Jung H, Ye JC, Kim EY. Improved k–t BLAST and k–t SENSE using FOCUSS. Physics in Medicine & Biology. 2007;52(11):3201.

75. Gorodnitsky IF, Rao BD. Sparse signal reconstruction from limited data using FOCUSS: A re-weighted minimum norm algorithm. IEEE Transactions on signal processing. 1997;45(3):600-16.

76. King K. Combining compressed sensing and parallel imaging. Proceedings of the 16th annual meeting of ISMRM, Toronto; 2008 (Vol. 1488, p. 44).

77. Liu B, Sebert F, Zou Y, Ying L. SparseSENSE: randomly-sampled parallel imaging using compressed sensing. In: Proceedings of the 16th Annual Meeting of ISMRM; 2008 May 3.

78. Zhao C, Lang T, Ji J. Compressed sensing parallel imaging. proceedings of the 16th annual meeting of ISMRM, Toronto; 2008 May (Vol. 1478).

79. Marinelli L, Hardy C, Blezek D. MRI with accelerated multi-coil compressed sensing. Proc ISMRM 16th Scientific Sessions. 2008:1484.

80. Liang D, Liu B, Wang J, Ying L. Accelerating SENSE using compressed sensing. Magnetic Resonance in Medicine: An Official Journal of the International Society for Magnetic Resonance in Medicine. 2009;62(6):1574-84.

81. Lustig M, Alley M, Vasanawala S, Donoho D, Pauly J. L1 SPIR-iT: Autocalibrating parallel imaging compressed sensing. Proc Intl Soc Mag Reson Med; 2009 Apr (Vol. 17, p. 379).

82. Doneva M, Börnert P, Eggers H, Mertins A. Partial Fourier compressed sensing. Proc Intl Soc Mag Reson Med; 2010 (Vol. 18, p. 4851).

83. Huang F, Chen Y, Yin W, et al. A rapid and robust numerical algorithm for sensitivity encoding with sparsity constraints: Self-feeding sparse SENSE. Magnetic Resonance in Medicine. 2010;64(4):1078-88.

84. Liu F, Duan Y, Peterson B, Kangarlu A. Compressed sensing MRI combined with SENSE in partial k-space. Physics in Medicine & Biology. 2012;57(21):N391.

85. Lustig M, Pauly JM. SPIRiT: iterative self-consistent parallel imaging reconstruction from arbitrary k-space. Magnetic resonance in medicine. 2010;64(2):457-71.

86. Murphy M, Alley M, Demmel J, Keutzer K, Vasanawala S, Lustig M. Fast l1-SPIRiT Compressed Sensing Parallel Imaging MRI: Scalable Parallel Implementation and Clinically Feasible Runtime. IEEE transactions on medical imaging. 2012;31(6):1250-62.

87. Uecker M, Lai P, Murphy MJ, et al. ESPIRiT—an eigenvalue approach to autocalibrating parallel MRI: where SENSE meets GRAPPA. Magnetic resonance in medicine. 2014;71(3):990-1001.

88. Caballero J, Price AN, Rueckert D, Hajnal JV. Dictionary learning and time sparsity for dynamic MR data reconstruction. IEEE transactions on medical imaging. 2014;33(4):979-94.

89. Guo W, Qin J, Yin W. A new detail-preserving regularization scheme. SIAM journal on imaging sciences. 2014;7(2):1309-34.

90. Pejoski S, Kafedziski V, Gleich D. Compressed sensing MRI using discrete nonseparable shearlet transform and FISTA. IEEE Signal Processing Letters. 2015;22(10):1566-70.

91. Qu X, Zhang W, Guo D, Cai C, Cai S, Chen Z. Iterative thresholding compressed sensing MRI based on contourlet transform. Inverse Problems in Science and Engineering. 2010;18(6):737-58.

92. Qu X, Cao X, Guo D, Hu C, Chen Z. Combined sparsifying transforms for compressed sensing MRI. Electronics letters. 2010;46(2):121-3.

93. Hu Y, Ongie G, Ramani S, Jacob M. Generalized higher degree total variation (HDTV) regularization. IEEE Transactions on Image Processing. 2014;23(6):2423-35.

94. Bredies K, Kunisch K, Pock T. Total generalized variation. SIAM Journal on Imaging Sciences. 2010;3(3):492-526.

95. Hong M, Yu Y, Wang H, Liu F, Crozier S. Compressed sensing MRI with singular value decomposition-based sparsity basis. Physics in Medicine & Biology. 2011;56(19):6311.

96. Ravishankar S, Bresler Y. MR image reconstruction from highly undersampled k-space data by dictionary learning. IEEE transactions on medical imaging. 2010;30(5):1028-41.

97. Qu X, Guo D, Ning B, et al. Undersampled MRI reconstruction with patch-based directional wavelets. Magnetic resonance imaging. 2012;30(7):964-77.

98. Deka B, Datta S, Handique S. Wavelet tree support detection for compressed sensing MRI reconstruction. IEEE Signal Processing Letters. 2018;25(5):730-4.

99. Olshausen BA, Field DJ. Emergence of simple-cell receptive field properties by learning a sparse code for natural images. Nature. 1996;381(6583):607.

100. Aharon M, Elad M, Bruckstein A. K-SVD: An algorithm for designing overcomplete dictionaries for sparse representation. IEEE Transactions on signal processing. 2006;54(11):4311-22.

101. Rubinstein R, Bruckstein AM, Elad M. Dictionaries for sparse representation modeling. Proceedings of the IEEE. 2010;98(6):1045-57.

102. Tosic I, Jovanovic I, Frossard P, Vetterli M, Duric N. Ultrasound tomography with learned dictionaries. Proceedings of the IEEE International Conference on Acoustics, Speech, and Signal Processing; 2010 Mar 14 (pp. 5502-5505).

103. Elad M, Aharon M. Image denoising via sparse and redundant representations over learned dictionaries. IEEE Transactions on Image processing. 2006;15(12):3736-45.

104. Mairal J, Elad M, Sapiro G. Sparse representation for color image restoration. IEEE Transactions on image processing. 2007;17(1):53-69.

105. Doneva M, Börnert P, Eggers H, Stehning C, Sénégas J, Mertins A. Compressed sensing reconstruction for magnetic resonance parameter mapping. Magnetic Resonance in Medicine. 2010;64(4):1114-20.

106. Bilgin A, Kim Y, Liu F, Nadar M. Dictionary design for compressed sensing MRI. Proceedings of the 18th Scientific Meeting of ISMRM, Stockholm; 2010.

107. Chen Y, Ye X, Huang F. A novel method and fast algorithm for MR image reconstruction with significantly under-sampled data. Inverse Problems and Imaging. 2010;4(2):223-40.

108. Otazo R, Sodickson D. Adaptive compressed sensing MRI. Proceedings of the 18th Scientific Meeting of ISMRM, Stockholm; 2010 May (p. 4867).

109. Lingala SG, Jacob M. Blind compressive sensing dynamic MRI. IEEE transactions on medical imaging. 2013;32(6):1132-45.

110. Awate SP, DiBella EV. Spatiotemporal dictionary learning for undersampled dynamic MRI reconstruction via joint frame-based and dictionary-based sparsity. 2012 9th IEEE International Symposium on Biomedical Imaging (ISBI); 2012 May 2 (pp. 318-321): IEEE.

111. Wang Y, Ying L. Compressed sensing dynamic cardiac cine MRI using learned spatiotemporal dictionary. IEEE transactions on Biomedical Engineering. 2013;61(4):1109-20.

112. Ophir B, Lustig M, Elad M. Multi-scale dictionary learning using wavelets. IEEE Journal of Selected Topics in Signal Processing. 2011;5(5):1014-24.

113. Liu Q, Wang S, Ying L, Peng X, Zhu Y, Liang D. Adaptive dictionary learning in sparse gradient domain for image recovery. IEEE Transactions on Image Processing. 2013;22(12):4652-63.

114. Ning B, Qu X, Guo D, Hu C, Chen Z. Magnetic resonance image reconstruction using trained geometric directions in 2D redundant wavelets domain and non-convex optimization. Magnetic resonance imaging. 2013;31(9):1611-22.

115. Qu X, Hou Y, Lam F, Guo D, Zhong J, Chen Z. Magnetic resonance image reconstruction from undersampled measurements using a patch-based nonlocal operator. Medical image analysis. 2014;18(6):843-56.

116. Dabov K, Foi A, Katkovnik V, Egiazarian K. Image denoising by sparse 3-D transform-domain collaborative filtering. Image Processing, IEEE Transactions on 16 (8), pp. 2080-2095. 2007.

117. Eksioglu EM. Decoupled algorithm for MRI reconstruction using nonlocal block matching model: BM3D-MRI. Journal of Mathematical Imaging and Vision. 2016;56(3):430-40.

118. Lai Z, Qu X, Liu Y, et al. Image reconstruction of compressed sensing MRI using graph-based redundant wavelet transform. Medical image analysis. 2016;27:93-104.

119. Ram I, Elad M, Cohen I. Redundant wavelets on graphs and high dimensional data clouds. IEEE Signal Processing Letters. 2012;19(5):291-4.

120. Ram I, Elad M, Cohen I. Image processing using smooth ordering of its patches. IEEE transactions on image processing. 2013;22(7):2764-74.

121. Lai Z, Zhang X, Guo D, et al. Joint sparse reconstruction of multi-contrast MRI images with graph based redundant wavelet transform. BMC medical imaging. 2018;18(1):7.

122. Candès EJ, Recht B. Exact matrix completion via convex optimization. Foundations of Computational mathematics. 2009;9(6):717.

123. Lingala SG, Hu Y, DiBella E, Jacob M. Accelerated dynamic MRI exploiting sparsity and low-rank structure: kt SLR. IEEE transactions on medical imaging. 2011;30(5):1042-54.

124. Akçakaya M, Basha TA, Goddu B, et al. Low-dimensional-structure self-learning and thresholding: regularization beyond compressed sensing for MRI reconstruction. Magnetic Resonance in Medicine. 2011;66(3):756-67.

125. Yoon H, Kim KS, Kim D, Bresler Y, Ye JC. Motion adaptive patch-based low-rank approach for compressed sensing cardiac cine MRI. IEEE transactions on medical imaging. 2014;33(11):2069-85.

126. Jin KH, Lee D, Ye JC. A general framework for compressed sensing and parallel MRI using annihilating filter based low-rank Hankel matrix. IEEE Transactions on Computational Imaging. 2016;2(4):480-95.

127. Majumdar A, Ward RK. An algorithm for sparse MRI reconstruction by Schatten p-norm minimization. Magnetic resonance imaging. 2011;29(3):408-17.

128. Yao J, Xu Z, Huang X, Huang J. An efficient algorithm for dynamic MRI using low-rank and total variation regularizations. Medical image analysis. 2018;44:14-27.

129. Shin PJ, Larson PE, Ohliger MA, et al. Calibrationless parallel imaging reconstruction based on structured low-rank matrix completion. Magnetic resonance in medicine. 2014;72(4):959-70.

130. Ongie G, Jacob M. A fast algorithm for convolutional structured low-rank matrix recovery. IEEE transactions on computational imaging. 2017;3(4):535-50.

131. Haldar JP, Zhuo J. P-LORAKS: Low-rank modeling of local k-space neighborhoods with parallel imaging data. Magnetic resonance in medicine. 2016;75(4):1499-514.

132. Lee D, Jin KH, Kim EY, Park SH, Ye JC. Acceleration of MR parameter mapping using annihilating filter-based low rank hankel matrix (ALOHA). Magnetic resonance in medicine. 2016;76(6):1848-64.

133. Haldar JP. Low-rank modeling of local k-space neighborhoods: from phase and support constraints to structured sparsity. Wavelets and Sparsity XVI; 2015 Aug 24 (Vol. 9597, p. 959710): International Society for Optics and Photonics.

134. Haldar JP. Low-rank modeling of local k-space neighborhoods (LORAKS) for constrained MRI. IEEE transactions on medical imaging. 2013;33(3):668-81.

135. Sun J, Li H, Xu Z. Deep ADMM-Net for compressive sensing MRI. Advances in neural information processing systems; 2016 (pp. 10-18).

136. Wang S, Su Z, Ying L, et al. Accelerating magnetic resonance imaging via deep learning. 2016 IEEE 13th International Symposium on Biomedical Imaging (ISBI); 2016 Apr 13 (pp. 514-517): IEEE.

137. Mardani M, Gong E, Cheng JY, et al. Deep generative adversarial neural networks for compressive sensing MRI. IEEE transactions on medical imaging. 2018;38(1):167-79.

138. Hammernik K, Klatzer T, Kobler E, et al. Learning a variational network for reconstruction of accelerated MRI data. Magnetic resonance in medicine. 2018;79(6):3055-71.

139. Aggarwal HK, Mani MP, Jacob M. MoDL: Model Based Deep Learning Architecture for Inverse Problems. IEEE transactions on medical imaging. 2018;38(2):394-405.
140. Schlemper J, Caballero J, Hajnal JV, Price AN, Rueckert D. A deep cascade of convolutional neural networks for dynamic MR image reconstruction. IEEE transactions on Medical Imaging. 2017;37(2):491-503.
141. Tsiotsios C, Petrou M. On the choice of the parameters for anisotropic diffusion in image processing. Pattern recognition. 2013;46(5):1369-81.
142. Gerig G, Kubler O, Kikinis R, Jolesz FA. Nonlinear anisotropic filtering of MRI data. IEEE Transactions on medical imaging. 1992;11(2):221-32.
143. Krissian K, Aja-Fernández S. Noise-driven anisotropic diffusion filtering of MRI. IEEE transactions on image processing. 2009;18(10):2265-74.
144. Lohmann G, Bohn S, Müller K, Trampel R, Turner R. Image restoration and spatial resolution in 7-tesla magnetic resonance imaging. Magnetic resonance in medicine. 2010;64(1):15-22.
145. Block KT, Uecker M, Frahm J. Suppression of MRI truncation artifacts using total variation constrained data extrapolation. International journal of biomedical imaging. 2008;2008.
146. Guichard F, Morel J-M. A note on two classical enhancement filters and their associated pde's. International Journal of Computer Vision. 2003;52(2-3):153-60.
147. Krishnan AP, Joy A, Paul JS. Improved image reconstruction of low-resolution multichannel phase contrast angiography. Journal of Medical Imaging. 2016;3(1):014001.

148. Perona P, Malik J. Scale-space and edge detection using anisotropic diffusion. IEEE Transactions on pattern analysis and machine intelligence. 1990;12(7):629-39.

149. Nordström KN. Biased anisotropic diffusion: a unified regularization and diffusion approach to edge detection. Image and vision computing. 1990;8(4):318-27.

150. You Y-L, Xu W, Tannenbaum A, Kaveh M. Behavioral analysis of anisotropic diffusion in image processing. IEEE Transactions on Image Processing. 1996;5(11):1539-53.

151. Steidl G, Weickert J, Brox T, Mrázek P, Welk M. On the equivalence of soft wavelet shrinkage, total variation diffusion, total variation regularization, and SIDEs. SIAM Journal on Numerical Analysis. 2004;42(2):686-713.

152. Pham-Gia T, Hung T. The mean and median absolute deviations. Mathematical and Computer Modelling. 2001;34(7-8):921-36.

153. Black MJ, Sapiro G, Marimont DH, Heeger D. Robust anisotropic diffusion. IEEE Transactions on image processing. 1998;7(3):421-32.

154. Wen Y-W, Chan RH. Parameter selection for total-variation-based image restoration using discrepancy principle. IEEE Transactions on Image Processing. 2011;21(4):1770-81.

155. Haldar JP. Real MRI Dataset Samples. Available at: https://mr.usc.edu/download/data/. Accessed September 10, 2018.

156. Charbonnier P, Blanc-Feraud L, Aubert G, Barlaud M. Two deterministic half-quadratic regularization algorithms for computed imaging. Proceedings of 1st

International Conference on Image Processing; 1994 Nov 13 (Vol. 2, pp. 168-172): IEEE.

157. Andreu F, Ballester C, Caselles V, Mazón JM. Minimizing total variation flow. Differential and integral equations. 2001;14(3):321-60.
158. Zhan Z, Cai J-F, Guo D, Liu Y, Chen Z, Qu X. Fast multiclass dictionaries learning with geometrical directions in MRI reconstruction. IEEE Transactions on biomedical engineering. 2015;63(9):1850-61.
159. Brox T, Welk M, Steidl G, Weickert J. Equivalence results for TV diffusion and TV regularisation. International Conference on Scale-Space Theories in Computer Vision; 2003 Jun 10 (pp. 86-100): Springer.
160. Joy A, Paul JS. Multichannel compressed sensing MR image reconstruction using statistically optimized nonlinear diffusion. Magnetic resonance in medicine. 2017;78(2):754-62.
161. You Y-L, Kaveh M. Fourth-order partial differential equations for noise removal. IEEE Transactions on Image Processing. 2000;9(10):1723-30.
162. Didas S, Weickert J, Burgeth B. Properties of higher order nonlinear diffusion filtering. Journal of mathematical imaging and vision. 2009;35(3):208-26.
163. Lysaker M, Lundervold A, Tai X-C. Noise removal using fourth-order partial differential equation with applications to medical magnetic resonance images in space and time. IEEE Transactions on image processing. 2003;12(12):1579-90.
164. Lysaker M, Tai X-C. Iterative image restoration combining total variation minimization and a second-order functional. International journal of computer vision. 2006;66(1):5-18.

165. Chambolle A, Lions P-L. Image recovery via total variation minimization and related problems. Numerische Mathematik. 1997;76(2):167-88.

166. Bresler Y. DLMRI-Lab. Available at: http://www.ifp.illinois.edu/~yoram/Software.html. Accessed October 18, 2018.

167. Caballero J. DLTG. Available at: http://www.doc.ic.ac.uk/~jc1006/software.html. Accessed October 18, 2018.

168. Knoll F. Second order TGV reconstruction for undersampled radial MR. Available at: http://cai2r.net/resources/software/second-order-tgv-reconstruction-undersampled-radial-mr. Accessed December 5, 2018.

169. Jacob M. Higher degree total variation (HDTV). Available at: http://user.engineering.uiowa.edu/~jcb/Software/HDTV/Software.html. Accessed October 18, 2018.

170. Hansen PC. Rank-deficient and discrete ill-posed problems: numerical aspects of linear inversion: Siam; 2005.

171. Gudbjartsson H, Patz S. The Rician distribution of noisy MRI data. Magnetic resonance in medicine. 1995;34(6):910-4.

172. Lustig M, Vasanawala S. Undersampled abdomens. Available at: http://mridata.org/undersampled/abdomens. Accessed January 24, 2018.

173. Lefkimmiatis S, Ward JP, Unser M. Hessian Schatten-norm regularization for linear inverse problems. IEEE transactions on image processing. 2013;22(5):1873-88.

174. Joy A, Paul JS. A mixed-order nonlinear diffusion compressed sensing MR image reconstruction. Magnetic resonance in medicine. 2018;80(5):2215-22.

175. Saucedo A, Joy A, Daar E, et al. Comparison of compressed sensing reconstruction for 3D echo planar spectroscopic imaging data using total variation and statistically optimized Perona-Malik non-linear diffusion. Proceedings of the Joint Annual Meeting ISMRM-ESMRMB; 2018.
176. Ravishankar S, Bresler Y. Data-Driven Learning of a Union of Sparsifying Transforms Model for Blind Compressed Sensing. IEEE Trans Computational Imaging. 2016;2(3):294-309.
177. Wang S, Tan S, Gao Y, et al. Learning Joint-Sparse Codes for Calibration-Free Parallel MR Imaging. IEEE transactions on medical imaging. 2018;37(1):251-61.
178. Adluru G, McGann C, Speier P, Kholmovski EG, Shaaban A, DiBella EV. Acquisition and reconstruction of undersampled radial data for myocardial perfusion magnetic resonance imaging. Journal of Magnetic Resonance Imaging: An Official Journal of the International Society for Magnetic Resonance in Medicine. 2009;29(2):466-73.
179. Chen L, Schabel MC, DiBella EV. Reconstruction of dynamic contrast enhanced magnetic resonance imaging of the breast with temporal constraints. Magnetic resonance imaging. 2010;28(5):637-45.
180. Meijering E. A chronology of interpolation: from ancient astronomy to modern signal and image processing. Proceedings of the IEEE. 2002;90(3):319-42.
181. Terebes R, Borda M, Baozong Y, Lavialle O, Baylou P. A new PDE based approach for image restoration and enhancement using robust diffusion directions and directional derivatives based diffusivities. Proceedings 7th

International Conference on Signal Processing, 2004 Proceedings ICSP'04 2004; 2004 (Vol. 1, pp. 707-712): IEEE.

182. Thévenaz P, Blu T, Unser M. Interpolation revisited [medical images application]. IEEE Transactions on medical imaging. 2000;19(7):739-58.
183. Unser M. Splines: A perfect fit for signal and image processing. IEEE Signal processing magazine. 1999;16(6):22-38.
184. Unser M, Fageot J, Ward JP. Splines Are Universal Solutions of Linear Inverse Problems with Generalized TV Regularization. SIAM Review. 2017;59(4):769-93.
185. Danielyan A, Katkovnik V, Egiazarian K. BM3D frames and variational image deblurring. IEEE Transactions on Image Processing. 2012;21(4):1715-28.
186. Montgomery DC, Runger GC. Applied statistics and probability for engineers: John Wiley & Sons; 2010.
187. Eksioglu E. MATLAB code to realize the BM3D-MRI algorithm. Available at: http://web.itu.edu.tr/eksioglue/pubs/BM3D_MRI.htm. Accessed October 18, 2018.
188. Qu X. PANO Code. Available at: https://sites.google.com/site/xiaoboxmu/publication. Accessed May 20, 2018.
189. Liu Y, Zhan Z, Cai J-F, Guo D, Chen Z, Qu X. Projected iterative soft-thresholding algorithm for tight frames in compressed sensing magnetic resonance imaging. IEEE transactions on medical imaging. 2016;35(9):2130-40.
190. Chang CH, Ji J. Compressed sensing MRI with multichannel data using multicore processors. Magnetic resonance in medicine. 2010;64(4):1135-9.

191. Terebes R, Lavialle O, Baylou P, Borda M. Directional anisotropic diffusion. 2002 11th European Signal Processing Conference; 2002 Sep 3 (pp. 1-4): IEEE.

192. Ludusan C, Lavialle O. Multifocus image fusion and denoising: a variational approach. Pattern Recognition Letters. 2012;33(10):1388-96.